SEIMICALLY INDUCED SETTLEMENT OF PARTIALLY-SATURATED SAND

by

MAJID GHAYOOMI

B.Sc., University of Tehran, Iran, 2004

M.Sc., Sharif University of Technology, 2006

A thesis submitted to the

Faculty of the Graduate School of the

University of Colorado in partial fulfillment

of the requirement for the degree of

Doctor of Philosophy

Department of Civil, Environmental and Architectural Engineering

2011

This thesis entitled:
Seismically Induced Settlement of Partially-Saturated Sand
written by Majid Ghayoomi
has been approved for the Department of Civil, Environmental and Architectural Engineering

_____
(John S. McCartney)

_____
(Hon-Yim Ko)

Date_____

The final copy of this thesis has been examined by the signatories, and we
Find that both the content and the form meet acceptable presentation standards
Of scholarly work in the above mentioned discipline.

Ghayoomi, Majid (Ph.D., Civil, Environmental and Architectural Engineering)

Seismically Induced Settlement of Partially-Saturated Sand

Thesis directed by Assistant Professor John McCartney and Professor Hon-Yim Ko

Deformation of soil layers during earthquake shaking is a major cause of damage to buildings and geotechnical structures. Over the past 40 years, several design methods have been proposed to quantify and estimate the settlement of sand layers due to seismic loads. Most of these methods have been focused on sands in dry or water-saturated conditions, leaving a gap in the basic understanding of the mechanisms of seismically induced settlements of partially-saturated sands. Design approaches for partially-saturated soil layers deserve further development because these soil layers may have different deformation mechanisms during earthquake loading than water-saturated or dry soil layers. In this research an effective stress-based empirical methodology is proposed to predict the earthquake induced settlement of a free field partially-saturated sand layer. This approach uses a complex coupling between stress state, seismic compression, and pore water pressure generation during earthquake loading. Accordingly, an experimental study on partially saturated soils was used in tandem with this design model to quantify input relationships for the different variables during earthquake loading and also to verify the induced settlement estimated using the proposed empirical approach. A new centrifuge physical modeling technique was developed that involves a soil specimen within a laminar container mounted atop a hydraulic servo-controlled shake table in a geotechnical centrifuge. Steady state infiltration of water was used to control the stress state in the partially-saturated sand layer during centrifugation. Specifically, infiltration was found to lead to a relatively uniform degree of saturation with depth in the sand layer, simplifying interpretation of the deformation response. Sand layers with a wide range of degrees of saturation were evaluated using this approach to assess the degree of saturation on their deformation response during cyclic loading. A nonlinear trend was observed in the variation of the surface settlement with degree of saturation, with a minimum value obtained for sand with a degree of saturation of about 0.4. This trend is consistent with the relationship between small-strain shear modulus and degree of saturation measured using bender elements and resonant column testing techniques and also with the predicted trend using the developed empirical methodology.

Dedication

This thesis is dedicated to my parents, Ali-Akbar and Nahid, my wife, Arezou, and my sister, Zahra, for their endless love, encouragement, and support.

Acknowledgements

I would like to thank my advisors, Professor John S. McCartney and Professor Hon-Yim Ko for their wisdom, inspiration, patience, friendship and dedication. Particularly, I cherish the many philosophical and analytical discussions Professor McCartney shared on topics ranging from science and engineering to effective presentation and writing style. He has certainly gone above and beyond the call of duty of an advisor.

I would especially like to thank Ali Khosravi for his friendship, thoughtful discussion and many important contributions to this research.

Thanks to Ibrahim Abaidala, Samiha Abdelrahman, and Thamer Al-Yaqub for their assistance in the centrifuge experiments, and to Mike Eck and Kent Polkinghorne for their assistance in performing the centrifuge tests and programming the network analyzer in Labview.

Without the unconditional love and support of my wife and the encouragement of my family, this work would not have been possible.

I am grateful to Professors Stein Sture, Dobroslav Znidarcic, Nien-Yin Chang, and Antonio Carraro for serving on my thesis committee.

CONTENTS

TABLES

Table

FIGURES

Figure

CHAPTER I

INTRODUCTION

1.1 Research Motivation

Deformation of soil layers during earthquake loading is a major cause of damage to buildings and geotechnical structures. Differential movement may cause distress in earth structures or buildings founded in the soil. Historically, investigations into the settlement of soil layers during earthquake shaking or application of dynamic loads have focused on dry or water-saturated conditions (Seed and silver 1972; Lee and Albaisa 1974; Finn and Byrne 1976; Tokimatsu and Seed 1987; Pradel 1998). This has left a gap in the understanding of the fundamental mechanisms of seismically induced settlement of partially-saturated soils. Although some have argued that the settlement of soils in saturated or dry conditions presents a worst-case scenario, the settlement of partially-saturated soils during dynamic or earthquake loading is a topic that should be investigated because finite settlements will occur in these soils. Not only it is important to quantify the amount of settlement that will occur in a soil layer having a given degree of saturation, an improved understanding of the impact of the average degree of saturation in a given soil profile throughout the year on the amount of settlement during an earthquake can be considered to decrease the amount of conservatism in designs for seismically induced settlement of soils.

Another important reason for research on this topic is that there are different mechanisms governing earthquake-induced deformations in partially-saturated soils than in dry or

saturated soils. On one hand, the presence of pore air can have a significant impact on the deformation response of a soil layer due to its greater compressibility than that of water. On the other hand, the presence of air-water menisci in partially-saturated soils will increase the inter-particle contact forces and potentially resist compression during shaking.

Although there have been some limited design approaches for consideration of earthquake-induced settlement of partially-saturated soil layers, they deserve further development. Stewart and Whang (2003) and Duku et al. (2008) evaluated the seismic compression of partially-saturated soils, which is defined as the volumetric strain in an element of partially-saturated soil during cyclic or earthquake loading. Although the evaluation of results of series of cyclic simple shear tests on partially-saturated sands by Duku et al. (2008) indicate that the degree of saturation doesn't play an important role on the magnitude of seismic compression, the method of suction control in their tests may have contributed to this observation which contradict expectations from effective stress evaluations on partially-saturated soils. In addition, the lack of a trend with degree of saturation contradicts the results from several studies who reported the impact of degree of saturation or matric suction on the small strain shear modulus of partially-saturated soils (Cabarkapa et al. 1999; Mancuso et al. 2002; Kim et al. 2003; Inci et al. 2003; Mendoza et al. 2005; Vassallo et al. 2007; Sawangsuriya et al. 2009; Ng et al. 2009; Khosravi et al. 2010). The trends in small strain shear modulus with these variables will also lead to changes in the modulus reduction curve, indicating that the degree of saturation and matric suction should play a role in the magnitude of seismic compression during earthquake shaking.

If a geotechnical system (i.e., embankments, foundation, retaining wall, etc) is designed assuming water-saturated conditions for the soil, it is likely that the system will be able to withstand seismic loads if the soil is partially-saturated. However, this assumption may lead to over-conservative, costly design. Some design is still needed, especially because settlements will occur during shaking of partially-saturated soils. Specifically, performance-based design

involves comparison of the predicted response of a partially-saturated soil to earthquake shaking with a given performance criterion (i.e., a certain amount of settlement, or liquefaction). Further, if there is a quantitative assessment of the settlement in partially-saturated soil, remediation techniques can be evaluated from a more objective viewpoint to prevent liquefaction and can be performed with more scientific background.

An important difference between the behavior of saturated and partially-saturated soils to earthquake shaking is that the hydraulic conductivity of partially-saturated soils is less than that of saturated soils. Accordingly, during earthquake loading, partially-saturated soils are expected to behave in a more undrained manner than saturated soils. Further, an increase in pore water pressure due to shear loading will certainly cause water flow, which will be governed by the hydraulic conductivity of the partially-saturated soil. An important implication is that the time for dissipation of earthquake-induced pore water pressures will be longer in partially-saturated soils, which may lead to greater pore pressure accumulation in partially-saturated soils during earthquakes and aftershocks in combination with any collapse of pore air that increases the degree of saturation.

1.2 Research Objectives

The objective of this study is to characterize the mechanisms of seismically induced settlement of partially-saturated sands, and to evaluate the suitability of an empirical design methodology to predict the amount of settlement in free-field soil layers during earthquake or cyclic shaking.

1.3 Research Approach

In this research an effective stress-based empirical methodology is proposed to predict the earthquake induced settlement of free-field partially-saturated sand layers. This methodology uses a complex coupling between stress state, seismic compression, and pore water pressure generation during earthquake loading. In all of the different mechanisms considered in this methodology, the concept of effective stress plays an important role. Terzaghi (1943) was

one of the early researchers to propose that settlement of water-saturated or dry soils is directly related to the effective stress. In both water-saturated and dry soils, the effective stress is approximately equal to the difference between the total stress arising from the self-weight of the soil and any surcharge loading and the pore water pressure (zero for dry soils). The effective stress equation for partially-saturated soils based on the concept proposed by Lu et al. (2010) and Khalili and Zargarbashi (2010) was implemented in this approach.

Accordingly, an experimental study on partially-saturated soils was performed to be used in tandem with this design model to verify the induced settlement estimated using the proposed empirical methodology. A new centrifuge physical modeling technique was developed to evaluate the settlement of free-field soil layer within a laminar container during cyclic loading induced using a hydraulic servo-controlled shake table. Steady-state infiltration of water was used to control the stress state in the partially-saturated sand layer during centrifugation in the laminar container. Specifically, infiltration was used because previous studies found that it leads to a relatively uniform degree of saturation with depth in the sand layer (Zornberg and McCartney 2010), which helps simplify interpretation of the deformation response. Instrumentation was incorporated into the laminar container setup to measure the induced acceleration time histories of the shake table and laminar container, surface settlements, volumetric water content profiles, and pore water pressure generation for sand layers having different degrees of saturation under cyclic loading.

Sand layers with a wide range of degrees of saturation were evaluated using this approach to assess the effect of stress state and degree of saturation on their deformation response during cyclic loading. Small strain dynamic shear modulus is a key parameter in evaluating the seismically induced settlement of a soil layer. Resonant column test as an element scale test and shear wave measurement using bender elements as a geo-physical technique was used to measure the small strain dynamic shear modulus of the soil.

1.4 Dissertation Organization

A review of the literature related to the topic of this research is presented in Chapter 2. This chapter includes a review on the dynamic properties of sands. Then, the efforts to characterize and estimate the seismic settlement of dry and saturated sands are evaluated. In addition, the behavior of partially-saturated sand is discussed along with the effective stress concept of partially-saturated sands. After reviewing general dynamic properties of sands and behavior of partially-saturated sands, saturation effect on cyclic parameters and liquefaction resistance of sands are presented. Further, studies on seismic compression of partially-saturated sand are introduced and their performance is evaluated. Centrifuge modeling technique and its corresponding features and concerns, and shear wave velocity measurement using bender elements are the two final discussions in this chapter.

The material properties of the sand used in this study are described in Chapter 3. Specifically, the measurement of the geotechnical, hydraulic and dynamic properties of the sand are presented. The process of developing the empirical methodology to estimate the seismically induced settlement of partially-saturated sand is described in Chapter 4. The importance of the evaluation of the seismically induced settlement of partially saturated sand is explained in this chapter. Then, mechanisms of settlement in partially saturated sand are explored and their differences with the dry and saturated sands are discussed. The step by step calculation process and the corresponding equations are presented. Further, the estimated settlements are shown for an example application. A parametric evaluation is presented to show the effects of different parameters on seismically induced settlement.

The description of a new physical modeling testing approach for partially-saturated soils is explained in Chapter 5. This chapter includes an explanation of the theoretical basis for the use of steady-state infiltration to reach a uniform degree of saturation throughout the depth of the sand layer. Then, an overview of the centrifuge and shake table testing facilities at CU Boulder used as part of this study is presented. Chapter 5 also includes a detailed description of

testing setup in the laminar container, including a description of the instrumentation and specimen preparation method. In addition, the infiltration process is explained and the theoretical and experimental steady-state infiltration results were compared.

Bender elements were used to evaluate the dynamic shear modulus of the soil during steady-state infiltration during centrifugation. This approach is used to evaluate that the infiltration approach leads to soil layers having different dynamic properties. The bender element set up description and instrumentation specifications are presented in Chapter 6. The results of dynamic shear modulus of the sand measured using the bender element testing approach, are presented in this chapter. The measured dynamic shear modulus is compared with the conventional empirical equations and the resonant column test results.

The cyclic testing procedures including the loading conditions and test schedule and the measurements recorded are described in Chapter 7. The performance of the laminar container is evaluated and then the cyclic test results are analyzed. The results include induced settlements in specimens having different degrees of saturation, accelerations at different depths, and excess pore water pressures. In addition, a few cyclic tests were performed using a substitute pore fluid and the results are compared with the case where water was used as the pore fluid. The predicted results using the empirical methodology were compared with experimental data and the ways to improve the empirical method were proposed.

A summary of the approach to reach the objectives of this study, conclusions drawn from the results, and issues proposed for future research are presented in Chapter 8. A MATLAB code which implements the empirical methodology developed in this study is presented in Appendix A.

CHAPTER II

BACKGROUND

2.1 Dynamic Properties of Sand

The stress-strain behavior of soils can be approximated by different approaches such as hyperbolic curve as illustrated in Figure 2-1. The hyperbolic curve is usually defined by two parameters including slope at zero strain (G_{max}) and asymptote at large strain (shear strength, τ_{max}). In a cyclic nonlinear model, this curve is referred to as the backbone curve.

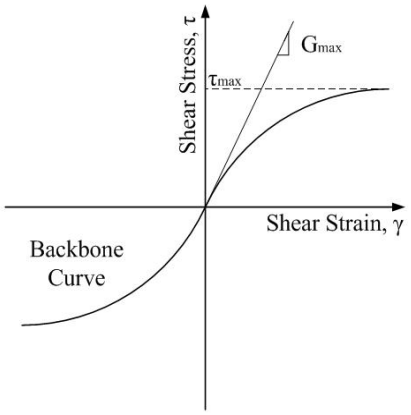

Figure 2-1. Backbone curve showing typical stress-strain behavior of soils

A soil subjected to shear stress tends to soften during application of shear strain. This is reflected in the shape of the backbone curve, which tends to decrease in slope with increasing shear strain (γ). The small strain shear modulus is defined as the shear modulus at strain amplitudes less than 10^{-6} (Kramer 1996). The small strain shear modulus is referred to as G_{max} because it is the highest modulus of the soil under a given effective stress and void ratio.

Although G_{max} is most commonly computed from the stress-strain curve, it should be noted that it can also be computed as a function of the shear wave velocity. Specifically, G_{max} can be computed as follows:

(2-1) $$G_{max} = \rho v_s^2$$

where ρ is the total density of the soil and v_s is the shear wave velocity of the soil.

Early studies on the dynamic properties of soils found that G_{max} is closely related to the mean effective stress, as well as stress history (quantified by the over-consolidation ratio, OCR), and void ratio (Hardin and Black 1969 and Hardin 1978). Hardin (1978) proposed a multiplicative form of a predictive equation for G_{max}:

(2-2) $$G_{max} = AF(e)(OCR)^k p_a^{1-n}(\sigma_m^{'})^n$$

where A is a constant value, F(e) is a void ratio function, OCR is the over-consolidation ratio, k is an over-consolidation ratio exponent, σ_m' is the mean effective stress, n is a stress exponent, and p_a is atmospheric pressure. The mean effective stress can be defined as a function of the vertical effective stress as $\sigma_m' = [(1+2K_0)/3]\ \sigma_v'$, where K_0 is the coefficient of earth pressure at rest. Hardin and Richart (1963) used Equation 2-2 to define the value of G_{max} for dry, round-grained Ottawa sand, as follows:

(2-3) $$G_{max} = 700\frac{(2.17-e)^2}{1+e}(\sigma_m^{'})^{0.5}$$

Later Hardin and Drnevich (1972) proposed Equation 2-4 for dry sands.

(2-4) $$G_{max} = 1230\frac{(2.97-e)^2}{1+e}(\sigma_m^{'})^{0.5}$$

Seed and Idriss (1970) correlated the value of G_{max} with mean effective stress and the relative density of the soil and proposed an empirical relationship for sands as expressed in Equation 2-5.

(2-5) $$G_{max} = K(\sigma_m^{'})^{0.5}$$

where K is a parameter that depends on sand relative density and σ'_m is the mean effective stress. σ'_m and G_{max} in Equation 2-3 to 2-5 has units of kg/cm^2, psi, and psf respectively. Iwasaki et al.

(1978) expressed G_{max} for dry sands at very low strain levels as in Equation 2-6 and 2-7,

(2-6) $$G_{max} = 850\frac{(2.17-e)^2}{1+e}(\sigma_m^{'})^{0.44} \quad for \quad \gamma = 10^{-5}$$

(2-7) $$G_{max} = 900\frac{(2.17-e)^2}{1+e}(\sigma_m^{'})^{0.4} \quad for \quad \gamma = 10^{-6}$$

The shear modulus reduction of the sand at higher shear strain amplitudes is expressed using the shear modulus reduction curve, as shown in Figure 2-2(a). In non-linear stress-strain behavior, the shear modulus (G) at each strain level can be obtained from the slope of the hyperbolic stress-strain curve. It should be considered that this loss of strength is different than what is happening in fully saturated specimen under dynamic loading where the generated excess pore water pressure decreases the effective stress and consequently the strength. Ishibashi and Zhang (1993) expressed the shear modulus reduction function as follows:

(2-8) $$\frac{G}{G_{max}} = K(\gamma, PI)(\sigma_m^{'})^{m(\gamma,PI)}$$

where K and m are parameters related to the unit weight and plasticity index of the soil. When a shear wave is traveling through the soil, it has some energy dissipation and damping. As shear modulus is affected by shear strain, damping ratio also varies for different strain levels as it is shown in Figure 2-2(b).

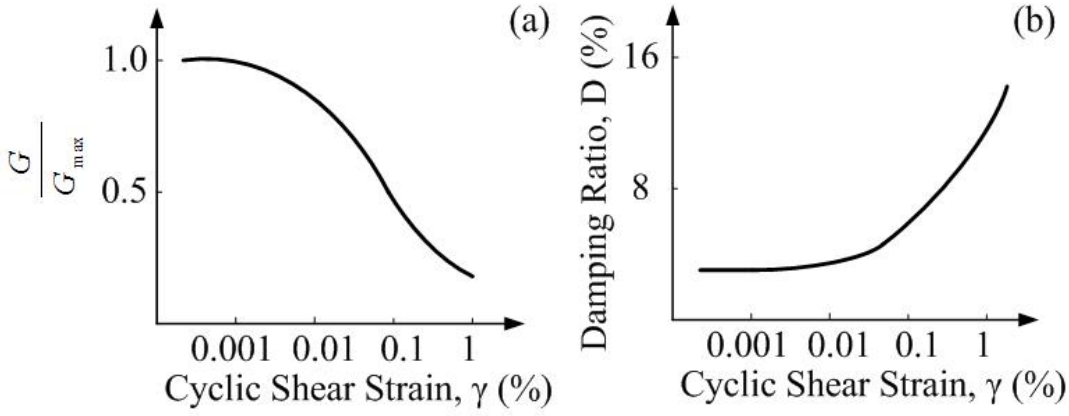

Figure 2-2. (a) Shear modulus reduction curve; (b) Material damping ratio curve

Stokoe et al. (2004) presented Equation 2-9 based on the hyperbolic equation proposed by Hardin and Drnevich (1972), as follows:

$$\frac{G}{G_{max}} = \frac{1}{1+\left(\frac{\gamma}{\gamma_r}\right)^a} \quad (2\text{-}9)$$

where γ is the shear strain, γ_r is the reference shear strain which is the shear strain that caused $G/G_{max}=0.5$, and "a" is a fitting parameter. Many investigators including Hardin and Drnevich (1972) simplified Equation 2-9 by assuming a = 1. Iwasaki et al. (1978) expressed γ_r as follows:

$$\gamma_r = \frac{\tau_{max}}{G_{max}} \quad (2\text{-}10)$$

where the value of τ_{max} can be defined as in Equation 2-11 using a value of a = 1.

$$\tau_{max} = \left[\left\{\left(\frac{1+K_0}{2}\right) sin\,\emptyset\right\}^2 - \left(\frac{1-K_0}{2}\right)^{1/2}\right]\sigma_v^{'} \quad (2\text{-}11)$$

where K_0 is the coefficient of earth pressure at rest, Φ is the soil friction angle, and σ_v' is the vertical effective stress. Menq et al. (2003) summarized results of some resonant column and torsional shear tests and defined the value of γ_r as follows:

$$\gamma_r(\%) = 0.12C_u^{-0.6}\left(\frac{\sigma^{'}}{p_0}\right)^{0.5C_u{}^{-0.15}} \quad (2\text{-}12)$$

Menq et al. (2003) also defined the value of a to be:

$$a = 0.86 + 0.1\,log\left(\frac{\sigma^{'}}{p_0}\right) \quad (2\text{-}13)$$

where σ' is the effective stress, p_0 is the atmospheric pressure, and C_u is the uniformity coefficient of the material. After defining the shear modulus reduction curve parameters, the shear modulus and the corresponding shear strain can be calculated using the shear modulus reduction function and stress-strain equation ($\gamma=\tau/G$). On the other hand, some researchers (Pradel 1998, Stewart and Whang 2003) proposed an explicit equation for the shear strain using the experimental shear strain data, as follows:

$$\gamma = \frac{1 + a \times e^{b.\frac{\tau_{ave}}{G_{max}}}}{1+a}.\frac{\tau_{ave}}{G_{max}} \quad (2\text{-}14)$$

where a and b are the model parameters and τ_{ave} is the average induced shear stress. Pradel (1998) expressed the model parameters based on the data by Iwasaki et al. (1978), as follows:

$$a = 0.0389\left(\frac{p}{p_0}\right) + 0.124, \quad b = 6400\left(\frac{p}{p_0}\right)^{-0.6} \quad (2\text{-}15)$$

Stewart and Whang (2003) developed similar equations based on the data by Stokoe and Darendeli (2001) for the shear modulus reduction curves. These equations are as follows:

$$a = 0.199\left(\frac{\sigma'}{p_0}\right)^{0.231} \quad , \quad b = 10850\left(\frac{\sigma'}{p_0}\right)^{-0.410} \tag{2-16}$$

2.2 Seismic Settlements of Dry Sands

Most early research studies on seismic settlement of sand layers were performed in dry conditions. At that time, it was believed that the settlement of dry or moist sands can happen during earthquake due to compression of the void space (Silver and Seed, 1971). D'Appolonia (1968) reported that there is a threshold horizontal acceleration (e.g., 1g) for a sand specimen to densify. The first attempt to investigate the settlement of dry sand under cyclic loading was performed by Youd (1970). He mounted the base of a direct shear apparatus on a vibrating table and confirmed the concept of the threshold horizontal acceleration. Since most of the accelerations during earthquakes are under 1g, further research was necessary to estimate the densification of sands due to earthquake vibrations. Silver and Seed (1971) examined the volume changes in sands under cyclic loading.

After studying the effects of cyclic shear strain, number of cycles, confining pressure and relative density on the settlements of sands, Seed and Silver (1972) suggested an approximate procedure to calculate the settlement of dry sand under earthquake loading. According to them, the vertical settlement of a sand layer can be obtained by knowing overburden pressure, cyclic strain, and number of cycles for each layer. They obtained the shear strain history at any depth using the equivalent linear method (to be explained later). Using this information and the results obtained from the simple shear tests, settlements can be estimated for each layer. Then, the total settlement is calculated by integrating differential settlement through the whole depth of the sand layer. They performed shake table tests to verify their analytical solution. An example of their results for shaking of medium dense sand is shown in Figure 2-3. They found that the measured and calculated values of settlement are generally in a good agreement, while in some cases they

differ by 50%. Figures similar to Figure 2-3 were plotted to show the effects of relative density, surcharge and base acceleration, with good correlations shown in all cases.

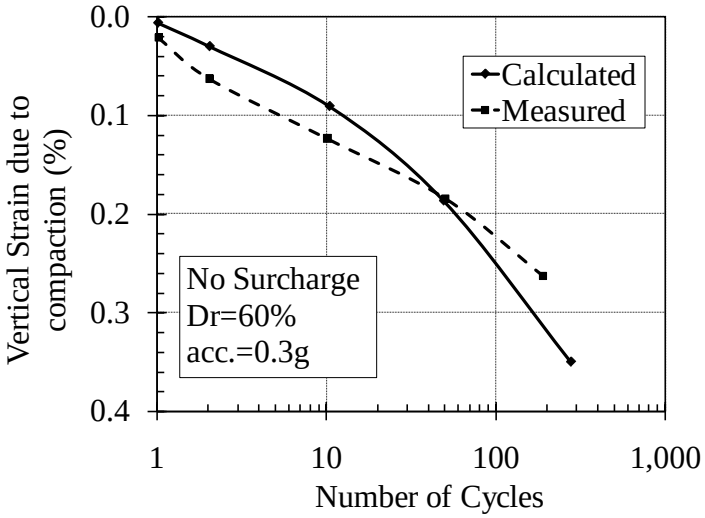

Figure 2-3. Comparison of measured and calculated settlements for medium dense sand layer due to base shaking (Seed and Silver 1972)

The difference in calculated and measured settlements observed in Figure 2-3 are likely due to the selection of the model input parameters or error in preparation density of the soil specimen. For example they varied the shear modulus profile through the soil layer and found that a small variation in the exponential power in shear modulus equation can lead to significant differences in the settlements as shown in Figure 2-4.

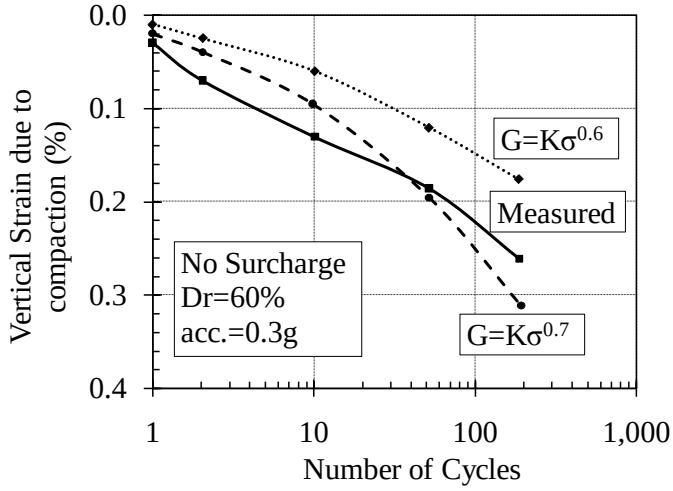

Figure 2-4. Effect of shear modulus exponential power on computed settlements (Seed and Silver 1972)

Finn and Byrne (1976) found that simple shear testing is time consuming and expensive, so they addressed the dynamic response of the soil using an analytical approach. They assumed a layer of soil to be a multi-degree of freedom system as shown in Figure 2-5. They lumped the mass of each layer and calculated the spring stiffness for each degree of freedom to be equal to shear modulus over height. A modal analysis was then performed by solving the equation of motion. They also studied the effect of a superstructure on the settlement of the sand layer and found that; firstly, the stiffness modulus of the soil was increased under the structure that decreases the settlement, and secondly, the presence of the structure produces more inertial forces due to the extra mass that increases the settlement. These results indicate that soils at shallow depths experience more settlement when a structure is present. However, deep layers were observed to experience the same amount of settlement regardless of the presence of the structure. They also mentioned the importance of incorporating a non-uniform soil density profile in estimating differential settlements.

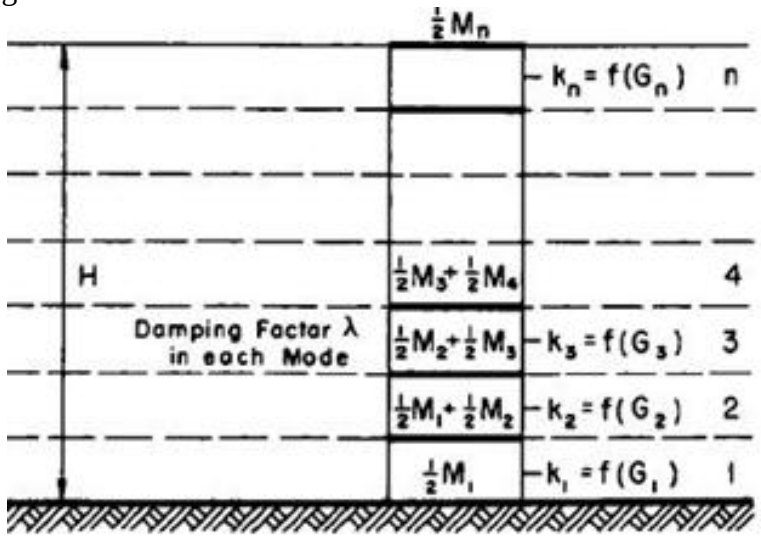

Figure 2-5. Discrete mass model for a soil layer (Finn and Byrne 1976)

Tokimatsu and Seed (1987) summarized the available data on seismic settlement of sand (Silver and Seed 1971; Seed and Silver 1972; Lee and Albaisa 1974). Later, Pradel (1998) formulized the plots proposed by Tokimatsu and Seed (1987) which has two main advantages.

First, only simple information such as the blow counts from the standard penetration test (SPT N-values) and earthquake characteristics are required. Second, a response analysis of the deposit is not required. Their method has following steps:

1. Divide the soil layer into n sub-layers.
2. Determine the average induced cyclic shear stress, τ_{ave} , for sub-layers as follows:

   (2-17) $$\tau_{av} = 0.65 \frac{a_{max}}{g} \sigma_0 r_d$$

   where a_{max} is the peak horizontal surface acceleration (a_{PSA}), σ_0 the initial total stress, and r_d is the induced stress reduction function.
3. Determine the maximum shear modulus of the soil, G_{max}, at the mid-point of each sub-layer using the mean effective stress at this depth.
4. Determine the compatible cyclic shear strain, γ, and shear modulus, G, using the values of τ_{ave}, G_{max}, and the shear modulus reduction function for each sub-layer.
5. Determine the volumetric strain, ε_v, which is a function of the cyclic shear strain, γ, and the earthquake magnitude, M, for each sub-layer. Pradel (1998) used the chart proposed by Tokimatsu and Seed (1987) based on the results published by Silver and Seed (1971) to relate the volumetric strain after 15 cycles and the normalized SPT-N ($N_{1\text{-}60}$) value as follows:

   (2-18) $$\varepsilon_{v-15} = \gamma \left(\frac{N_{1-60}}{20} \right)^{-1.2}$$

6. Tokimatsu and Seed (1987) provided a chart that expressed the relative density as a function SPT-N value as shown in Figure 2-6. The equation 2-18 is for 15 cycles which is corresponding to an earthquake of a 7.5 magnitude. The number of cycles corresponding to any earthquake magnitude (M) can be calculated using an expression developed by Tokimatsu and Seed (1987):

   (2-19) $$N = (M - 4)^{2.17}$$

7. The volumetric strain can be obtained for the corresponding number of cycles using a

relationship developed by Pradel (1998) based on the results of Silver and Seed (1971):

(2-20) $$\varepsilon_v = \varepsilon_{v-15}\left(\frac{N}{15}\right)^{0.45}$$

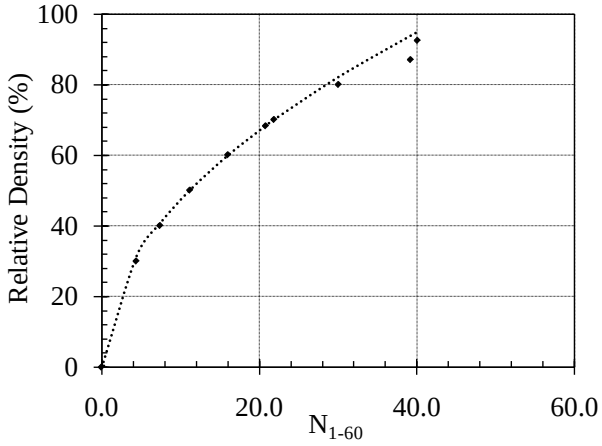

Figure 2-6. Relation between relative density and $N_{1\text{-}60}$ (Tokimatsu and Seed 1987)

8. Calculate the settlement of each sub-layer by multiplying the volumetric strain by the height of the layer.
9. Calculate the surface settlement by summing the sub-layer settlements.

Pyke et al. (1975) compared the results of settlement calculations using the method proposed by Seed and Silver (1972) and the actual settlements during an earthquake and found a significant difference between those two responses. Consequently, they studied the effect of the multidirectional shaking on the soil response using shake table tests. They concluded that shaking the specimen in both horizontal directions causes a settlement twice the amount when there is one directional shaking. They also found that vertical shaking doesn't cause any densification by itself, but it increases the settlement as much as 50% in comparison with the settlement under one directional shaking when it occurs in combination with other shaking directions. A comparison of the responses due to the different combination of shaking direction is shown in Figure 2-7.

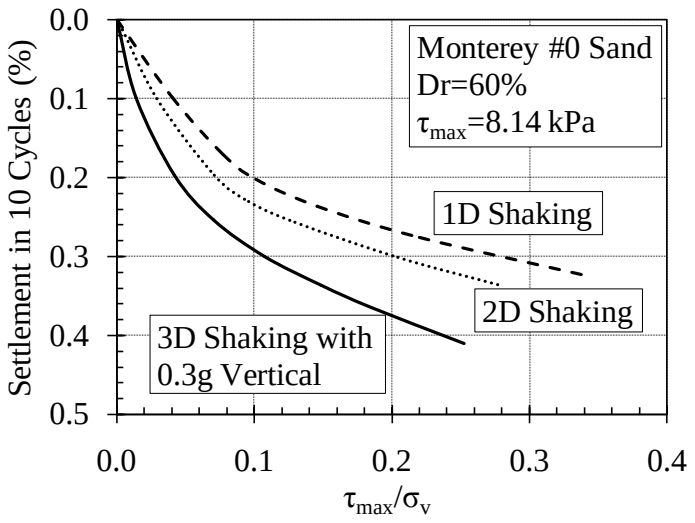

Figure 2-7. Relation between stress ratio and settlement due to different combination of shaking (Pyke et al. 1975)

Other approaches are available in the literature. Vincens et al. (2003) estimated the settlement of a soil layer by considering the continuum soil response under harmonic base excitation and particle rearrangement. They performed modal analysis and calculated maximum shear strain at each depth by summation of the different vibration modes contribution.

2.3 Seismic Settlements of Saturated Sands

Lee and Albaisa (1974) investigated the earthquake induced settlement of saturated sands. They found that even when the earthquake motion is not strong enough to create liquefaction, some excess pore pressure will develop and the subsequent dissipation may lead to settlements. The settlements before liquefaction are smaller than what happens during and after liquefaction. They found that the amount of volumetric strain after pore water dissipation for non-liquefaction conditions increases with larger soil grain sizes, decreasing the soil relative density, and increasing the pore water pressure generated during the undrained cyclic loading. The liquefaction resistance of sand is usually expressed in terms of τ_{ave}/σ'_0 where τ_{ave} is the average induced cyclic shear stress (obtained from Equation 2-14) and σ'_0 is the initial effective stress and is dependent on specimen preparation and stress history effects (Tokimatsu and Seed 1987). These effects are insignificant in post liquefaction when there are large strains.

To calculate the average induced shear stress Pradel (1998) developed an expression for the r_d function, as follows:

$$r_d = \frac{1}{1 + \left(\frac{d_c}{30.5m}\right)^2} \quad (2\text{-}21)$$

where d_c is the depth of the soil in meter.

Seed et al. (2001) also defined the value of r_d based on more extensive ground response analyses as follows:

$$if\ \ d_c < 20m \ => \ r_d = \frac{1 + \frac{a_1}{a_2}}{1 + \frac{a_1}{a_3}} \quad (2\text{-}22)$$

where

$$a_1 = -23.013 - 2.949\frac{a_{max}}{g} + 0.999M + 0.0053V_{s-d_c=12}$$

$$a_2 = 16.258 - 0.201e^{0.341(d_c + V_{s-d_c=12} + 7.586)}$$

$$a_3 = 16.258 - 0.201e^{0.341(V_{s-d_c=12} + 7.586)}$$

where d_c is the depth of the soil, M is the earthquake magnitude, and $V_{s\text{-}dc=12}$ is the shear wave velocity at a depth of 12 m.

Seed et al. (1984a) showed the correlation of the developed shear strain, cyclic stress ratio and settlement in 10 cycles as shown in Figure 2-8. Even though liquefaction may not occur, the dissipation of excess pore water pressure after incomplete liquefaction may cause settlements. Tokimatsu and Yoshimi (1983) presented a plot for excess pore-water pressure ratio versus normalized stress ratio as shown in Figure 2-9.

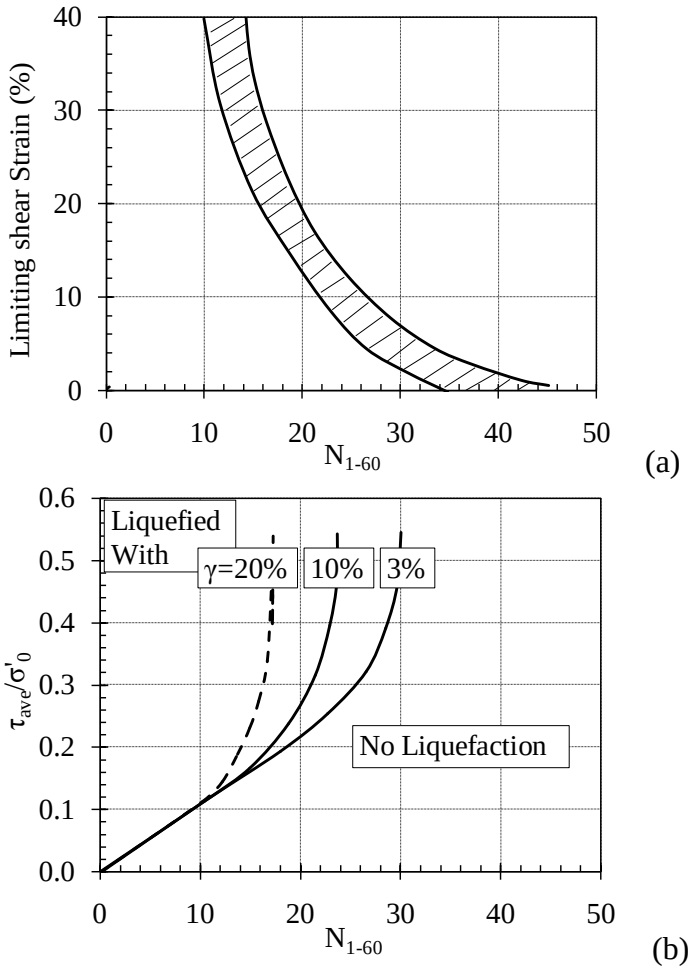

Figure 2-8. Correlations between dynamic soil response and standard penetration test measurements (N_{1-60}) (Seed et al. 1984a): (a) Limiting shear strain; (b) Cyclic stress ratio causing liquefaction

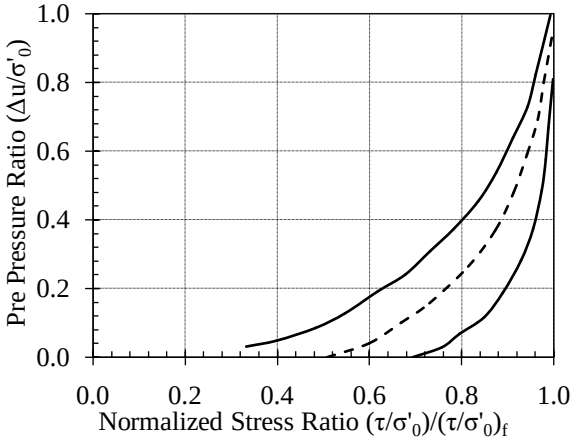

Figure 2-9. Relation between induced pore pressure ratio and normalized stress ratio for clean sands (Tokimatsu and Yoshimi 1983)

Lee and Albaisa (1974) expressed the volumetric strain as a function of induced pore water pressure for different relative densities shown in Figure 2-10. Higher pore water pressure ratios results in larger volumetric strains. The results in Figures 2-9 and 2-10 were combined to obtain the plot in Figure 2-11. The curves in Figure 2-11 can be used to calculate settlements for non-liquefied sand. When the stress ratio is 0.8 (factor of safety of 1.25) the volumetric strain is about 10%. Further, if the normalized stress ratio is less than 0.7 the effect of pore water pressure on settlement is insignificant. Most of the equations and plots are for an earthquake magnitude of 7.5. If the design earthquake is different, the stress ratio value should be corrected for that earthquake.

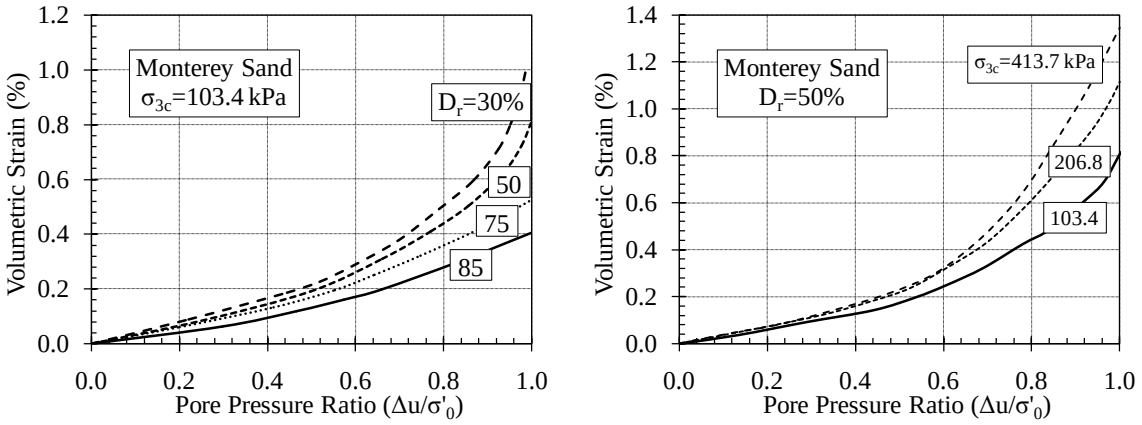

Figure 2-10. Relations between induced pore pressure ratio and volumetric strain (Lee and Albaisa 1974)

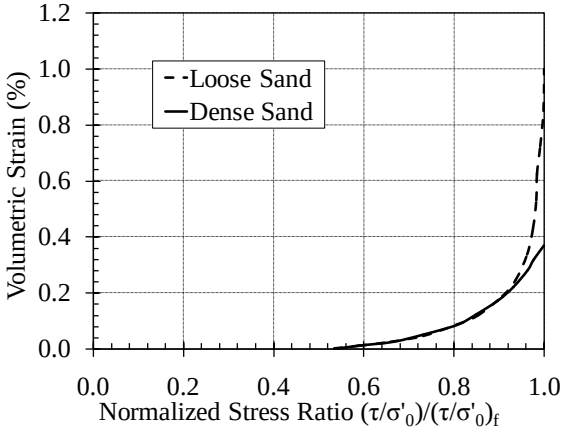

Figure 2-11. Relation between normalized stress ratio and volumetric strain (Tokimatsu and Seed 1987)

2.4 Effective Stress Concept in Partially-Saturated Sand

The mechanical and hydraulic behavior of soils and particulate materials is closely related to the inter-particle state of stress. Terzaghi (1943) was the first person who proposed the concept of "effective" stress in soil mechanics to account for inter-particle stresses. The effective stress variable ($\sigma'=\sigma-u$) was found to be useful in formulating the mechanical and hydraulic behavior of dry or saturated soils. The deformation behavior and strength of the soil are related to effective stress variable. Although the definition of the effective stress is unique for fully saturated or dry soils ($\sigma'=\sigma-u_w$), there are different methods to state the effective stress variable for partially-saturated soils. Whereas saturated soils contain two constituents (soil particles and pore-water), partially-saturated soils consist of three parts including soil particles, pore water and pore air. Bishop (1959) defined the effective stress in partially-saturated soils as follows.

$$\sigma' = \sigma - u_a + \chi(u_a - u_w) \tag{2-23}$$

where χ is the effective stress parameter, ($\sigma-u_a$) is the net normal stress and (u_a-u_w) is the matric suction.

A concept that builds upon Bishop's concept of a single stress state variable is that of the Suction Stress Characteristic Curve (SSCC) proposed by Lu and Likos (2006). They used the concept of the SSCC to define the effective stress of partially-saturated soils as in Equation 2-24 where suction stress is a function of matric suction. A typical suction stress characteristic curve for sand is shown in Figure 2-12.

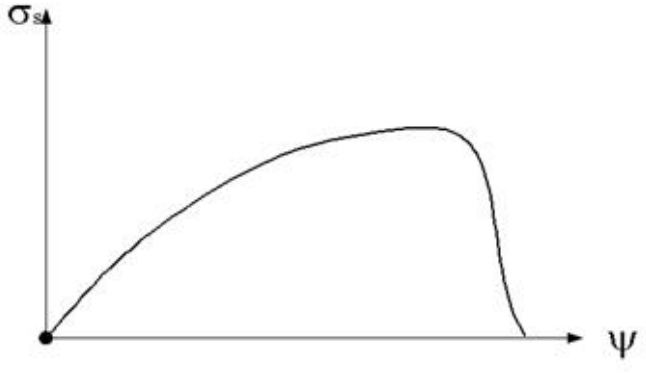

Figure 2-12. Typical SSCC for sand

(2-24) $$\sigma' = (\sigma_t - u_a) + \sigma_s$$

Lu et al. (2010) used theoretical and empirical analyses to define the suction stress as follows:

(2-25) $$\sigma_s = -S_e(u_a - u_w)$$

where S_e is the effective degree of saturation equal to $(S - S_r)/(1 - S_r)$, S_r is the residual degree of saturation, and u_w is the water pressure. The difference in pore water pressure and pore air pressure ($u_a - u_w$) is defined as the matric suction. Lu et al. (2010) showed how relationships between matric suction and the degree of saturation (i.e., the soil-water retention curve or SWRC) such as that of van Genuchten (1980) incorporated into Equation 2-25 to develop a functional form for the effective stress as follows:

(2-26) $$\sigma' = (\sigma - u_a) + \frac{u_a - u_w}{(1 + [\alpha_{vG}(u_a - u_w)]^{N_{vG}})^{(N_{vG}-1)/N_{vG}}}$$

where α_{vG} and N_{vG} are parameters for the van Genuchten (1980) SWRC model.

The effective stress can have a significant impact on the dynamic shear modulus of unsaturated soils. Since there is no unique effective stress state defined for partially-saturated soils, a dynamic shear modulus function is also not available. Consequently, validating the proposed effective stress states for partially-saturated soils and using them to estimate the dynamic shear modulus of the soil is important. The dynamic shear modulus function will be used to calculate the settlement of the partially-saturated sand under seismic loading.

2.5 Saturation Effect on Dynamic Properties of Partially-Saturated Sand

Hardcastle (1998) studied the effect of the degree of saturation on the maximum shear modulus and the shear modulus reduction of sandy loess. He showed a decreasing trend for shear modulus as the soil gets closer to fully saturated condition. Altun and Goktepe (2006) also studied the shear modulus for different degree of saturations and obtained the same results. Inci et al. (2003) showed that for cohesive or well graded soils the relation between the modulus and the suction pressure is proportional while Qian et al. (1991) showed an optimum value of the degree of saturation corresponding to the maximum modulus for cohesionless or poorly

graded soils as shown in Figure 2-13.

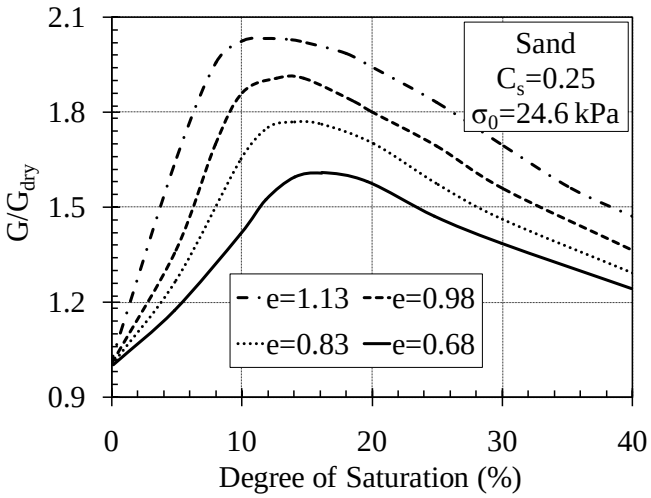

Figure 2-13. G/G_{dry} versus degree of saturation (Qian et al. 1991)

Michaels (2006) performed viscoelastic analyses to estimate viscous damping in partially-saturated soils and verified the results by field measurements. He modified the Kelvin-Voigt (KV) model to Kelvin-Voigt-Maxwell-Biot (KVMB) model (shown in Figure 2-14) and calculated the equivalent KV damping as a function of frequency as shown in Figure 2-15. The data shown in Figure 2-15 (theoretical curves) have an increasing trend followed by a decreasing trend. On the left side (low frequencies) the pore fluid and frame (soil skeleton) are coupled and moved together and damping is mostly affected by the fluid viscosity. Damping increases with increasing the frequency until it reaches a peak value where the relative inertial motion starts to dominate and damping begins to decrease. Also, higher degrees of saturation lead to higher damping.

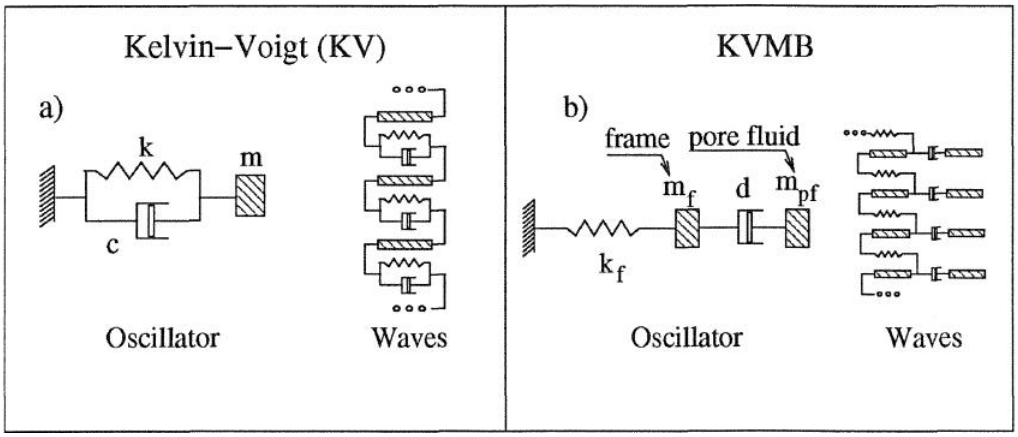

Figure 2-14. KV and KVMB models (Michaels 2006)

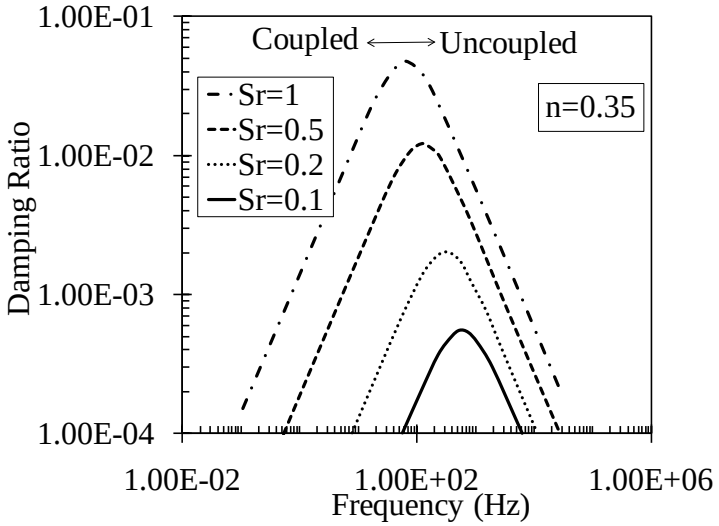

Figure 2-15. Equivalent KV damping ratio versus frequency (Michaels 2006)

2.6 Liquefaction Resistance of Partially-Saturated Sand

One of the first experimental studies on liquefaction potential of sands was performed by Rocker (1968). He performed cyclic triaxial tests and found that a small decrease in the degree of saturation led to an increase in the number of cycles of load application needed to cause liquefaction. Mulilis et al. (1976) performed cyclic triaxial tests and determined that the liquefaction strength of sand decreases approximately 10 percent as the B-value (pore pressure change over confining pressure change as a measure of degree of saturation) increases from 0.92 to 0.97. Chaney (1978) examined the saturation effect on cyclic resistance of sands to

liquefaction. He showed that when B-value is decreasing from 1.0 to 0.9, the number of cycles to cause 5% double amplitude axial strain increases 1.7 times and 16 times for dense and loose sands, respectively. The problem with using B-value is that it is also a function of soil structure, porosity, compressibility of pore water, the absolute pressure existing in the pore fluid and S_r.

In either saturated or partially-saturated soils there is a pore pressure build-up due to cyclic loading until failure. The amount of increase of pore pressure per cycle is a function of density of the soil, bulk density of pore fluid, rebound tangent modulus and reduction in volume of sand. Martin et al. (1975) presented the following equation:

$$\frac{\Delta u}{\varepsilon_{vd}} = \frac{1}{\frac{1}{E_r} + \frac{n}{K_{aw}}} \qquad (2\text{-}27)$$

where E_r is the rebound tangent modulus of a one dimensional unloading curve at a point corresponding to the initial vertical effective stress (approx. 104 psi), K_{aw} is the bulk modulus of air/water mixture, Δu is the increase in pore pressure increment per load cycle and $\Delta\varepsilon_{vd}$ is reduction in volume of sand structure due to slip deformation per load cycle. A parametric evaluation of Equation 2-27 is shown in Figure 2-16. Higher pore pressure is built up in a specimen with higher S_r. Also, testing the specimens under higher strain level caused more excess pore pressure.

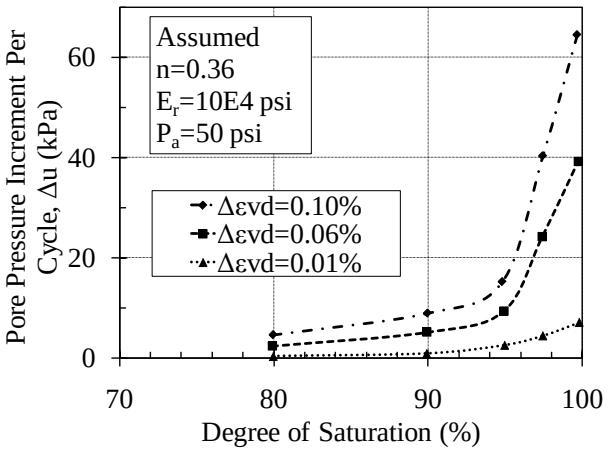

Figure 2-16. Pore pressure change due to change in degree of saturation (Chaney 1978)

Nagase and Ishihara (1988) studied the liquefaction-induced settlement of sand during earthquake. They explained that the volumetric strains depend on the amount of pore-pressure built-up when the soil did not liquefy. Yoshimi et al. (1989) presented the liquefaction resistance of partially-saturated sands and observed a decrease in the liquefaction resistance with increasing degree of saturation while the liquefaction resistance is always lower than static shear strength as in Figure 2-17 where DA is the double amplitude shear strain (peak to peak strain in cyclic loading).

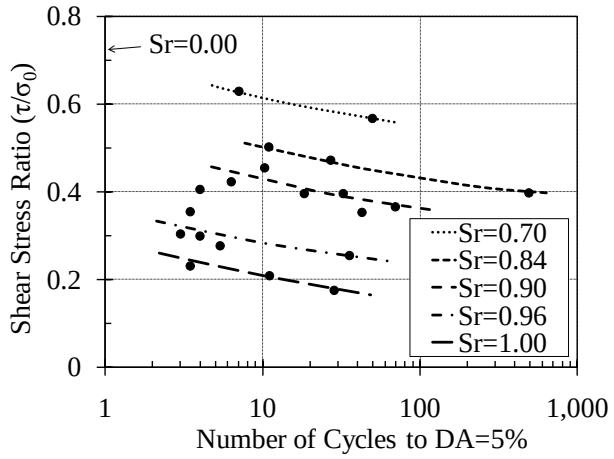

Figure 2-17. Effect of degree of saturation on liquefaction characteristics of sand (Yoshimi et al. 1989)

Loose sands are less resistant to liquefaction. The relation between degree of saturation and liquefaction resistance, R_u/R_s, where R_u is defined by the point coordinate on Figure 2-16 at 15 cycles and R_s is R for fully saturated specimen is shown in Figure 2-18. The liquefaction resistance at S_r=70% is about three times of that at fully saturated specimen.

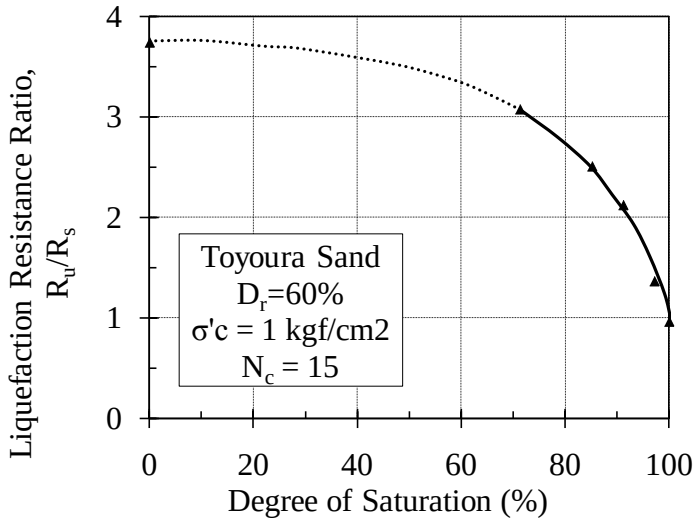

Figure 2-18. Relation between degree of saturation and liquefaction resistance ratio (Yoshimi et al. 1989)

Tsukamoto et al. (2002) proposed to use P- and S-wave velocities to measure degree of saturation instead of B-value because it can be measured both in the field and in the lab with the same credibility. Kokusho (2000) and Tsukamoto et al. (2002) correlated wave velocities with B-value and their work led to the following equations.

$$\left(\frac{V_p}{V_s}\right)^2 = \frac{4}{3} + \frac{2(1-\upsilon_b)}{3(1-2\upsilon_b)(1-B)} \quad (2\text{-}28)$$

where the value of υ_b can be defined as:

$$\upsilon_b = \frac{1}{2}\frac{3K_b - 2G_0}{3K_b + G_0} = \frac{1}{2}\frac{3 - 2G_0C_b}{3 + G_0C_b} \quad , C_b = \frac{1}{K_b} \quad (2\text{-}29)$$

where V_p is the P-wave velocity, V_s is S-wave velocity, υ_b is soil skeleton Poisson's ratio, B is B-value, G_0 is soil shear modulus at small strain (G_{max}) and C_b and K_b are soil skeleton compressibility and volumetric modulus. A summary of test results by Tsukamoto et al. (2002) is shown in Figure 2-19. It shows a decreasing trend for liquefaction resistance with increasing V_p or degree of saturation.

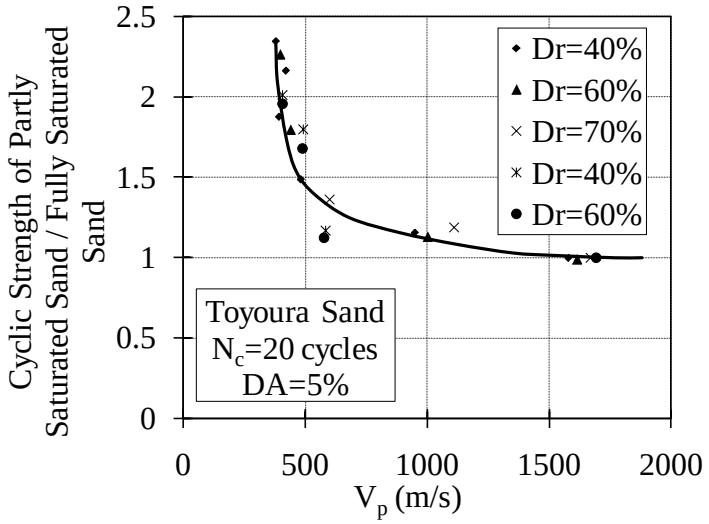

Figure 2-19. The normalized cyclic strength of sand versus P-wave velocity (Tsukamoto et al. 2002)

Okamura and Teraoka (2006) evaluated the effect of decreasing the degree of saturation as potential countermeasure against liquefaction. They prepared a box of saturated sand with a block on the surface and desaturated a zone under the block. Then, they applied excitation to the bottom of the box and measured the settlement of the block with different width of desaturated zone. Their results highlighting the effect of desaturation on liquefaction settlement are shown in Figure 2-20.

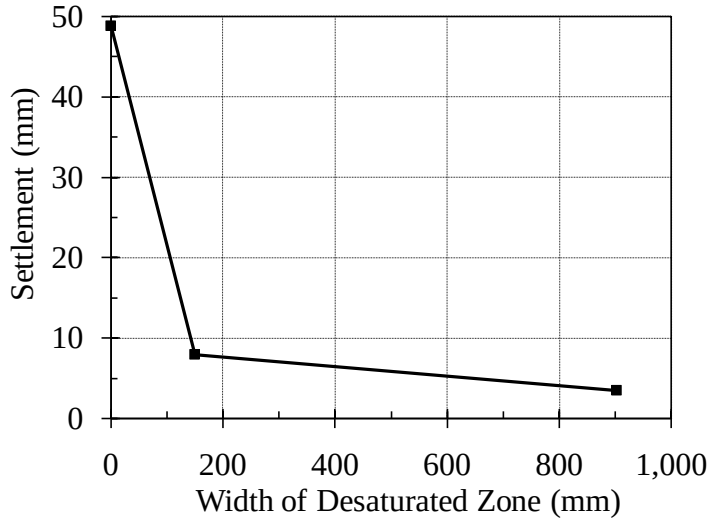

Figure 2-20. Settlement of block after shaking (Okamura and Teraoka 2006)

2.7 Seismic Compression of Partially-Saturated Sand

Although the significance of studying on dynamic response of partially-saturated soil is obvious from a fundamental perspective, this field has not got the appropriate attention. This is likely because saturated soils are generally considered a worst-case scenario in liquefaction analyses (Chaney 1978; Yoshimi et al. 1989), and also because of experimental difficulties in controlling the partially-saturated stress state in partially-saturated soils (Lu and Likos 2006). This is also because of difficulties in understanding drained and undrained behavior in partially-saturated soils. For example, in liquefaction analyses of saturated soils, if the earthquake loading is fast and with sufficient magnitude, the entire dynamic load are transmitted to the water. This will cause an increase in pore water pressure and a decrease in effective stress since water is comparatively incompressible. In partially-saturated soils, a percentage of the load is transmitted to the pore water (Chaney 1978) while the rest to the soil skeleton. Different from water-saturated soils, transmission of load to the soil skeleton will lead to collapse of air filled voids, leading to settlement even though pore water pressures may not increase. However, may be the matric suction balances out the tendency to collapse.

Stewart and Whang (2003) and Duku et al. (2008) evaluated the seismic compression of partially-saturated soils, which is defined as the volumetric strain in an element of partially-saturated soil during cyclic or earthquake loading. Although the evaluation of results of series of cyclic simple shear tests on partially-saturated sands by Duku et al. (2008) indicate that the degree of saturation doesn't play an important role on the magnitude of seismic compression, the method of suction control in their tests may have contributed to this observation which contradict expectations from effective stress evaluations on partially-saturated soils. In addition, the lack of a trend with degree of saturation contradicts the results from several studies who reported the impact of degree of saturation or matric suction on the small strain shear modulus of partially-saturated soils (Cabarkapa et al. 1999; Mancuso et al. 2002; Kim et al. 2003; Inci et al. 2003; Mendoza et al. 2005; Vassallo et al. 2007; Sawangsuriya et al. 2009; Ng et al. 2009;

Khosravi et al. 2010). Specifically, soil specimens with different degrees of saturation were prepared by tamping and kneading to a target relative density and the specimens were tested in constant water content conditions. Possible changes in degree of saturation, matric suction, and stress state during the test during compression of the voids may have contributed to the lack of a well-defined trend. According to the above discussions, a comprehensive study on seismic compression of partially-saturated sand is required considering element scale, physical modeling, and analytical approach.

2.8 Centrifuge Modeling

The purpose of centrifuge modeling is to produce a physical scaled model to simulate the real prototype model by increasing the acceleration levels proportional to the reduction of linear dimensions. The scaling relations defined by Ko (1988a) are shown in Table 2-1. The scaling relations (ratio of model to prototype quantity) for time are different for diffusion and dynamic phenomena. In centrifuge modeling of saturated or partially-saturated soils under dynamic loading phenomena both behaviors exist together, so there will be a scaling conflict. This problem can be resolved by making the diffusion event progress slower by either reducing the particle size (there by reducing the hydraulic conductivity) or by using a substitute pore fluid N times more viscous than water. Since the first approach changes the mechanical property of the model, the second approach is being used commonly in centrifuge modeling.

Dewoolkar et al. (1999) listed certain criteria for an ideal substitute pore fluid. To satisfy these criteria, different fluids were tested by different researchers including silicone oil, Glycerin-Water mixture, the Delft Geotechnics model pore fluid, and Methylcellulose. Dewoolkar et al. (1999) explained advantages and disadvantages of each substitute pore fluid and proposed methylcellulose (Metolose) as a good substitute pore fluid that has been used at the University of Colorado at Boulder for several years. The chemical properties of Metolose are available on Metolose Brochure (1997) and on the producer's website (Shinetsu Co.).

Table 2-1. Scaling relations for centrifuge modeling (Ko 1988a)

Quantity	Prototype	Model
Length	n	1
Area	n^2	1
Volume	n^3	1
Velocity	1	1
Acceleration	1	n
Mass	n^3	1
Force	n^2	1
Energy	n^3	1
Stress	1	1
Strain	1	1
Mass density	1	1
Energy density	1	1
Time (dynamic)	n	1
Time (diffusion)	n^2	1
Time (creep)	1	1

Dewoolkar et al. (1999) measured the viscosity of Metolose solutions using a standard capillary viscometer pre-calibrated with fluids of standard viscosities. They found that the viscosity of Metolose solution is fairly stable with time. Since the amount of Metolose powder dissolved in water is very small, the density of the Metolose solution is virtually the same as the water. Dewoolkar et al. (1999) conducted an evaluating program including triaxial compression tests, permeability tests and seismic centrifuge experiments on level ground plus modeling of model-type experiments with Metolose-saturated embankment and retaining wall models. As they proposed, the viscosity of Metolose is constant with time, increasing with increasing concentration, and decreasing with increasing temperature. Since the centrifuge facility at the University of Colorado at Boulder (Ko, 1988b) has a cooling system, temperature effects are not relevant. The surface tension of grade 90SH Metolose is about 75% of that of water (Metalose brochure 2007). Consequently, the use of Metolose should be investigated for partially-saturated sands. Further tests on strain rate, dynamic modulus and damping characteristics seem to be

necessary.

Although considerable research has been done on capillary rise phenomena (Lu and Likos 2004; Jirapinate et al. 2006), still there is a need to study the capillary rise in centrifuge modeling because the N-g gravitational acceleration may affect this phenomena. Within the Network of European Centrifuges for Environmental Geotechnics (NECER), scientists studied the scaling relations of the capillary rise (from dry to wet condition) of water through the soil including capillary height, rising velocity and rising time and showed that the scaling factor for capillary rise is 1/N (Rezzoug at al. 2004). Their tests' objective was to provide a water table boundary condition to an initially partially-saturated sand column and observe the evolution of capillary rise at different g-levels. Their result which shows a satisfactory agreement in the comparison of the theoretical and experimental scaling factors is demonstrated in Figure 2-21.

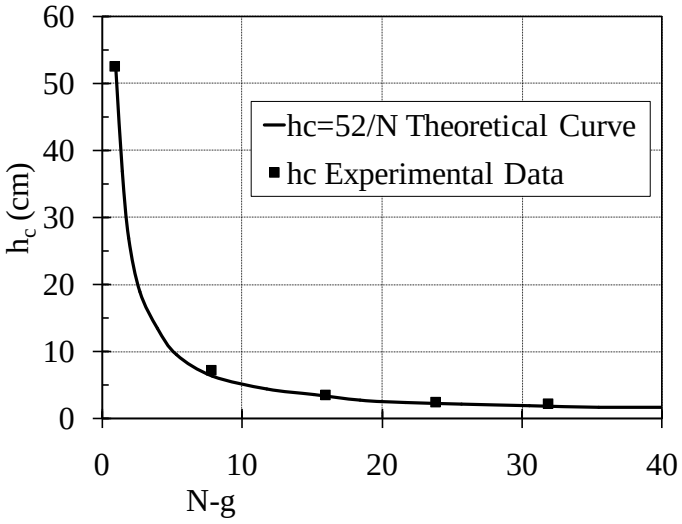

Figure 2-21. Capillary rise variation at different g-level (Rezzoug et al. 2004)

2.9 Shear Wave Velocity Measurement Using Bender Element

Nondestructive assessment of soil properties is a developing area in geotechnical engineering. In centrifuge modeling in particular, it is often required to measure changes in soil density nondestructively after different stages of testing (before and after shake table testing, before and after insertion of a pile foundation, etc.). Bender elements apply shear strains having

small strain magnitudes to soil layers through the use of piezoelectric ceramics. Piezoelectric materials deform during application of a voltage difference, or generate a voltage difference when deformed. Bender elements are typically constructed from sheets of piezoelectric ceramic bonded together and connected electrically in a series or parallel configuration to obtain different polarizations. Specifically, parallel-connected benders are used for sending signals while series-connected are used for receiving signals. When a voltage signal is applied to a sending element, a shear wave will be induced in the surrounding soil, which can be detected using a receiving element located at a known distance from the sending element. Shear wave velocity can be measured using a pair of bender elements by measuring the time difference between sending and receiving shear waves from one bender element to another. Then, the small-strain shear modulus can be calculated using Equation 2-1.

Since Shirley and Hampton (1978) introduced bender elements to soil testing, bender elements have been incorporated into many conventional geotechnical tests, including triaxial tests (Bates 1989; Brignoli et al. 1996; and Pennington et al. 2001), resonant column tests (Dyvik and Madshush 1985), oedometer tests (Dyvik and Madshush 1985; Kawaguchi et al. 2001), direct simple shear tests (Dyvik and Madshush 1985), true-triaxial tests (Agarwal and Ishibashi 1991), and large container tests (Blewett et al. 2000). Andrus and Stokoe (2000) also used bender elements in the field for liquefaction resistance evaluation. Concerns such as electromagnetic cross-talk, in-plane and out-of-plane directivity, bender resonant frequency, and effects of reflections from boundaries have also been addressed in laboratory and theoretical studies (Arulnathan et al. 1998; Greening and Nash, 2004; Lee and Santamarina 2005; Leong et al. 2005).

Bender elements have a long history for measurement of G_{max} of saturated or dry soils (Shirley and Hampton 1978; Dyvik and Madshus 1985; Bates et al. 1989; Argawal and Ishibashi 1991; Brignoli et al. 1996; Arulnathan et al. 1998; Pennington et al. 2001; Leong et al. 2005) and unsaturated soils (Cabarkapa et al. 1999; Inci et al. 2003; Marinho et al. 2005; Alramahi et

al. 2007; Ng and Yung 2008; Sawangsuriya et al. 2009, Ng et al. 2009) in laboratory tests because they induce and measure low shear strains and are relatively compact in size. Several studies have used bender elements to study the impacts of matric suction, degree of saturation, and hydraulic hysteresis on the magnitude of G_{max} for partially saturated soils (Cabarkapa et al. 1999; Inci et al. 2003; Marinho et al. 2005; Alramahi et al. 2007; Ng and Yung 2008; Sawangsuriya et al. 2009, Ng et al. 2009). Most of these studies focused on the behavior of compacted soils. Hoyos et al. (2008) compared G_{max} measurements from bender element and resonant column tests and found that G_{max} measurements from the bender element test were generally higher than those from the resonant column test, especially under higher confining pressures.

Bender elements have been also used in centrifuge modeling tests as well, primarily for the purpose of shear wave velocity tomography to infer zones of densified soil (Ismail and Hourani 2003; Lei et al. 2004; Brandenberg et al. 2006; Rammah et al. 2006; Kim and Kim 2010). However, their use in partially saturated soils in the centrifuge deserves further investigation.

CHAPTER III

MATERIAL CHARACATERIZARTION

3.1 Geotechnical Properties

F-75 Ottawa sand was selected for use in this study because it has relatively high saturated permeability (about 6×10^{-4} cm/s at the target void ratio used in this test), while still having fine enough soil particles to retain water over suctions up to 10 kPa. The geotechnical properties of this fine silica sand are summarized in Table 3-1 and the grain size distribution obtained from the sieve analysis tests is shown in Figure 3-1.

Table 3-1. Geotechnical Properties of F-75 Ottawa Sand

Property	**Description**
Mineralogy	Quartz, 99.8% SiO_2
Grain shape	Rounded
Specific gravity, G_s	2.65
Surface area	162 cm^2/g
C_u	1.71
C_c	1.01
e_{min}, e_{max}	0.49, 0.80
ρ_{min}, ρ_{max}	1469, 1781 kg/m^3
$K_{saturated}$ (Hydraulic Conductivity)	6×10^{-4} cm/s

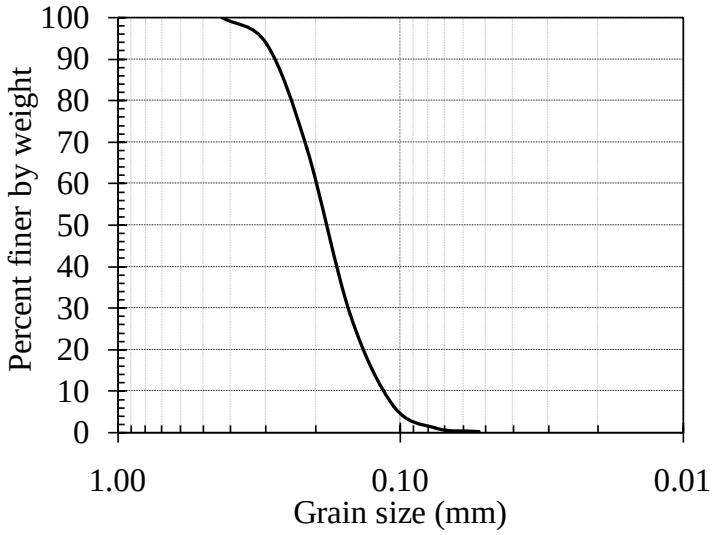

Figure 3-1. Grain size distribution of F-75 Ottawa Sand

3.2 Hydraulic Properties

The Soil Water Retention Curve (SWRC) of F-75 Ottawa sand was measured using a hanging column test with controlled outflow (McCartney et al. 2008). A schematic of the test is shown in Figure 3-2. In this test, increments of suction are applied to the base of soil specimen by lowering the water level in a manometer tube connected to a high air-entry porous disc (a Büchner funnel). The difference of this hanging column from others is that the outflow can be measured under constant suction through the use of a Mariotte bottle attached to the outflow side of the hanging column. A point on the SWRC may be defined by applying an increment of suction to an initially water-saturated specimen, then subsequently recording outflow reaching equilibrium. This step can be repeated for different suction levels. The volumetric water content can be back-calculated using outflow data at each step and the final volumetric water content.

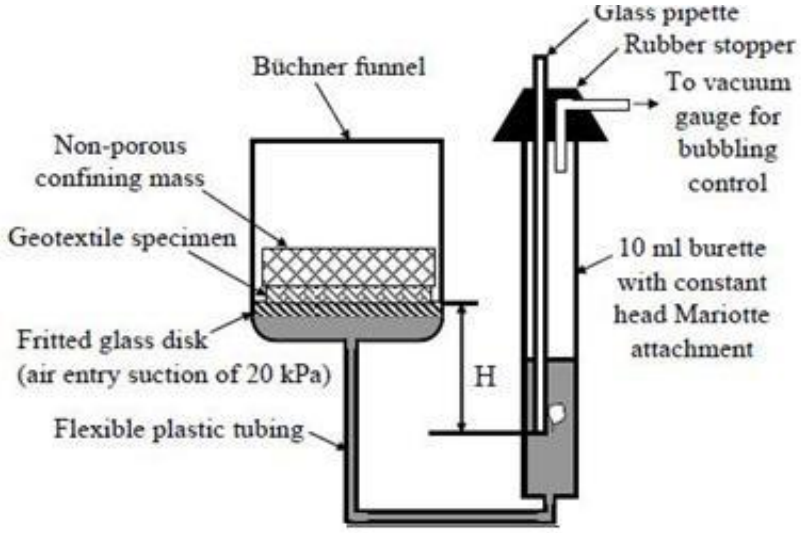

Figure 3-2. The schematic of hanging column test apparatus (McCartney et al. 2008)

The SWRC measured for F-75 Ottawa sand is shown in Figure 3-3 along with the van Genuchten (1980) SWRC model as it is expressed in Equation 3-1, which was fitted to the experimental data using least-squares regression.

$$\theta = \theta_r + (\theta_s - \theta_r)\left[\frac{1}{1+(\alpha_{vG}\Psi)^N}\right]^{\left(1-\frac{1}{N_{vG}}\right)} \tag{3-1}$$

The hydraulic conductivity function (HCF) was estimated using the van-Genuchten-Mualem model (van Genuchten 1980) shown in Equation 3-2. The fitting parameters for the van Genuchten SWRC model were found to be θ_r=0.04, θ_s=0.397, N_{vG}=7, and α_{vG}=0.24. The slope of the predicted HCF was used to estimate Gardner's α_G parameter for F-75 Ottawa sand, which was found to be 2.5 kPa^{-1}.

$$K = K_s \frac{\left[1-(\alpha_{vG}\Psi)^{N_{vG}-1}\left(\frac{1}{1+(\alpha_{vG}\Psi)^{N_{vG}}}\right)^{\left(1-\frac{1}{N_{vG}}\right)}\right]^2}{[1+(\alpha_{vG}\Psi)^{N_{vG}}]^{\left(\frac{1}{2}\left(1-\frac{1}{N_{vG}}\right)\right)}} \tag{3-2}$$

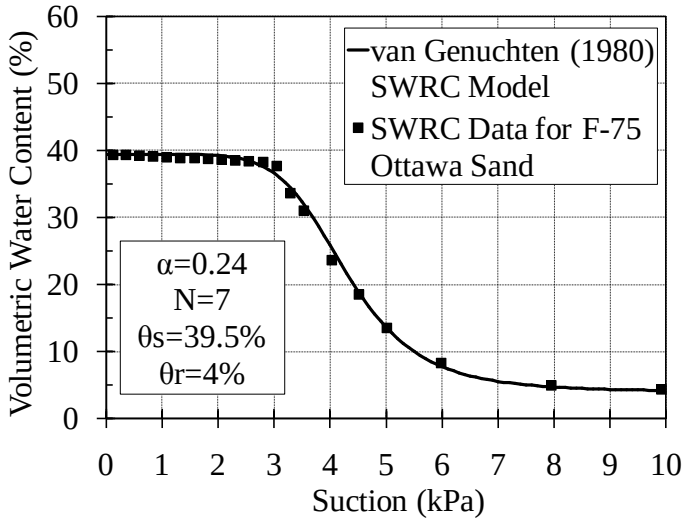

Figure 3-3. SWRC of F-75 Ottawa Sand

3.3 Dynamic Properties

3.3.1 Resonant Column Device

A fixed-free Stokoe-type resonant column device with suction-control capabilities was developed at the University of Colorado at Boulder. The overall layout of this system is shown in Figure 3-4. This new apparatus allows control of the total confining pressure and matric suction, two key components of the effective stress of partially-saturated soils (Equation 2-16). Air pressure is used to impose the cell pressure through a water bath around the specimen while the diffusion of air is limited by placing vacuum grease between a thin double latex membrane surrounding the soil specimen. The pore air pressure in the soil specimen is vented to atmosphere, so it is considered to be zero. The pore water pressure in the specimen is controlled using the hanging column technique with controlled outflow as explained in Section 3.2 (McCartney et al. 2008).

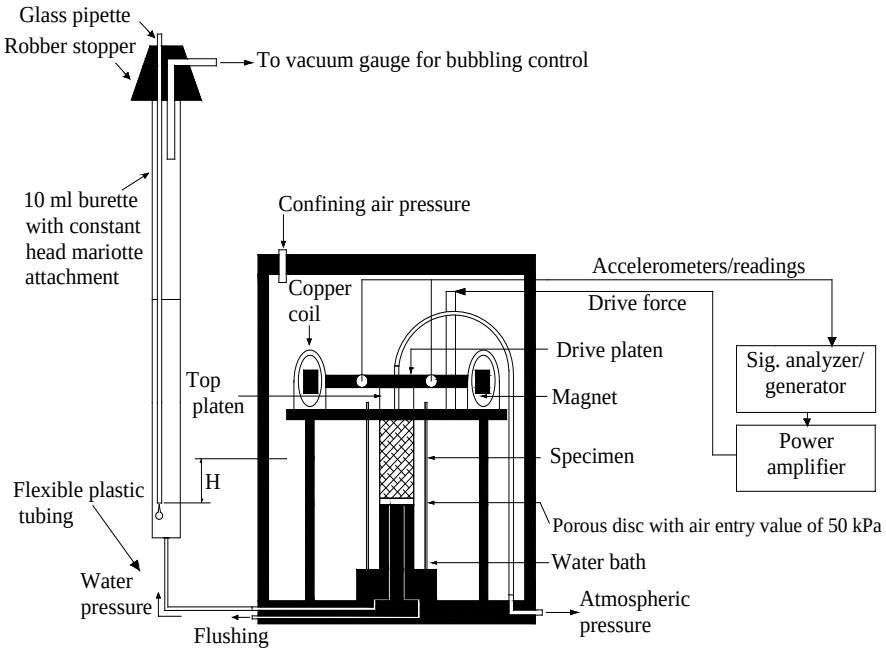

Figure 3-4. Cross-section of the suction-controlled resonant column apparatus

The resonant column test was performed according to ASTM D4015 to determine the small-strain shear modulus G_{max}. A swept sine signal with constant amplitude was supplied by a DataPhysics Quattro® dynamic signal analyzer to a non-contact electromagnetic drive plate connected to the top of the specimen. The resonant angular frequency of the specimen-drive plate system was measured during application of the swept sine signal using two PCB accelerometers attached to the top platen. The two accelerometers were useful in checking the vertical alignment of the specimen during the test. The average measured resonant frequency was used to calculate the dynamic shear modulus. Because the strain magnitudes imposed in this study were in the linear elastic range (less than 10^{-6}), the same specimen was used to evaluate the impact of different matric suction values on G_{max}. The volume change due to confining pressure change and suction change during the test was assumed to be negligible.

3.3.2 Specimen Preparation

Cylindrical specimens were prepared by aerial pluviation (raining) of sand into the membrane expanded over a split mold. Each specimen had a diameter of 35 mm and a height of 70 mm, and an initial relative density of 50%. The intensity and velocity of raining were controlled by the opening of the funnel from which the sand was poured, and the distance between the funnel and the mold, respectively. Three specimens were prepared to evaluate the behavior under three values of net normal stress ($\sigma - u_a$). A total of nine testing conditions including three matric suction values and three net normal stresses were considered for the testing program, as summarized in Table 3-2.

Table 3-2. Matrix of stress conditions applied to the sand specimens

Net Stress (kPa)	**3.5**	**12**	**20**
Matric Suction (kPa)	0.0 (Saturated)	0.0	0.0
	1.5	1.5	1.5
	3.0	3.0	3.0

3.3.3 Effect of Matric Suction on G_{max} of Partially-Saturated Sand

The SWRCs obtained from the resonant column tests on the three sand specimens evaluated under different net normal stresses are shown in Figure 3-5. It was found that the SWRCs are relatively the same, with negligible changes in porosity with net stress. A shift in the water retention curve of approximately 1 kPa was noted when the confining pressure was increased from 3.5 kPa to 20 kPa. The small-strain shear modulus values of the sand obtained from the resonant column tests are presented in Figures 3-6 and 3-7. Similar to Qian et al. (1991), an increase in G_{max} was noted as the specimen dried from initially saturated conditions. After reaching a matric suction of 4.5 (for tests under σ_c = 3.5 kPa) or 6 kPa (for tests under σ_c = 12 kPa and 20 kPa), a decrease in G_{max} was noted. The degree of saturation for these values of suction corresponds approximately to residual conditions.

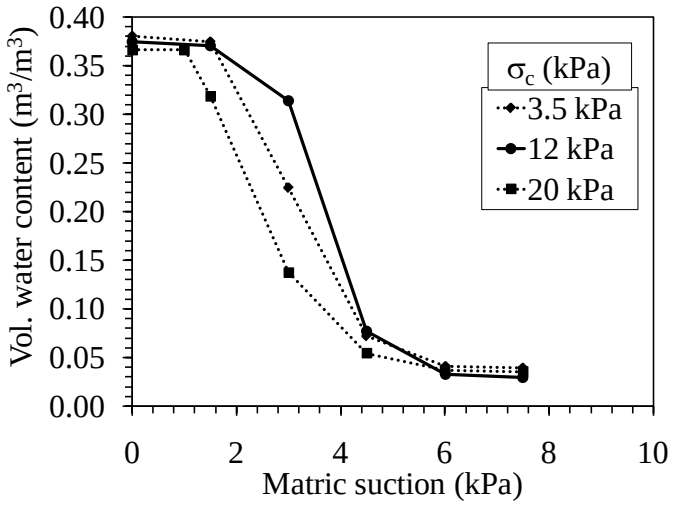

Figure 3-5. Points on the SWRC at which G_{max} measurements were made

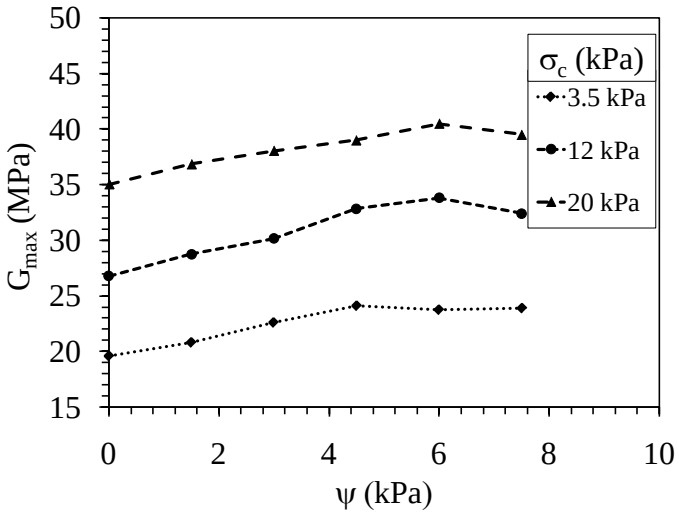

Figure 3-6. Measured G_{max} values as a function of matric suction

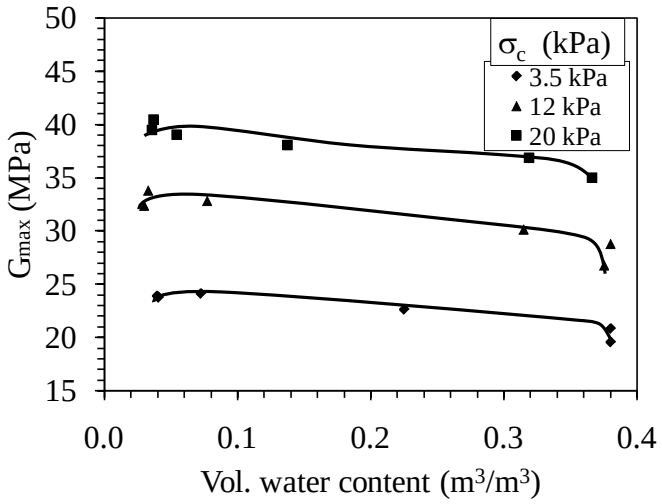

Figure 3-7. Measured G_{max} values as a function of vol. water content

Schubert (1975) categorized the effect of matric suction on the small-strain shear modulus of sand into three zones: a saturation zone ranging from zero suction up to the air entry suction; a transition zone ranging from the air entry suction to the residual suction; and a residual zone ranging from the residual suction and higher. In the saturation zone, the capillary force is almost negligible and a gradual increase of small-strain shear modulus is observed. In the transition zone the capillary force increases to a maximum value at a low degree of saturation. In this zone, a rapid rate of increase in small-strain shear modulus is observed. In the residual zone the capillary force rapidly decreases toward zero and the small-strain shear modulus decreases with increasing matric suction. This optimum value was found to be close to the water content of the sand at residual conditions.

CHAPTER IV

EMPIRICAL METHODOLOGY TO ESTIMATE SEISMICALLY INDUCED SETTLEMENT OF PARTIALLY-SATURATED SAND

4.1 Objectives

Prediction of the seismically induced settlement of a sand layer is a major challenge in geotechnical design. Seed and Silver (1972), Tokimatsu and Seed (1987), Pradel (1999), Lee and Albaisa (1974) have all developed prediction methods for sand layers in dry or saturated conditions. Although these studies provide valuable information about the logic behind seismically induced settlement in soils in general, validated methods are still needed for the prediction of the seismically induced settlement of partially saturated sand layers.

In this chapter, a new methodology is described for prediction of the settlement response of partially-saturated sand layers to seismic loading. This methodology will be used to predict the settlement and other key parameters including effective stress, shear modulus, induced shear stress and shear strain, and excess pore water pressure. Because one of the goals of this study is to validate this methodology by comparing it against the centrifuge modeling results, the input parameters used to demonstrate the behavior of the methodology are those for F-75 silica sand. However, an issue with the methodology developed in this study is that key input parameters are difficult to define. Accordingly, assumptions were made about some of the input parameters based on experimental observations in the literature. The methodology was implemented in MATLAB, and a summary of the program is presented in Appendix A.

4.2 Methodology for Seismic Settlement Prediction

The material parameters of a sand layer vary with depth due to variations in effective stress. Although the settlement process during earthquake shaking involves coupling between changes in effective stress and displacement, fully-coupled analyses are complex and difficult to validate (Arulanandan et al. 1983). Accordingly, an equivalent linear approach is used to estimate the settlement of a sand layer due to earthquake shaking. To do this, the sand layer is divided into n sub-layers (shown in Figure 4-1). It is assumed that the material properties are constant over each sub-layer. The total settlement can be calculated by summing the partial settlements of each sub-layer, as follows:

$$\Delta H = \sum_{i=1}^{n} dh_i = \sum_{i=1}^{n} \varepsilon_{v_i} h_i \tag{4-1}$$

where ΔH is the total settlement, and dh is the partial settlement in each sub-layer. According to aforementioned assumption of constant parameters in each layer, the settlement of each layer is of the product of the vertical strain and the height of each layer. The vertical strain data is usually obtained from simple shear tests where the vertical strain is equal to the volumetric strain (i.e., constant area). Consequently, the change in height may be estimated from the volumetric strain, as follows:

$$dh = \varepsilon_v h \tag{4-2}$$

where ε_v is the volumetric strain. The particular value of ε_v for a given soil layer depends on the stress- and strain-dependent dynamic material parameters at the depth of the soil layer, as well as the characteristics of the seismic load at the depth of the soil layer.

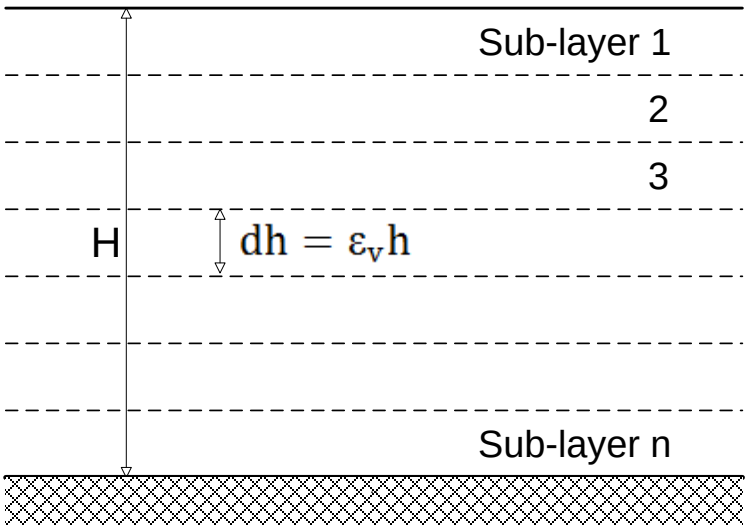

Figure 4-1. Division of the sand layer into n sub-layers

The volumetric strain of partially-saturated sands arises primarily from two sources: (1) compression of voids, and (2) consolidation associated with dissipation of excess pore water pressure. During seismic loading of dry soils, the soil particles will tend to re-arrange and form a denser structure. Because of this re-arrangement, the void space available in the specimen may tend to collapse if the soil is initially loose. The presence of air voids in partially saturated soils indicates that void collapse may also occur in these soils. However, different from dry sands, collapse of voids in partially-saturated soils may be resisted by inter-particle contact stresses, which depend on the matric suction and degree of saturation.

During seismic loading of water-saturated soils, the tendency for particle rearrangement will lead to generation of excess pore water pressure. Different from dry sands, settlement in saturated soils is expected after the shaking stops when the excess pore pressures are allowed to dissipate. In fact, all settlement should happen after the seismic load in the case of undrained situations because of the zero volume change condition. Different from saturated soils, partially saturated soils do not behave in undrained or constant water content conditions. Settlements due to dissipation of excess pore water pressures in partially-saturated soils will occur during loading as well. Further, the tendency for generation of excess pore water pressures will cause an

increase in the degree of saturation, which will lead to a reduction in effective stress and less resistance to particle rearrangement.

The contributions of each source of seismically induced settlement are calculated separately in this methodology and then added back together (which assumes the validity of superposition), as follows:

(4-3) $$\varepsilon_v = \varepsilon_{v-compression} + \varepsilon_{v-consolidation}$$

The volumetric strain associated with compression of the voids requires an estimate of the initial value of effective stress which contributes to the strength of the soil. The total density of the soil is needed to calculate the initial effective stress. The total density can be calculated at the center of the sub-layer, as follows:

(4-4) $$\rho = \rho_d(1+\omega) = \rho_d(1+\frac{S_r e}{G_s})$$

where ρ is the total density, ρ_d is the dry density, ω is the gravimetric water content, S_r is the degree of saturation, e is the void ratio, and G_s is the specific gravity. Using this value, the total stress at a depth z in the soil layer can be calculated as follows:

(4-5) $$\sigma = \rho g z$$

where z is the depth to the center of the soil sub-layer. Effective stress is a key parameter to define dynamic parameters that contribute to the soil response. The effective stress can be calculated using a single stress state approach that correlates suction and effective stress and can be expressed as follows (Lu et al. 2010):

(4-6) $$\sigma' = (\sigma - u_a) + \frac{u_a - u_w}{(1+[\alpha_{vG}(u_a-u_w)]^{N_{vG}})^{(N_{vG}-1)/N_{vG}}}$$

where α_{vG} and N_{vG} in Equation 4-6 are the van Genuchten (1980) SWRC fitting parameters. This equation was selected as it permits the use of equations developed for saturated and dry soils to be used for partially-saturated soils.

After calculating the effective stress at the center of the sub-layer, the small strain (maximum) shear modulus may be estimated at the center of each sub-layer. There are many

formulas available for this purpose including the one proposed by Hardin and Richart (1963), Seed and Idriss (1970), Hardin and Drnevich (1972). All these equation were proposed for sand and they have a general form as shown in Equation 4-7.

(4-7) $$G_{max} = AF(e)(\sigma_m^{'})^{0.5}$$

The shear modulus of soils depends on the strain level induced inside the sand layer. Consequently, the shear modulus of a soil at a specific depth should be updated based on the shear strain induced by an earthquake or cyclic load. In order to estimate the shear strain, the induced shear stress is first estimated using the induced acceleration at the surface of the soil and the depth of the center of the soil sub-layer as proposed by Seed and Idriss (1971) and expressed in Equation 4-8.

(4-8) $$\tau_{ave} = C\ \frac{a_{max}}{g}\sigma_0 r_d$$

where C is a coefficient that depends on the loading condition. In the case of cyclic load the average and maximum induced shear stresses are the same [$\tau_{ave} = (a_{ave}/g)\sigma_o r_d$] and can be measured at the surface of the sand layer. In this case C is equal to 1 while in the case of earthquake load it is equal to 0.65. r_d in Equation 4-8 is a function of depth. The maximum shear modulus G_{max} and the average induced shear stress can be used to estimate a consistent shear modulus and shear strain through an iteration process using Equation 4-9 (shear modulus reduction function) and stress-strain relation ($\tau_{ave} = G\gamma$).

(4-9) $$\frac{G}{G_{max}} = \frac{1}{1 + \left(\frac{\gamma}{\gamma_r}\right)^a}$$

The “a” value in Equation 4-9 can be obtained using Equation 2-13 proposed by Menq (2003) or assumed to be 1 as proposed by Iwasaki et al. (1978), while γ_r value can be calculated using Equation 2-12 proposed by Menq (2003). On the other hand, the induced shear strain can also be directly estimated using Equations 2-14 and 2-16 proposed by Stewart and Whang (2003). Once the induced shear strain is defined at the center of each sub-layer, it can be used to estimate the volumetric strain, which is needed to calculate the seismically induced

settlement. According to Tokimatsu and Seed (1987), Pradel (1998), and Stewart and Whang (2003), volumetric strain depends on induced shear strain, relative density, Number of loading cycles. The seismically induced volumetric strain can be obtained by synthesizing the data from the literature. Because the available information to develop the volumetric strain is from cyclic simple shear tests on dry sands, it should only be used for dry sand. Consequently, a term should be incorporated into this equation to consider the effect of the degree of saturation and suction. The partially-saturated sand has smaller void air spaces than dry sand because of the presence of water in the void space. On the other hand, inter-particle contact forces can resist against compression. Considering all the parameters affecting the seismically induced volumetric strain of sand, volumetric strain would be calculated using a single equation in Equation 4-10.

$$\varepsilon_{v-compression} = f(\gamma, N, D_r, S_r) \quad \text{(7-10)}$$

where γ is the shear strain, D_r is the relative density, N is the number of cycles, and S_r is the degree of saturation.

In order to calculate the volumetric strain due to consolidation associated with the dissipation of excess pore water pressure the amount of accumulated pore pressure due to seismic load should be calculated. Lee and Albaisa (1974) expressed that the consolidation volume change only depends on the excess pore pressure build up and it is independent of type of cyclic loading. According to Tokimatsu and Seed (1987), the excess pore water pressure in saturated sand is associated with the shear stress and shear strain induced by seismic loads. In their approach, the first step was to define the term Cyclic Stress Ratio (CSR) at the center of each sub-layer, as follows:

$$CSR = \frac{\tau_{ave}}{\sigma'} \quad \text{(7-11)}$$

where τ_{ave} is the average induced shear stress and σ' is the initial effective stress.

The excess pore water pressure generated in a saturated sand layer depends on the number of cycles induced during loading and the magnitude of the CSR. In the case of earthquake load the equivalent number of cycles is related to the magnitude of the

earthquake using Equation 2-19 (Tokimatsu and Seed, 1987). The generated excess pore water pressure is expressed usually as a r_u function, where r_u is equal to the ratio of the change in pore water pressure (Δu) to the initial effective stress at the depth of interest. r_u depends on CSR, N (number of cycles), e (void ratio), and S_r (degree of saturation), as follows:

(4-12) $$r_u = f(CSR, N, e, S_r)$$

Lee and Albaisa (1974), Wu and Seed (2004), and Cetin et al. (2009) presented an extensive database on volumetric strains induced in saturated sands due to consolidation associated with dissipation of excess pore water pressure. They presented different data sets showing the variation of consolidation volumetric strain due to change in the relative density, the total confining stress, and pore pressure ratio. The general form of the equation to calculate the volumetric strain due to consolidation is shown in Equation 4-13.

(4-13) $$\varepsilon_{v-consolidation} = f(r_u, D_r, \sigma)$$

where r_u is the pore pressure ratio, D_r is the relative density, and σ is the total confining stress. A schematic flow chart describing the empirical methodology is shown in Figure 4-2.

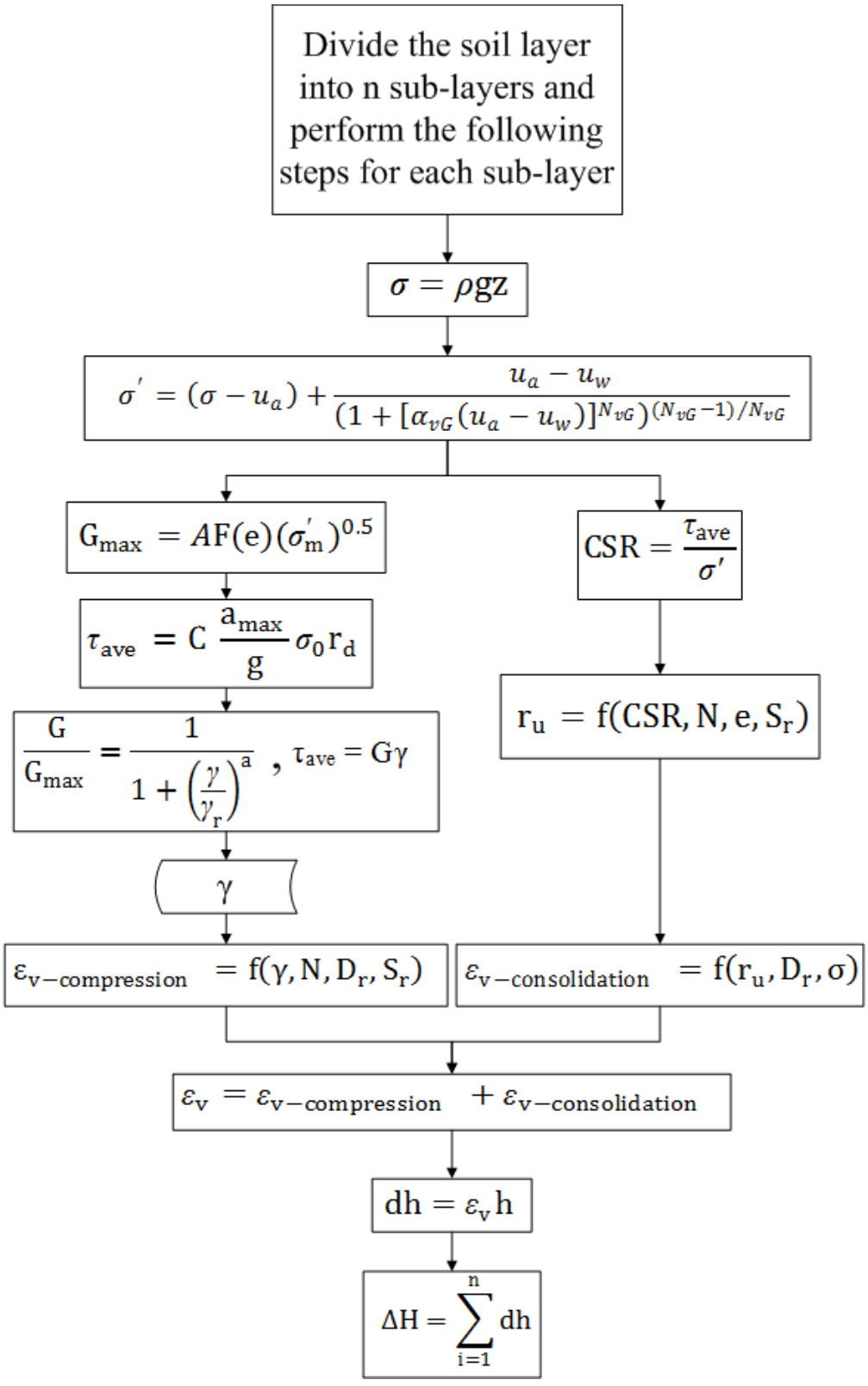

Figure 4-2. Schematic flow chart of the empirical methodology

4.3 Evaluation of Seismic Compression Using the Empirical Methodology

In last section a frame work was established to estimate the seismically induced settlement of partially-saturated sand layer. As discussed earlier, there are material parameters and empirical equations in this methodology that are not clearly defined. Different researchers studied some of these parameters and equations separately. In this section, material parameters were obtained from the literature; empirical equations were obtained by synthesizing the data sets available in the literature; and some assumptions were made for the parameters and equations based on the observed trend which are not perfect. However, it should be noted that the data sets obtained from the literature are not for the same material. Consequently the same magnitudes of settlement cannot be expected because the input parameters used in the methodology are not specific to Ottawa sand. The initial input parameters, used in this section in order to study the methodology, are listed in Table 4-1. Although the methodology is developed for both earthquake and cyclic loads, cyclic load was considered in this research to study the seismically induced settlement of partially-saturated sand.

Table 4-1. Empirical approach initial input data

Parameter	**Value**
Model depth	15.875 cm
Height of the bottom of the sample from centrifuge platform	27.94 cm
Centrifuge arm length	5.486 m
g-level at the center of the specimen	40g
Number of sub-layers	50
Sand	Ottawa Sand
G_s	2.65
Φ	35°
υ	0.25
$\rho_{d\text{-}max}$, $\rho_{d\text{-}min}$	1781, 1469 kg/m^3
e_{max},e_{min}	0.8039, 0.4879
D_r	0.45
C_u	1.71
ρ_w	1000 kg/m^3
PSA (prototype)	0.65g
N	15
Frequency (prototype)	1 Hz

The sand layer was assumed to have uniform degrees of saturation ranging from 0.00 to 1.00 in increments of 0.01. Although suction profile through the depth of the soil layer could be more complicated, a uniform suction profile was selected. Uniform suction profile is a simple form that can be easily interpreted. In addition, it is possible to study the effect of the degree of saturation on seismic compression of sand layers with different uniform suction profiles. On the other hand, this system is more convenient in centrifuge physical modeling. The van Genuchten (1980) SWRC parameters for F-75 Ottawa sand are listed in Table 4-2. The SWRC plot is shown in Figure 4-3. A set of empirical equation was selected to be used in the methodology as presented in Table 4-3.

Table 4-2. SWRC parameters for the van Genuchten (1980) model

Parameter	**Value**
θ_r (residual water content)	0.04
θ_s (saturated water content)	0.397
α_v	0.24
N_v	7

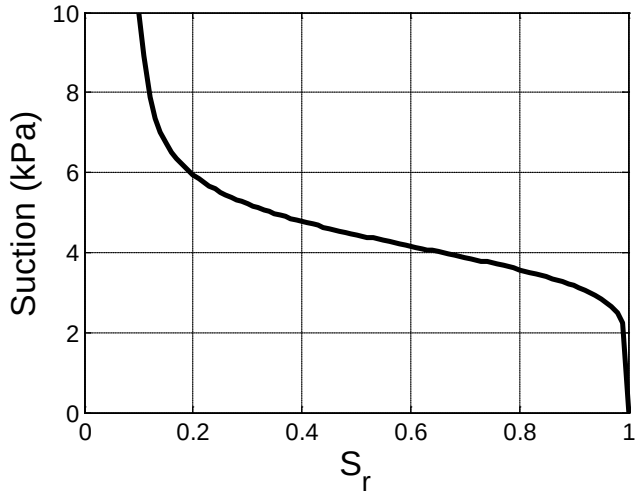

Figure 4-3. Estimated SWRC for F-75 Ottawa sand

Table 4-3. A set of empirical equations that can be used in the propsed methdology

General Form	Example Empirical Equation	Units	References
$G_{max} = AF(e)(\sigma_m^{'})^{0.5}$	$G_{max} = 700\frac{(2.17-e)^2}{1+e}(\sigma_m^{'})^{0.5}$	Kg/cm^2	Hardin and Richart (1963)
$G_{max} = AF(e)(\sigma_m^{'})^{0.5}$	$G_{max} = 9200(\sigma_m^{'})^{0.5}$	kPa	Chapter 5 (BE Test)
$\tau_{ave} = C\ \frac{a_{max}}{g}\sigma_0 r_d$	*C=1 : Cyclic Load* *C=0.65 : Earthquake*	---	Seed and Idriss (1971)
	$r_d = \frac{1}{1+\left(\frac{d_c}{30.5m}\right)^2}$, d_c: depth		Pradel (1998)
$\frac{G}{G_{max}} = \frac{1}{1+\left(\frac{\gamma}{\gamma_r}\right)^a}$	$a = 0.86 + 0.1\ log\left(\frac{\sigma^{'}}{p_0}\right)$	---	Menq (2003)
	$a = 1$	---	Hardin and Drnevic (1972)
	$\gamma_r(\%) = 0.12C_u^{-0.6}\left(\frac{\sigma^{'}}{p_0}\right)^{0.5C_u{}^{-0.15}}$	---	Menq (2003)
$\varepsilon_{v-compression}$ $= f(\gamma, N, D_r, S_r)$	$\varepsilon_{v-compression}$ $= \gamma\left(\frac{\left(\frac{D_r}{0.15}\right)^2}{20}\right)^{-1.2}\left(\frac{N}{15}\right)^{0.45}(1-S_r)$	---	Pradel (1998); Tokimatsu and Seed (1987); Assuming a linear reduction factor for S_r
$r_u = f(CSR, N, e, S_r)$	$r_{u-sat} = {}^1/_2 + {}^1/_\pi\ sin^{-1}\left(2\left(\frac{N}{N_{L-sat}}\right)^{1/\alpha} - 1\right)$ *α=0.7*	---	Kramer (1996)
	N_L=f(e,CSR)	---	From Seed and Lee (1965)
	$r_u = r_{u-sat}S_r^{3.5}$	---	Based onYoshimi et al. (1989)
$\varepsilon_{v-consolidation}$ $= f(r_u, D_r, \sigma)$	$\varepsilon_{v-consolidation} = \varepsilon_{v-liquefied}(r_u)^{2.25}$	---	Lee and Albaisa (1974)
	$\varepsilon_{v-liquefied} = 0.12 * \left(\frac{1}{\left(\frac{D_r}{0.15}\right)^2}\right)^{0.75}$	---	From Tokimatsu and Seed (1974) for large CSR
	$\varepsilon_{v-liquefied} = 0.2 * \left(\frac{1}{\left(\frac{D_r}{0.15}\right)^2}\right)^{0.6}$	---	From Wu and Seed (2004) for large CSR

The empirical equations presented in Table 4-3 are obtained by synthesizing data from different sources. However, following considerations were made during the equation development process.

To calculate the volumetric strain due to compression of voids, Pradel (1998) correlated the volumetric strain with the induced shear strain and SPT-N value for 15 cycles of loading based on the plots presented by Tokimatsu and Seed (1987) as expressed in Equation (2-18). Pradel (1998) also proposed Equation 2-19 to account for different number of cycles. In addition, Tokimatsu and Seed (1987) showed the relation between the relative density and SPT-N value as in Figure 2-6. A curve was fitted to Figure 2-6 and the corresponding equation inserted in the volumetric strain equation proposed by Pradel (1998). Although a complete and actual relation can be obtained by performing a set of suction-controlled simple shear tests, it is assumed that the volumetric strain is decreasing linearly by increasing the degree of saturation. Consequently, a linear reduction factor is added to the volumetric strain equation. Combining the volumetric strain equation for dry sand (Equation 2-18) and the equation incorporate the effect of number of cycles (Equation 2-19), inserting the equivalent relative density instead of SPT-N value, and considering a linear reduction factor for changes in the degree of saturation, following equation was proposed for volumetric strain of partially-saturated soils due to compression of void space.

(4-14) $$\varepsilon_{v-compression} = \gamma \left(\frac{\left(\frac{D_r}{0.15}\right)^2}{20} \right)^{-1.2} \left(\frac{N}{15}\right)^{0.45} (1 - S_r)$$

As explained in previous section, the volumetric strain due to consolidation associated with the dissipation of excess pore water pressure mainly depends on the amount of excess pore pressure generated. Kramer (1996) developed an equation to estimate the value of r_u for cyclic loading of saturated soils, as follows:

(4-15) $$r_{u-sat} = {}^1/_2 + {}^1/_\pi \, sin^{-1}\left(2\left(\frac{N}{N_{L-sat}}\right)^{{}^1/_\alpha} - 1\right)$$

where $N_{L\text{-}sat}$ is the number of cycles to reach liquefaction in saturated sand which depends

on the CSR value, α is a constant equal to 0.7, and N is the actual number of cycles applied to the sand layer. The data in Figure 4-4 from Seed and Lee (1975) provides an approach to relate CSR and the number of cycles to reach liquefaction for soils having different void ratios. The data in Figure 4-4 was used to develop a functional relationship between CSR and the number of cycles to reach liquefaction, as follows:

(4-16) $$CSR = aN_{L-sat}^2 + bN_{L-sat} + c$$

where $$a = -0.00732e + 0.00920$$

$$b = 0.17007e + 0.19286$$

$$c = -1.44463e + 1.55401$$

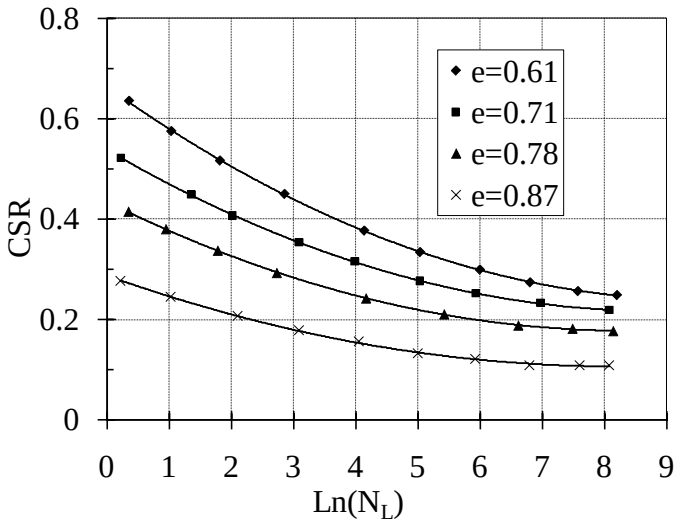

Figure 4-4. CSR function for saturated sand (Seed and Lee, 1965)

The value of $N_{L\text{-}sat}$ can be obtained by solving Equation 4-16 for any given CSR. After calculating the values of $N_{L\text{-}sat}$ for each sub-layer and knowing N value for the specific loading condition, the r_u value can be calculated using Equation 4-15 for saturated sand. The r_u value in unsaturated specimen is different than saturated specimen. It is assumed that the ratio of $r_u/r_{u\text{-}sat}$ is always less than one and decreasing by decreasing the degree of saturation. Because accumulation of excess pore pressure leads to liquefaction, it is assumed that $r_u/r_{u\text{-}sat}$ is

proportional to liquefaction resistance ratio. Yoshimi et al. (1989) evaluated the liquefaction resistance of partially-saturated sands, by plotting the liquefaction resistance ratio against the degree of saturation (shown in Figure 2-18). Because liquefaction happens due to generation of excess pore water pressure, the liquefaction resistance ratio was used for the ratio between the values of r_u for partially-saturated and saturated sands under the same loading conditions, resulting in the following equation for r_u for partially-saturated soils:

(4-17) $$r_u = r_{u-sat} S_r^{3.5}$$

Lee and Albaisa (1974), and Wu and Seed (2004) presented an extensive database on volumetric strains induced in saturated sands due to consolidation associated with dissipation of excess pore water pressure after liquefaction, as shown in Figure 4-6. In these two plots the post-liquefaction volumetric strain is correlated to the SPT-N value and CSR value. According to these plots the volumetric strain approaches a uniform value for a very high CSR at any given SPT-N value especially for low SPT-N values (loose sands). A maximum surface acceleration of 0.65g which was selected for this study produces very high CSRs through the depth of the specimen. For the case of D_r=0.45 which is a loose sand specimen the assumption of uniform post-liquefaction volumetric strain can be applied. Consequently, by synthesizing the data shown in Figure 4-5 (a) and (b) and inserting the equivalent relative density instead of SPT-N value, following equations can be obtained respectively.

(4-18) $$\varepsilon_{v-liquefied} = 0.12 * \left(\frac{1}{\left(\frac{D_r}{0.15}\right)^2} \right)^{0.75}$$

(4-19) $$\varepsilon_{v-liquefied} = 0.2 * \left(\frac{1}{\left(\frac{D_r}{0.15}\right)^2} \right)^{0.6}$$

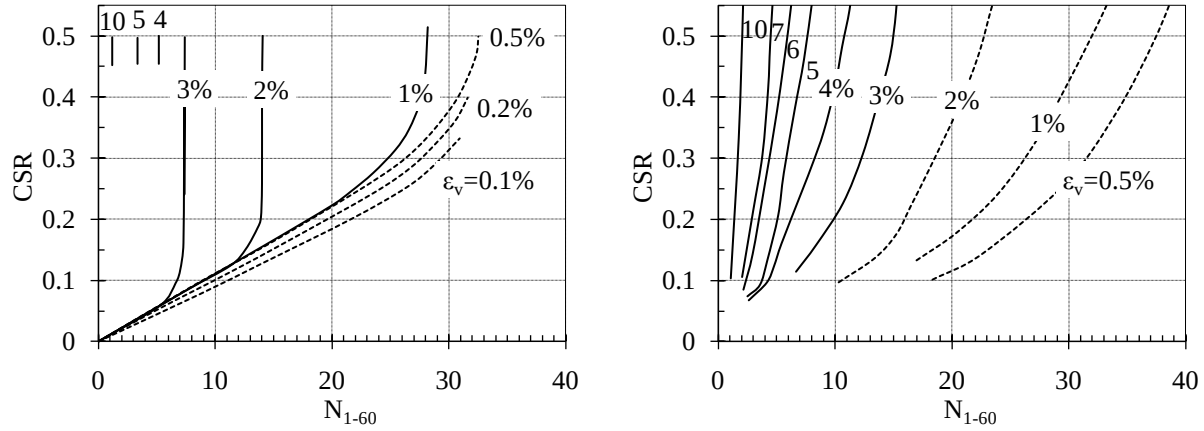

Figure 4-5. Post-liquefaction volumetric strain of saturated clean sand [(a) Tokimatsu and Seed (1987); (b) Wu and Seed (2004)]

Lee and Albaisa (1974) showed that incomplete liquefaction can also cause volumetric strain. They measured the change in volumetric strain due to the change in r_u value for different relative densities and confining pressures as shown in Figure 2-10 (a) and (b). The volumetric strains measured by Lee and Albaisa (1974) can be normalized by the volumetric strain in the case of liquefied condition when r_u=1. The normalized data can be approximated using a single equation for all relative densities and confining pressures as follows.

(4-18) $$\varepsilon_{v-consolidation} = \varepsilon_{v-liquefied}(r_u)^{2.25}$$

After inserting the required equations and input parameters in the MATLAB code presented in the appendix, the desired values would be calculated based on the selection of input parameters. In this section the equation by Hardin and Richart (1963) is used for G_{max}, C=1 is applied for cyclic load, the "a" value in the shear modulus reduction function is calculated based on the equation of Hardin and Drnevich (1972), and the volumetric strain of liquefied sand is obtained using the equation based on the data of Tokimatsu and seed (1987).

Suction stress values were calculated using Equation 2-25 for F-75 Ottawa sand. As suction stress depends on the SWRC, it is constant with depth for each degree of saturation. Consequently, it has more significant effect on the effective stress in shallower depths. The

effective stress variation through the depth of sand layers having different degrees of saturation is shown in Figure 4-6.

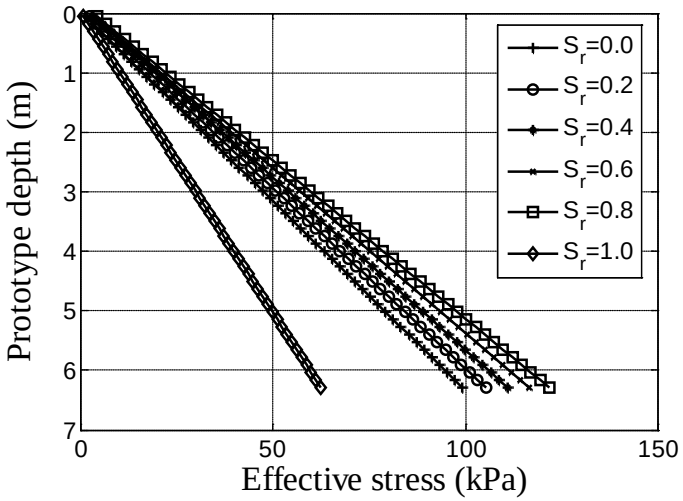

Figure 4-6. Variation in effective stress with depth in the sand layer

The maximum shear modulus variation due to changes in the effective stress was calculated using Equation 4-6. The variation of the small-strain shear modulus with depth is shown in Figure 4-7. The maximum shear moduli in this figure are calculated using the equation proposed by Hardin and Richart (1963).

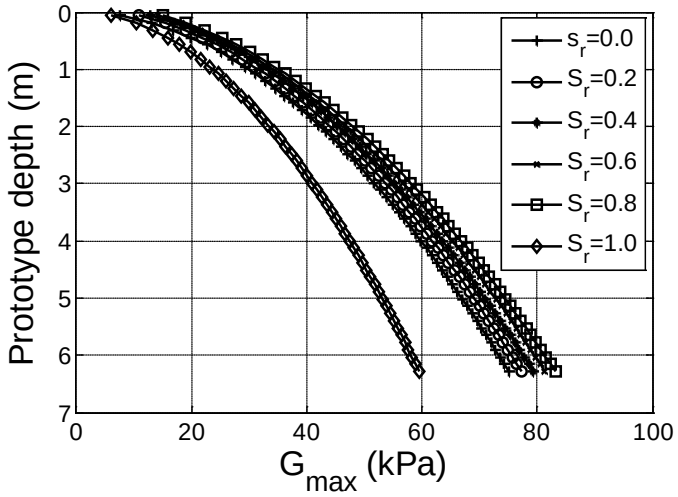

Figure 4-7. The maximum shear modulus variation through the depth of the sand layer

The average induced shear stress is obtained using Equation 2-14 where Pradel's (1999)

r_d values were inserted in that equation. The calculated average shear stress and maximum shear modulus were used to obtain the consistent induced shear strain and shear modulus in the sand. The a and γ_r values used in iteration method were obtained using the equations proposed by Menq (2003) and presented in Equations 2-12 and 2-13. The calculated shear strain and the reference shear strain using the approach of Menq (2003) are shown in Figure 4-8.

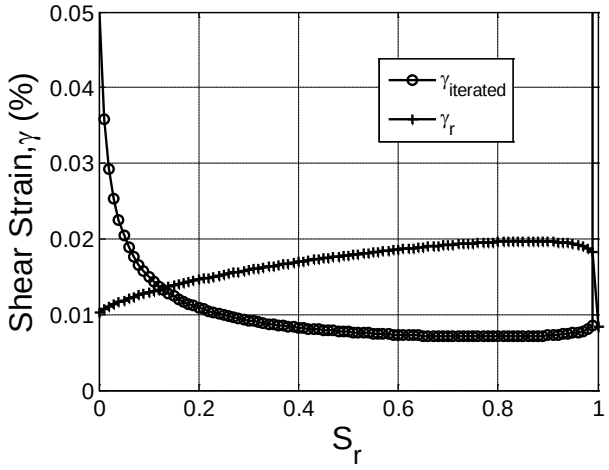

Figure 4-8. Consistent shear strain for the top sand sub-layer

The volumetric strain due to compression of the void space caused by the induced shear strain in the top sub-layer was calculated using Equation 4-14 and is shown in Figure 4-9. The volumetric strain decreases by increasing the degree of saturation.

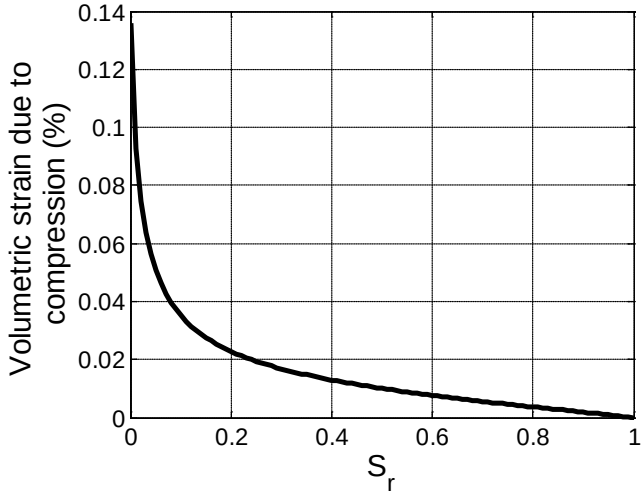

Figure 4-9. Volumetric strain due to compression of void space for the top sub-layer

After calculating the volumetric strain caused by collapse or compression of void space, the volumetric strain caused by consolidation due to excess pore water pressure dissipation should be calculated. The CSR value is calculated based on the induced shear stress and initial effective stress at the center of each sub-layer. The number of cycles causing liquefaction in saturated condition is calculated by solving Equation 4-16. Then, the r_u function was calculated for saturated sand using Equation 4-15 and modified for different degrees of saturation using Equation 4-17. The variation of r_u value for partially-saturated sands due to cyclic loading for the top sub-layer is shown in Figure 4-10. The volumetric strain due to consolidation after dissipation of excess pore water pressure is calculated using Equations 4-18 and 4-20, and shown in Figure 4-11. The volumetric strain decreases by decreasing the degree of saturation while there is very low volumetric strains at the degree of saturation lower than 0.6.

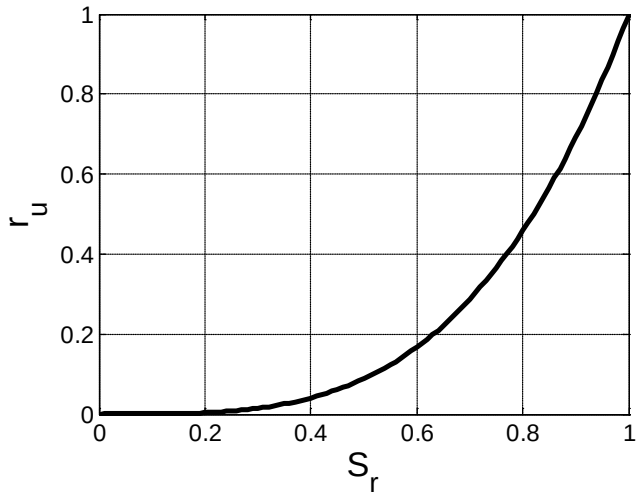

Figure 4-10. r_u function for the top sub-layer

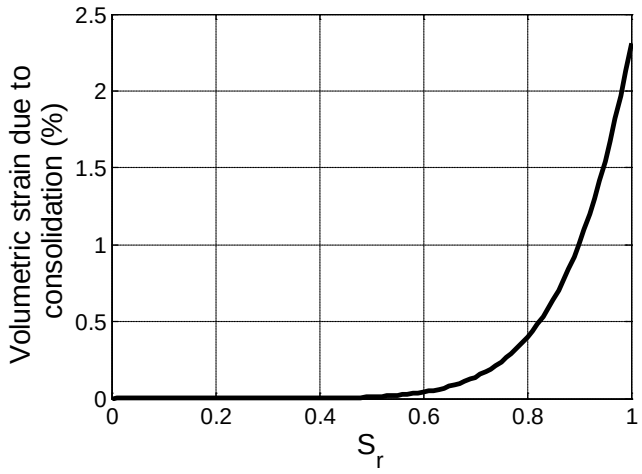

Figure 4-11. Volumetric strain due to consolidation for the top sub-layer

The total volumetric strain at each sub-layer is obtained by adding the volumetric strains calculated from each of the volumetric strain sources shown in Figures 4-9 and 4-11. Then, the total settlement of the sand layer is calculated using summation of differential settlements obtained by multiplication of the volumetric strain and height of each sub-layer. The surface settlement of the sand layer for different degrees of saturation with the characteristics listed in Table 4-1 is shown in Figure 4-12. The settlement observed in Figure 4-12 follows a nonlinear trend with the degree of saturation. A minimum value was obtained at a degree of saturation of 0.7.

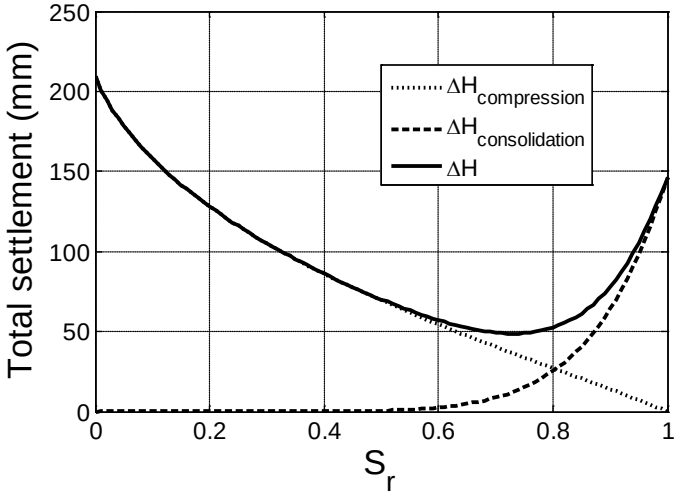

Figure 4-13. Total settlement due to cyclic load using the empirical approach

4.4 Parametric Analysis of the Empirical Methodology

As discussed earlier there are two main uncertainties in the empirical methodology including material parameters and unverified relations adopted from tests on either dry or saturated sand. In order to obtain a better prediction of the seismic settlement, the material parameters and empirical equations used in this methodology should be improved.

One of the improvements is to obtain more accurate material parameters. To demonstrate the importance of input parameters, the sensitivity of predicted settlements was analyzed for two different input parameters including small-strain shear modulus and strain-dependent shear modulus. The settlement of the sand layer was calculated using G_{max} equation proposed by Hardin and Richart (1963) and also the equation proposed later in this study based on bender element test. The seismic settlement variation for different degrees of saturation is shown in Figure 4-13. Although the G_{max} values estimated using these two equations were very close, the settlement values are different. Specifically, the settlement values based on bender element test data has higher values in low degrees of saturation. It shows the effect of G_{max} on seismic settlement due to compression of voids.

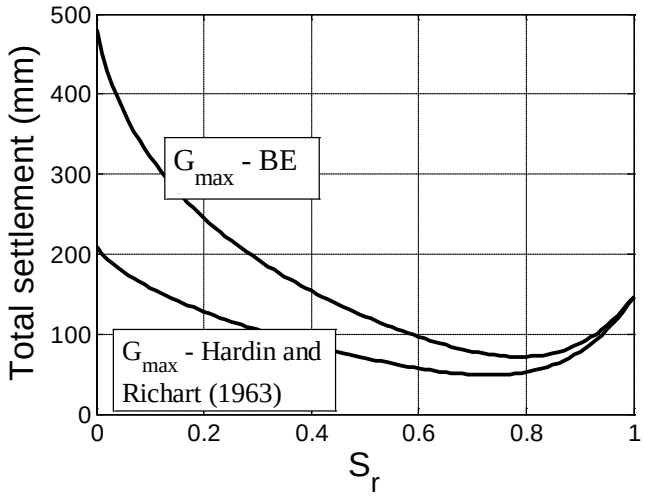

Figure 4-13. Total settlement of the sand layer using two G_{max} equations

On the other hand, the seismic settlement of a layer of partially-saturated sand was

evaluated based on two different definitions of shear modulus reduction function. The “a” value in shear modulus reduction function presented in Equation 4-9 can affect the estimated shear modulus and consequently the predicted seismic settlement. The predicted settlement of the sand layer based on the two “a” values in shear modulus reduction function is presented in Figure 4-14. In this plot, settlement is calculated based on the “a” value in Equation 2-13 proposed by Menq (2003) and “a” value proposed by Hardin and Drnevich (1972). The value of a proposed by Menq (2003) depends on the coefficient of uniformity of the sand as well as the effective stress, and is approximately equal to 0.86. On the other hand, Hardin and Drnevich (1972) estimated the magnitude of “a” to be 1. If the value of “a” increases from about 0.86 to 1, the total magnitude of settlement increases significantly, as shown in Figure 4-14. The G_{max} value in both curves was calculated using the equation by Hardin and Richart (1963). The results shown in Figures 4-13 and 4-14 indicate that the material input parameters have significant effects on the final predicted settlement and need to be further investigated.

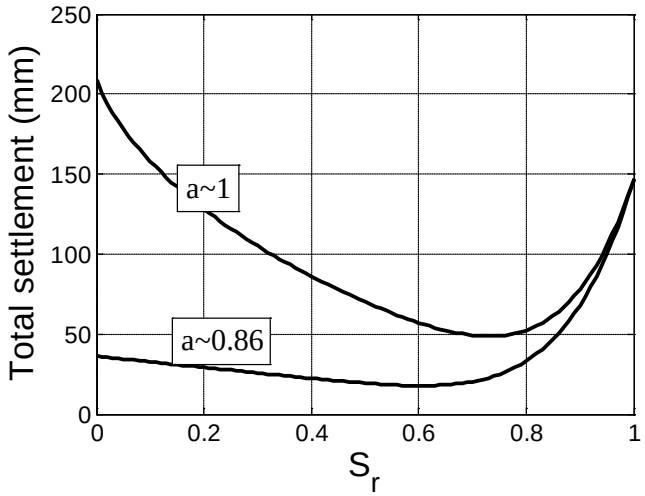

Figure 4-14. Total settlement of the sand layer using two different a values

Another important issue is selection of the relations used in the empirical methodology. One of the important relations is the equation to estimate the post-liquefaction volumetric strain and then calculate the volumetric strain due to consolidation. Two different equations were

adopted from two different data sets presented by Tokimatsu and Seed (1987) and Wu and Seed (2004). The volumetric strain due to consolidation associated with dissipation of excess pore water pressure has a significant effect on the total seismically induced settlement of partially-saturated sand as shown in Figure 4-15. In this Figure G_{max} is based on Hardin and Richart (1963) and "a" value in shear modulus reduction function is about 1.

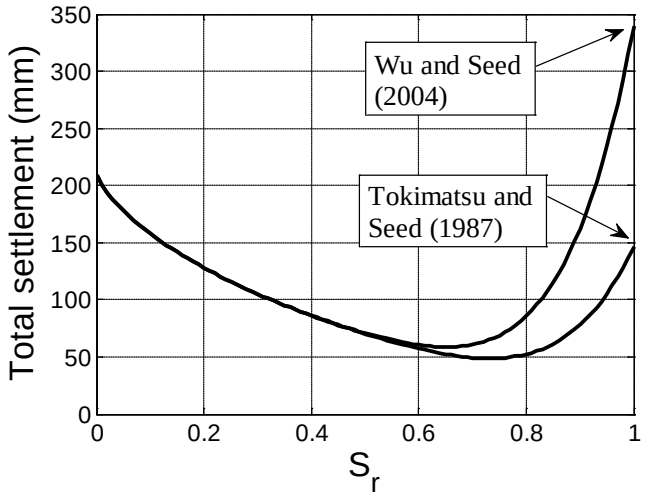

Figure 4-15. Total settlement of the sand layer using two different post-liquefaction settlement equations

r_u value has a major effect on seismic settlement due to consolidation. The pore pressure ratio of partially-saturated sand was estimated by multiplying a reduction factor to the pore pressure ratio of saturated sand. This reduction factor is based on liquefaction resistance data which is only an assumption. The seismic settlement results of partially-saturated sand layer based on two different r_u definitions are shown in Figure 4-16. G_{max} is from Hardin and Richart (1963), "a" value is about 1, and post-liquefaction settlement is from Wu and Seed (2004). The selection of r_u function affects both the settlement value and the degree of saturation of minimum settlement.

According to Figures 4-13 to 4-16, selection of more accurate input parameters and equations are necessary. However, understanding the general trend and settlement mechanisms is useful to better characterize and interpret the seismically induced settlement measurements from

experimental tests. The surface settlement due to the applied cyclic load using different parameter and equation selections are shown in Figure 4-17 where a range of seismically induced settlement can be obtained. A general nonlinear trend with a minimum settlement at a middle range degree of saturation can be observed in this figure.

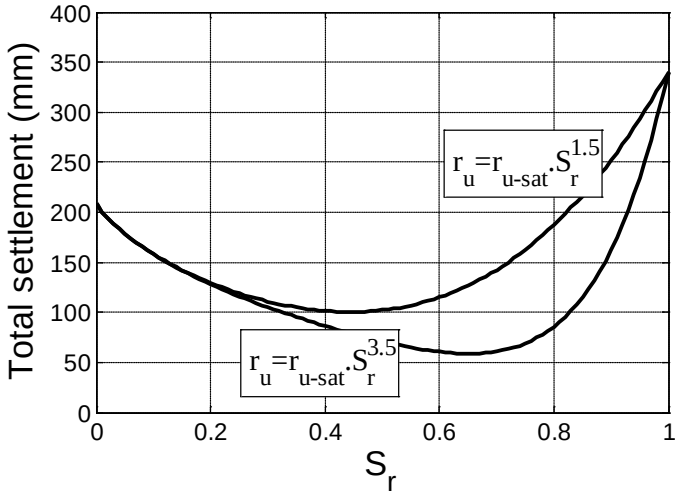

Figure 4-16. Total settlement of the sand layer using two different r_u functions

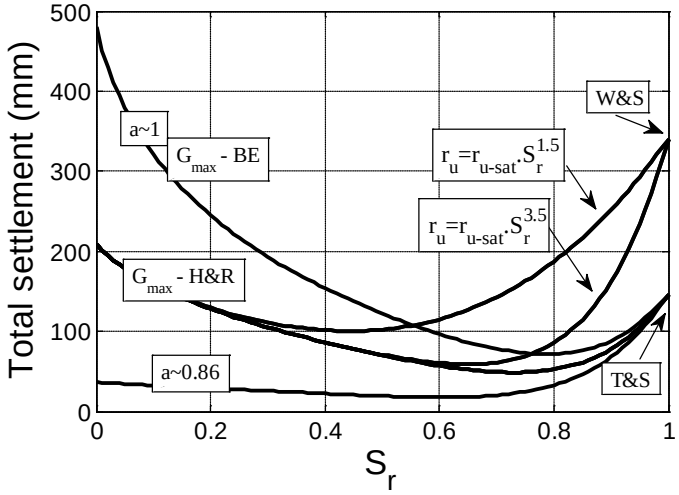

Figure 4-17. A possible range for total settlement of the sand layer

CHAPTER V

CENTRIFUGE PHYSICAL MODELING TEST DEVELOPMENT

5.1 Concept of Partially-Saturated Soil Testing

Although most soils near the ground surface have a complex suction profile due to environmental interaction, for design purposes it is conventional to evaluate the response of soil profiles with a simplified suction profile. One simplified suction profile involves a soil layer having a water table at some depth below the surface, with no infiltration. In this case, the matric suction will increase linearly with height above the water table. However, in the case of sands, the soil layer will be completely dry within a short distance away from the water table due to the shape of the SWRC. Accordingly, this simplified suction profile is not optimal for physical modeling of the impact of partially-saturated conditions on the deformation response of soils during cyclic loading. Another case would be that of steady-state infiltration through a soil layer having a water table at some depth below the surface. In this case, water flow will occur under unit gradient conditions, so the matric suction will tend to be uniform with depth except near the water table (Zornberg and McCartney 2010). The magnitude of suction in the soil profile depends on the rate of infiltration. Because of its simplicity and its association with a real infiltration scenario in the field, a uniform suction profile is most suitable for physical modeling of the impact of partially-saturated conditions on the deformation of soils during cyclic loading. Further, this approach is particularly suitable for use in the centrifuge because the region of the specimen having constant suction during infiltration will increase with the g-level

(Dell'Avanzi et al. 2004).

The use of infiltration to control the suction profile in partially-saturated soil layers has been referred to as the Drainage-Recharge Method (Yegian et al. 2007) or the Steady-State Infiltration Method (McCartney and Zornberg 2010). In this method, different degrees of saturation can be achieved by imposing different infiltration rates on top of the soil layer. After reaching steady-state infiltration, cyclic loading tests can be performed. Another method which has been used to obtain a uniform suction profile in partially-saturated sands is the Electrolysis Method (Yegian et al. 2007). This technique was found to be appropriate for degrees of saturation close to fully saturated conditions, as it takes long time to reach a desired degree of saturation. This technique was not adopted in this study as the centrifugal acceleration may cause migration of pore fluid to the bottom of the soil layer.

Infiltration of water through a partially-saturated soil layer is related to the volumetric water content, θ (or the degree of saturation, S_r), the matric suction,ψ, and the hydraulic conductivity, K. Dell'Avanzi et al. (2004) solved the governing equation for infiltration into partially-saturated soils in a centrifuge, expressed as the profile of suction with height from the bottom of a soil model, z_m, as in Equation 5-1.

$$\psi = -\frac{1}{\alpha_G} ln\left[e^{\left(ln|v_m/N_r K_s + e^{-\alpha_G \psi_{0,m}}| - \alpha_G \rho_w z_m (r_0 - z_m/2)\right)} - \frac{v_m}{N_r K_s}\right] \quad (5\text{-}1)$$

where r_0 is the outside radius of the container in the centrifuge, α_G is obtained from the Gardner (1958) hydraulic conductivity function (HCF) with units of kPa^{-1}, N_r is the g-level (varying with the value of z_m in the model), ρ_w is the density of water (or alternate pore fluid), $\psi_{0,m}$ is the suction at the bottom of the soil layer, K_s is the hydraulic conductivity of saturated soil, and υ_m is the discharge velocity. In this investigation, a freely-draining water table bottom boundary condition was employed (i.e., ψ_m = 0 kPa).

5.2 Centrifuge Facility

For the physical modeling experiments in this investigation, the 400 g-ton centrifuge at

the University of Colorado at Boulder was used (Figure 5-1). This centrifuge consists of an asymmetric rotor arm with a hanging platform at one end, and counterbalance weight on the other. The platform is available to accommodate containers up to 1.21×1.21×0.91 m and weighing up to two tons that can be under centrifugal acceleration of 200g. The radius between from the center of rotation to the platform in the fully extended position is 5.48 m. Two high strength steel tension straps carry the centrifugal loads while an external box-girder structure supports the 33.65 ton weight of the arm. The power supply is from a General Electric 684 kW DC electrical motor connected through shear pins to a horizontal drive shaft, which enters a right angle gear box having a 6.4 to 1 speed reduction ratio. Since during N-g tests, the high velocity of the platform stir the cylindrical air mass inside the chamber, heat is generated. A cooling system containing spiral pipes mounted on the wall of the chamber carries chilled water, minimize the thermal effects. Detailed information on this facility is available in Ko (1988b).

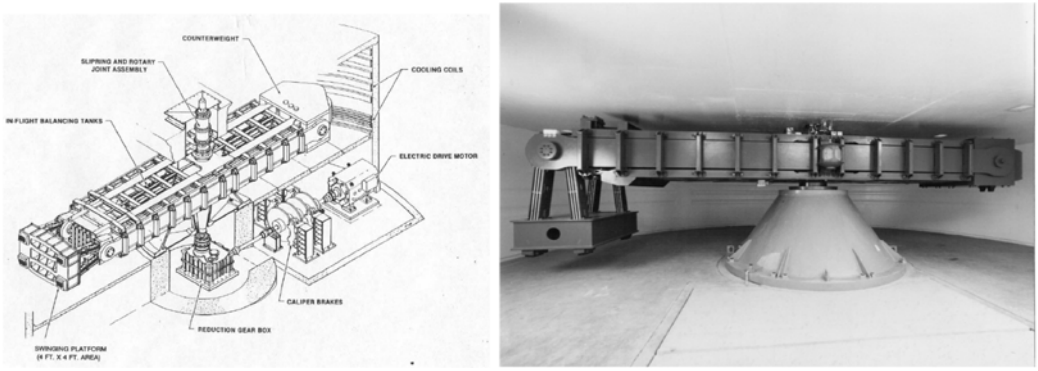

(a) (b)

Figure 5-1. (a) Schematic; (b) Picture of 400 g-ton centrifuge at the University of Colorado at Boulder

5.3 Shake Table Apparatus

The shake table which can be used to impose earthquake or cyclic loads on an overlying soil container used in this study was originally designed by Ketchum (1989). It is an electro-hydraulic system mounted on the centrifuge platform. The system components consist of the servo valve combination including a pilot valve and slave valve manufactured by Team

Corporation, the hydraulic power supply system, the linear actuator, an LVDT, and linear bearings and bearing mounts. The schematic of the shake table assembly is shown in Figure 5-2. A servo controller (Team model) and power amplifier are used to control this servo combination.

The shake table is driven by the linear actuator which is connected to servo valves. To supply the valves with appropriate pressure and flow of oil, an MTS hydraulic power pump and distribution system is used. The linear actuator is located between the two valves and is connected to the shake table. The LVDT is mounted on the centrifuge arm and is attached to the piston rod end of actuator to measure the displacement of the piston relative to the basket. The linear bearings are used to support the shake table on which the experimental package is placed. The shake table system has an estimated 42 kN capacity (Ketchum, 1989).

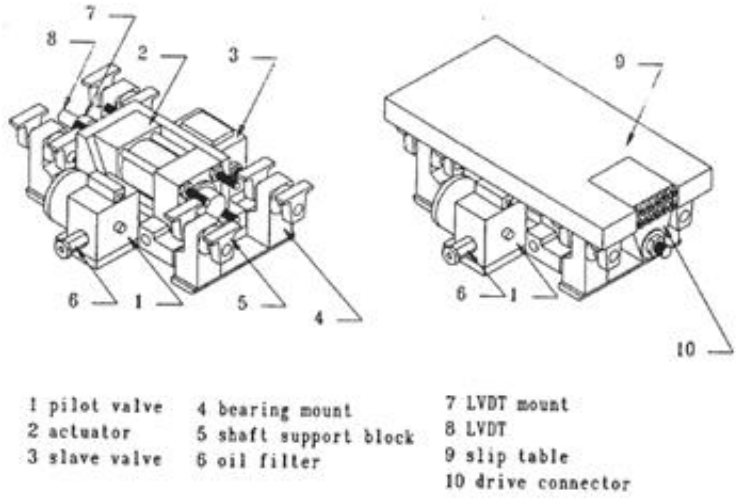

Figure 5-2. The schematic configuration of the shake table

5.4 Laminar Container

Several studies have evaluated the end restraint effects of the specimen container on the movement of shear waves through the soil layer. Options to control the boundary effects on the container on the soil response are a duxseal liner (Weissman 1989), a stacked-ring assembly (Whitman et al. 1981; Lambe and Whitman 1982; Heidari and James 1982; Arulanandan et al. 1983), and a laminar container (Hushmand et al. 1988). The laminar container was found to be

the optimal solution because it simulates shear beam conditions in which shear waves propagate uniformly through the soil specimen while minimizing end effects (Whitman and Lambe 1986). A laminar container developed by Law (1991) with an inside length of 58.42 cm, width of 24.13 cm, and depth of 15.87 cm was used in this study. The container is composed of 14 rectangular aluminum rings, each 1.27 cm thick, and each separated from each other by a 0.5 mm gap between them. Linear bearings between the rings reduce friction during differential movement of rings. The top ring is attached rigidly to vertical supports on the side and ends of the box. The supports on the sides are also equipped with linear bearings to maintain alignment of the rings while the supports on the sides are used to prevent displacements greater than 30 cm which may result in damage of the container and sensors. The schematic view of the laminar container is shown in Figure 5-3.

The laminar container was modified to permit control of flow of pore fluid through the soil layer. In order to drain the water from the bottom of the container, an outflow control plate with the thickness of 1.27 cm was fixed rigidly to the base support of the box. The outflow control plate has a 6.35 mm-thick indentation in its top surface into which a drainage layer could be placed. The drainage layer used in this study is a gravel layer with a uniform particle size of 6.35 mm, overlain by a 10-mil fabric filter. Eight drainage lines in the wall of the outflow control plate were connected to the indentation from the short sides of the plate to drain the water from the bottom of the soil layer. Schematic and Pictures of additional drainage plate and drainage lines are shown in Figure 5-4.

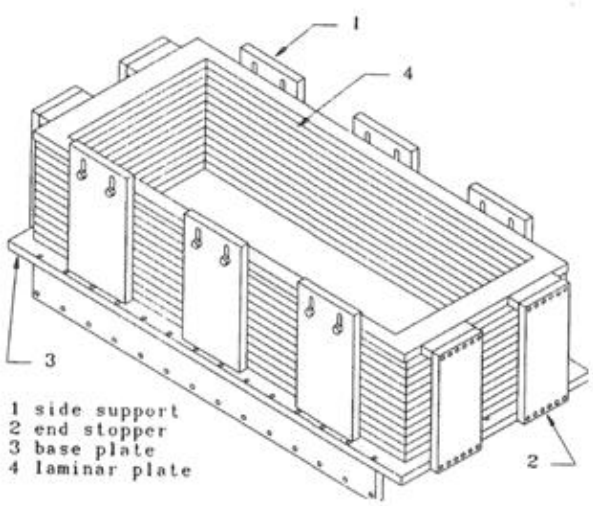

Figure 5-3. The schematic of laminar container by Law (1991)

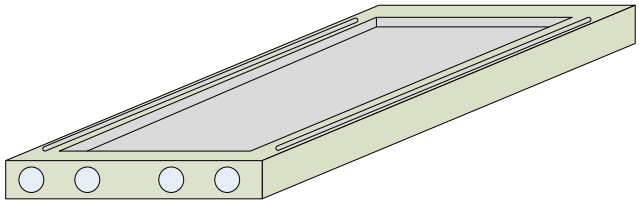

(a)

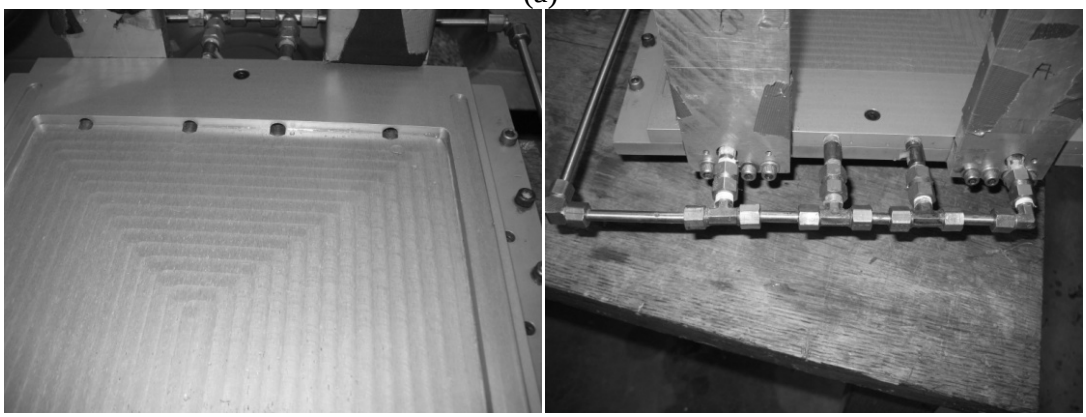

(b) (c)

Figure 5-4. (a) Schematic of the drainage plate; (b) Picture of the drainage plate; (c) Picture of drainage lines connecting to the drainage plate

5.5 Infiltration Setup

In order to apply infiltration to the top of the soil specimen, water was sprayed onto the soil surface using six spray nozzles mounted on two horizontal steel brackets running across the length of the container at a height of 8.15 cm above the soil surface. 3 types of spray nozzles were used to achieve different discharge of water including Bete PJ20, Spraying System Co. 1/8SF-CE and Spraying System Co. 1/4M-8 as they are shown in Figure 5-5. These spray nozzles supply a cone of mist, which is necessary to obtain uniform coverage of flow across the soil layer. The nozzles were arranged on the steel brackets so that the spray covers the whole surface area of the soil. The idealized spray distribution from the nozzles is shown in the plan view of the laminar container in Figure 5-6.

Figure 5-5. Spray nozzles used in this study, left to right: PJ20, 1/8SF-CE, 1/4M-8

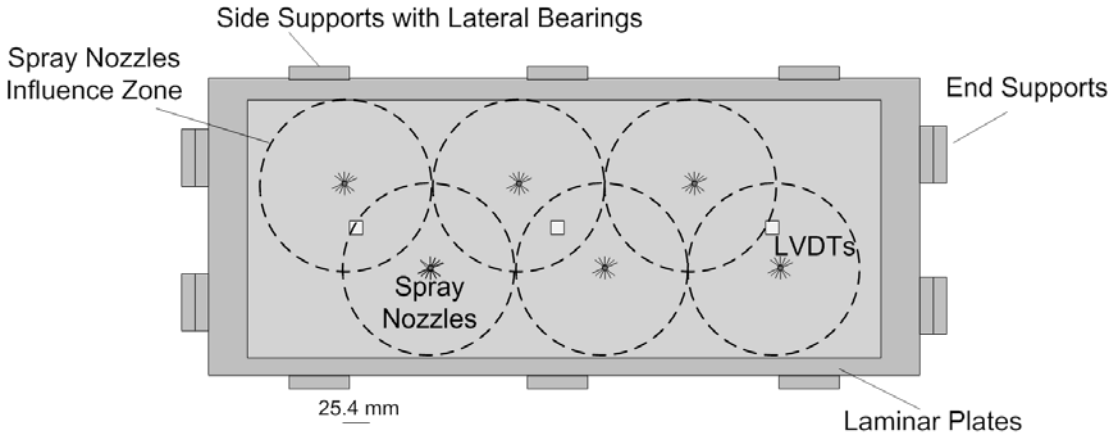

Figure 5-6. Schematic of nozzle arrangement and zone of influence of water spray

The fully-assembled laminar container is mounted atop the shake table on the centrifuge platform. Pictures of the modified laminar container are shown in Figures 5-7(a) and (b). The auxiliary components of the infiltration setup on the centrifuge platform are shown in the schematic in Figure 5-8. This set up is divided to inflow and outflow system. Inflow system results in spraying water on top of the sand layer, while the outflow system drain the water from the bottom of the specimen. A picture of the assembled test setup placed on the centrifuge platform is shown in Figure 5-9. Specifically, a bladder tank was used to supply pressurized inflow water to the spray nozzles. A proportional control valve (Model EPV-250B from Hass Mfg. of Averill Park, NY) was used to control the water discharge rate from the tank, and a differential pressure transducer (DPT) (Model P305D from Validyne Engineering Corp. of Northridge, CA) was used to monitor the volume of water leaving the tank. Pictures of the proportional control valve and the differential pressure transducer are shown in Figure 5-10.

Drainage from the eight ports in the outflow control plate of the laminar container is routed through steel pipes to an outflow tank. A second DPT was used to measure the volume of water accumulating in the outflow tank over time. A proportional control valve was incorporated into the drainage line from the laminar container at the connection to the outflow tank in order to prevent drainage from the bottom of the specimen during initial saturation of the sand layer, and to permit drainage of the sand layer during steady state infiltration in the centrifuge.

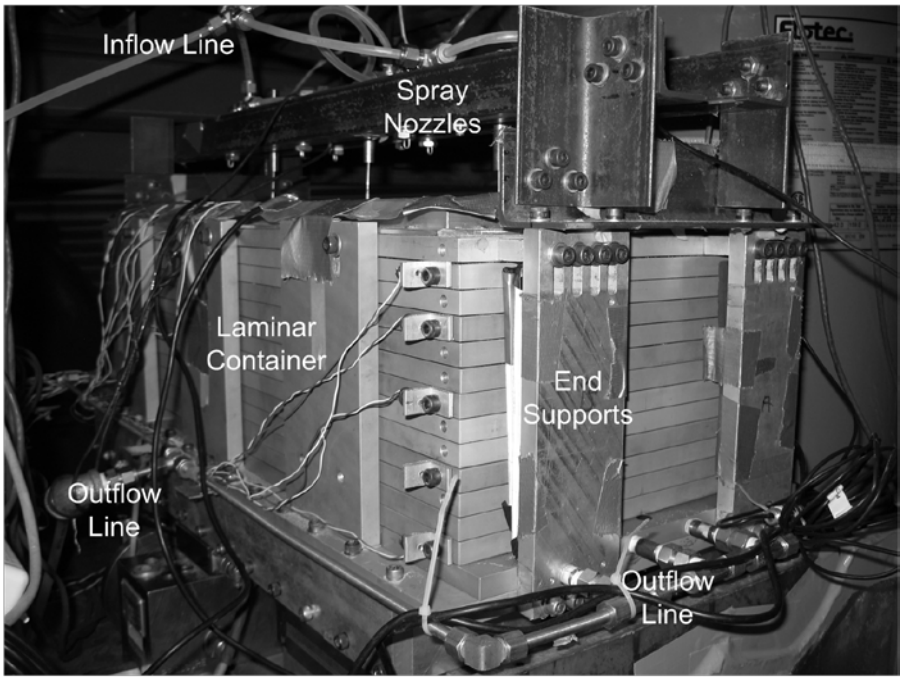

(a)

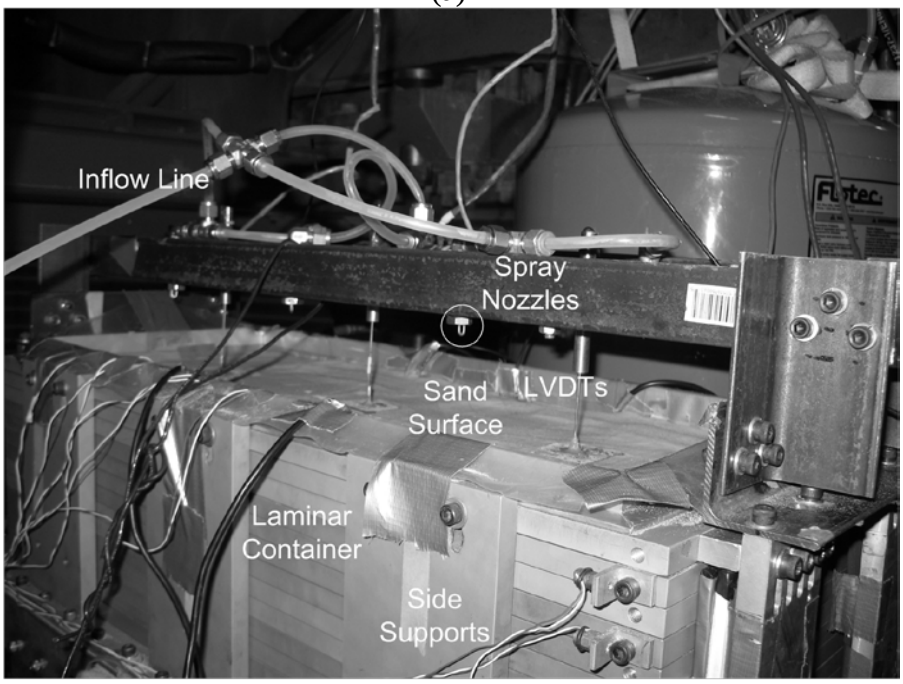

(b)

Figure 5-7. Pictures of the modified laminar container on the centrifuge platform

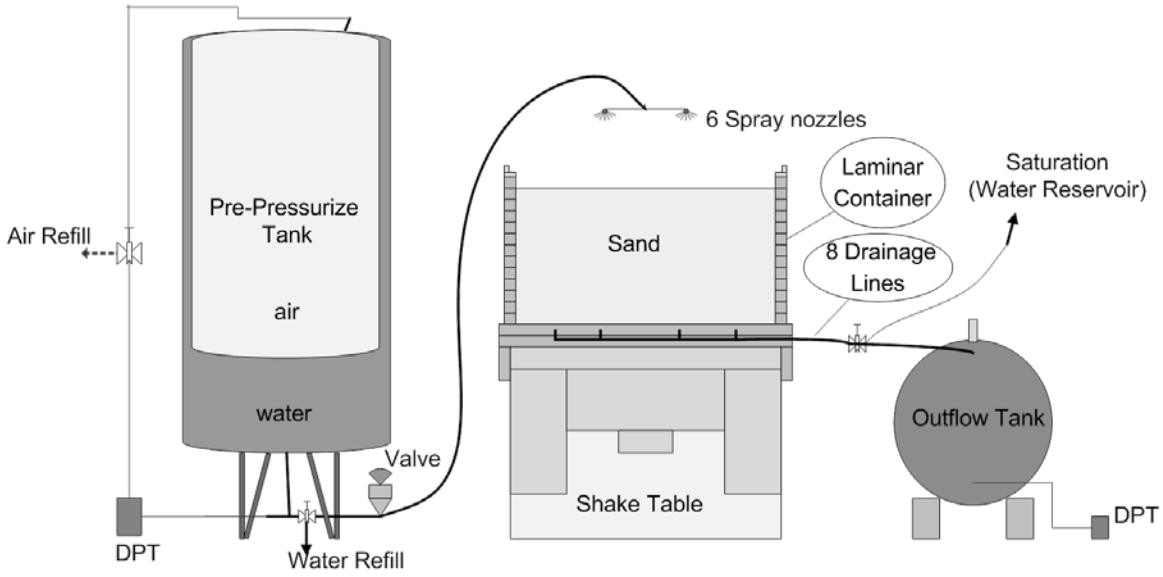

Figure 5-8. Schematic of infiltration system setup

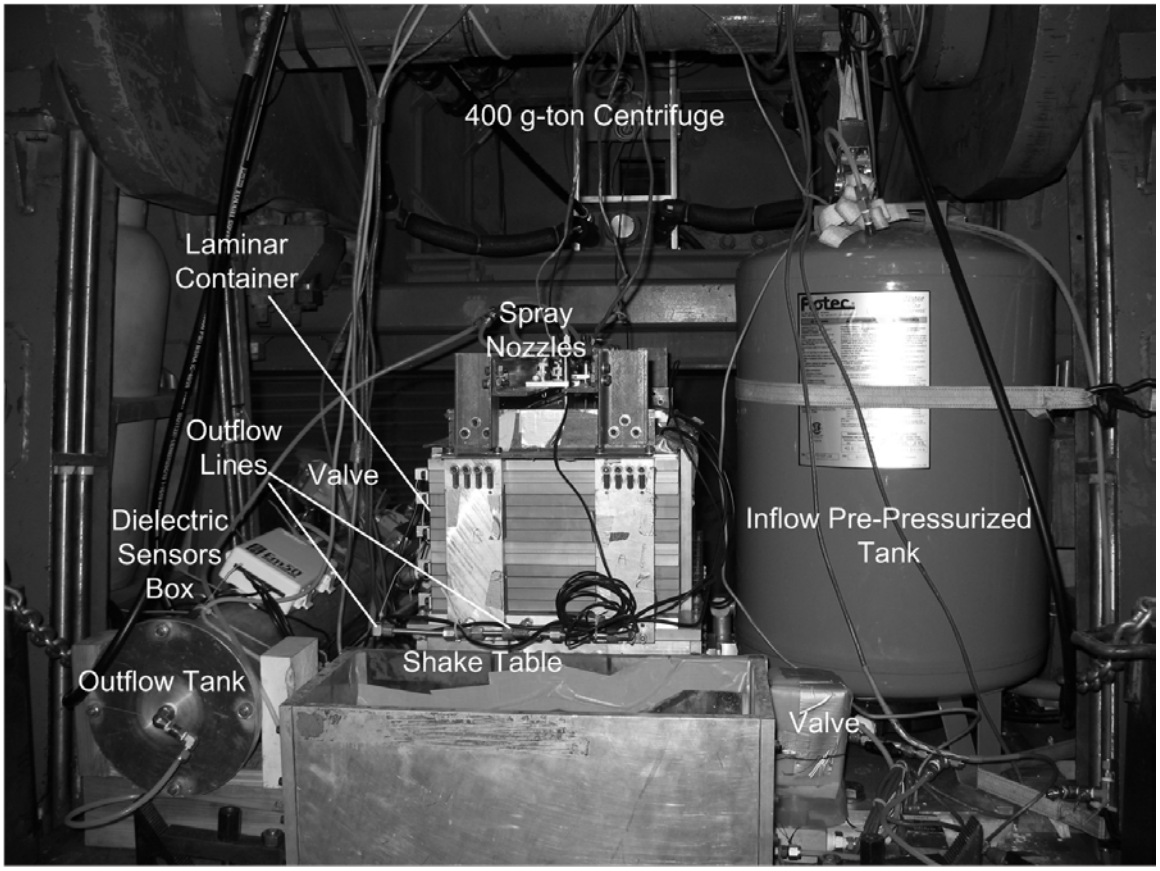

Figure 5-9. Picture of infiltration system setup

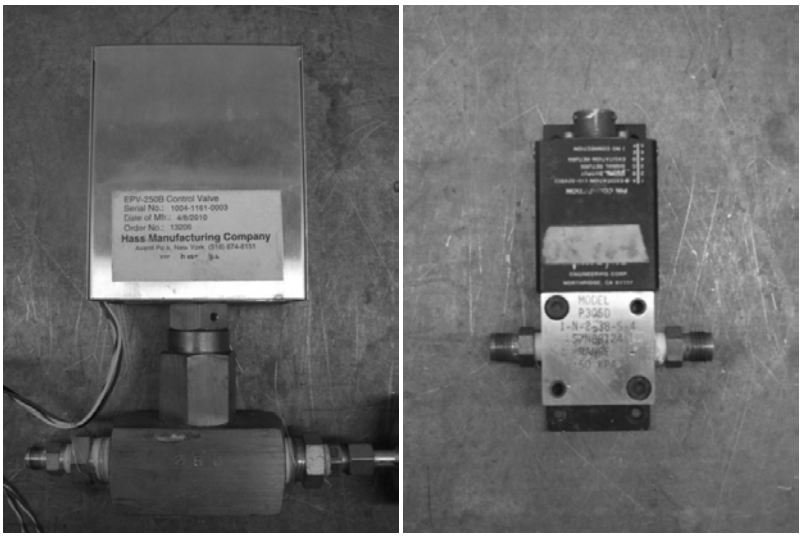

(a) (b)

Figure 5-10. (a) Proportional control valve (b) Differential pressure transducer

5.6 Instrumentation

The side- and front-view schematics of detailed instrumentation arrangement inside the laminar container are shown in Figures 5-11(a) and (b). Four types of instruments including dielectric sensors, accelerometers, pore pressure transducers (PPT), and linear variable differential transformers (LVDT) were used to study the seismic behavior of the sand layer. A close up picture of these measuring instruments is shown in Figure 5-12.

Four EC-TM® dielectric sensors from Decagon Devices of Pullman, WA were used to infer changes in volumetric water content with depth in the sand layer. These four sensors were placed horizontally, perpendicular to the shaking direction, at depths of 1.27, 5.08, 8.89, and 12.7 cm from the surface of the sand profile. The connecting wires were passed out of the top of the box, and were taped to the sides of the container.

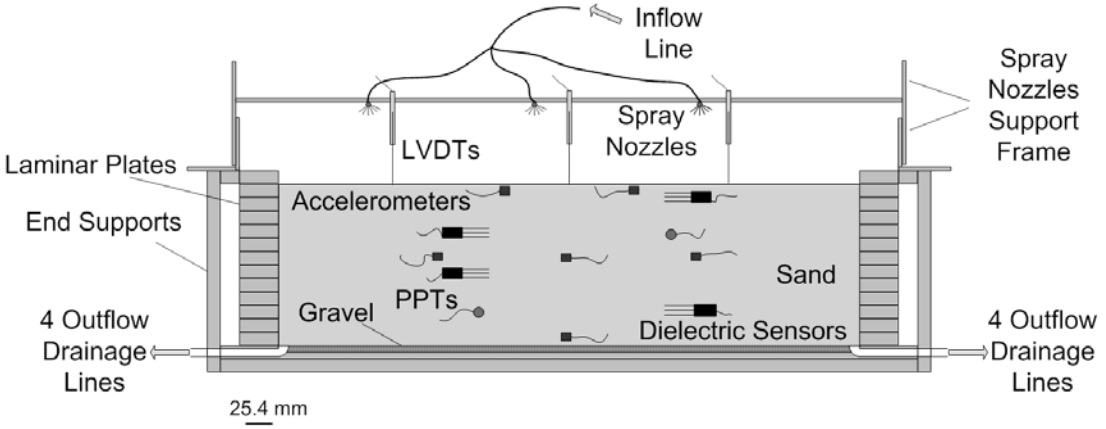

(a)

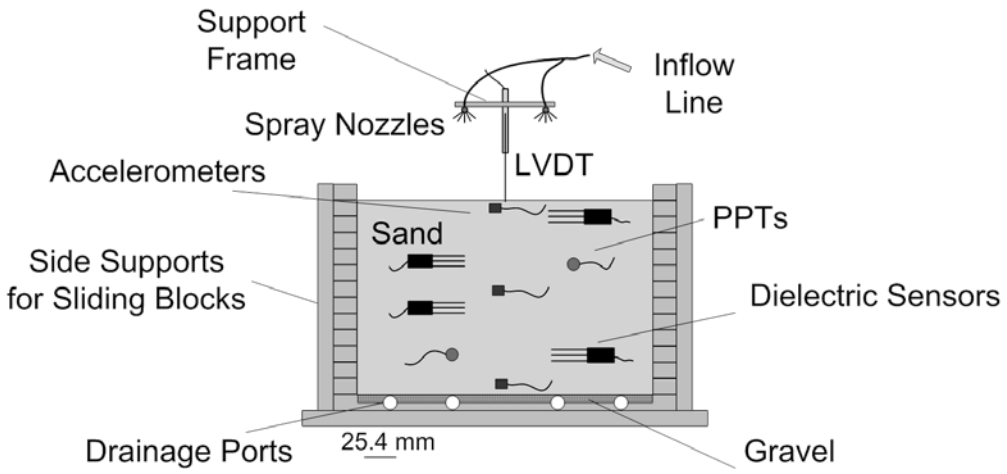

(b)

Figure 5-11. (a) Side view; (b) Front view schematic of laminar container with instrumentation

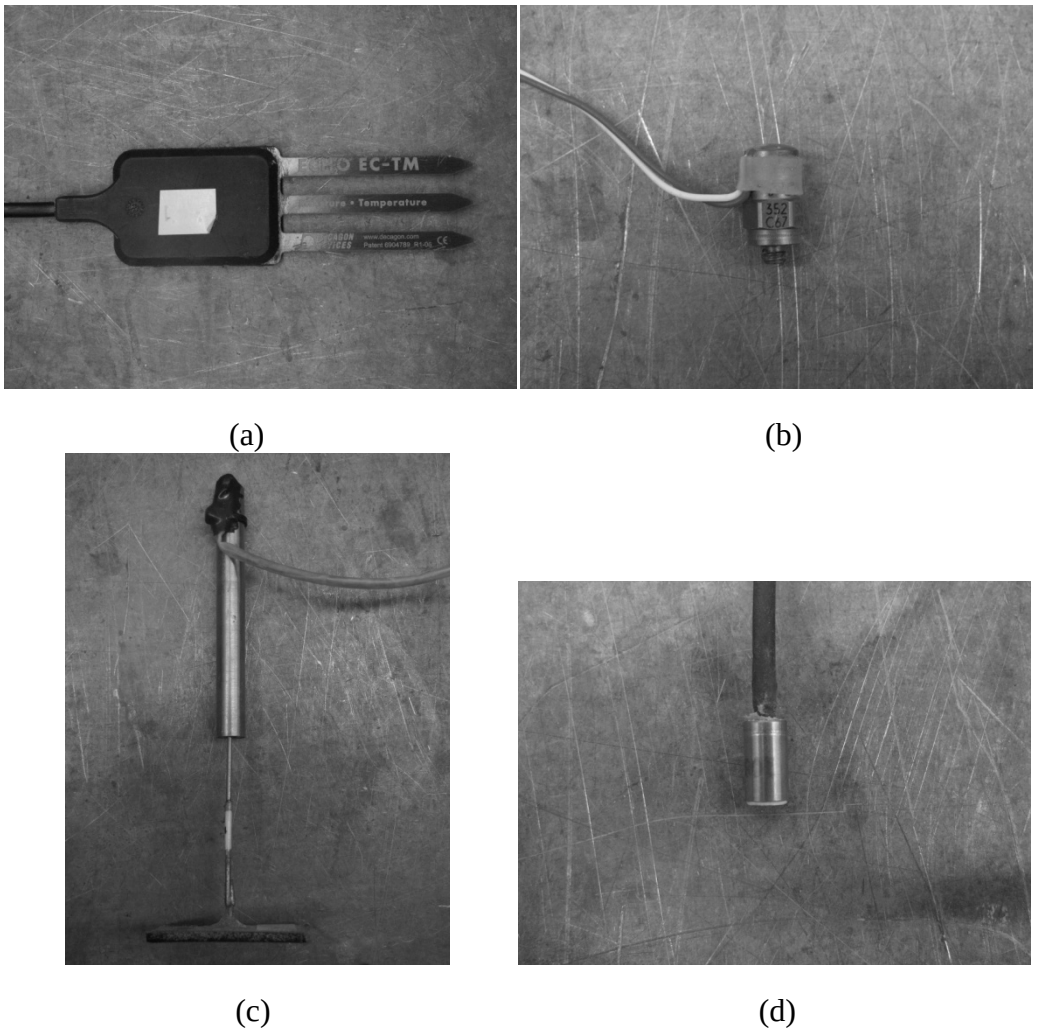

(a) (b)

(c) (d)

Figure 5-12. Picture of measurement instruments: (a) EC-TM® Dielectric Sensor; (b) PCB Accelerometer; (c) LVDT; (d) Druck PPT

Integrated Circuit Piezoelectric (ICP) accelerometers obtained from PCB Piezoelectronics, Inc. of Depew, NY were used to measure the induced acceleration time history at different depths in the soil layer and to check the uniformity of motion with horizontal distance in the soil layer during the shaking event. The accelerometers were buried at the surface and bottom of the sand layer and also at a depth of 7 cm, horizontally in the shaking direction.

Druck PDCR 81 pore water pressure transducers (PPTs) were used to measure the static pore pressure and generation and dissipation of excess pore pressures in the soil layer due to shaking. Although PDCR 81 PPTs are intended for use in fluid-saturated soils, they may be

used to measure the equilibrium values of matric suction as long as the matric suction magnitude is less than 60 kPa and the default porous stone is initially well-saturated (Muraleetharan and Granger 1999). The PPTs were buried at depths of 1.27 and 8.89 cm.

Three LVDTs mounted on the steel frame for the spray system on top of the laminar container, were used to measure surface settlements of the soil layer. The LVDT cores were mounted on 25-mm by 25-mm very thin plastic square footings to prevent punching of the core into the sand surface. A machine deflection test indicates that the deflection of the steel frame is less than 0.001 mm during centrifugation at 40g.

The instruments mentioned above were used when their measurements were required in the test. For example as it will be explained later, in bender element tests only dielectric sensors were implemented while in seismic compression tests all four instruments were used. Dielectric sensors where also used in the tests presented in this chapter in order to calibrate the infiltration setup.

5.7 Procedures

A flexible plastic sheet was used to separate the sides of the sand layer from the container. This sheet was used to prevent sand and water from penetrating into the gaps between the laminar container plates. Before assembly of the laminar plates, the sheet was glued to the inside of the bottom drainage plate. A flexible, waterproof glue suitable for both aluminum and plastic was used. After 48 hours of curing time for the glue, the laminar plates were re-assembled, as shown in Figure 5-13. All the sliding bearings between the rings were cleaned and placed at the right place to obtain the best performance of the container.

Figure 5-13. Picture of the assembled container

The drainage plate was filled with fine gravel having a uniform particle diameter of approximately 6.35 mm to serve as a drainage layer. The completed drainage layer is shown in Figure 5-14.

Figure 5-14. A layer of gravel served as a drainage layer

A nonwoven geotextile filter was placed on top of the gravel layer to provide separation between the gravel and the overlying sand layer. The filter after installation is shown in Figure 5-15.

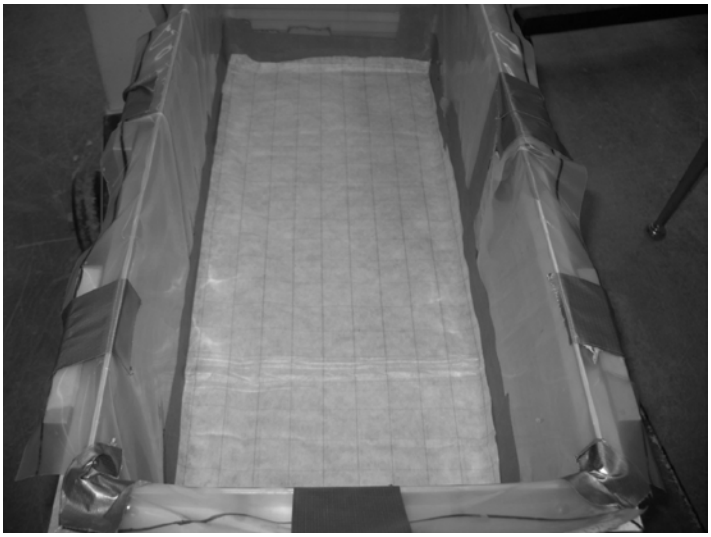

Figure 5-15. An interfacing fabric sheet separates gravel and sand layer

The sand layer was prepared using dry pluviation (Whitman and Lambe 1988) to reach a relative density of 45%. The sand was pluviated using a funnel with a strainer from zero height, so that provided a low relative density. The final thickness of the sand layer was 15.87 cm. The sand raining procedure is shown in Figure 5-16.

Figure 5-16. Sand layer preparation using dry pluviation

The different instruments were placed in the soil at different depths during pluviation as described above. The placement picture of dielectric sensors, PPTs, and accelerometers are shown in Figure 5-17 (a), (b), and (c). The pluviation was continued after the placing the

instrument at the desired position. Since the porous stone on the tip of the pore pressure transducers should be fully saturated, the placement area was locally saturated and then the transducers were placed as it is shown in Figure 5-17(b).

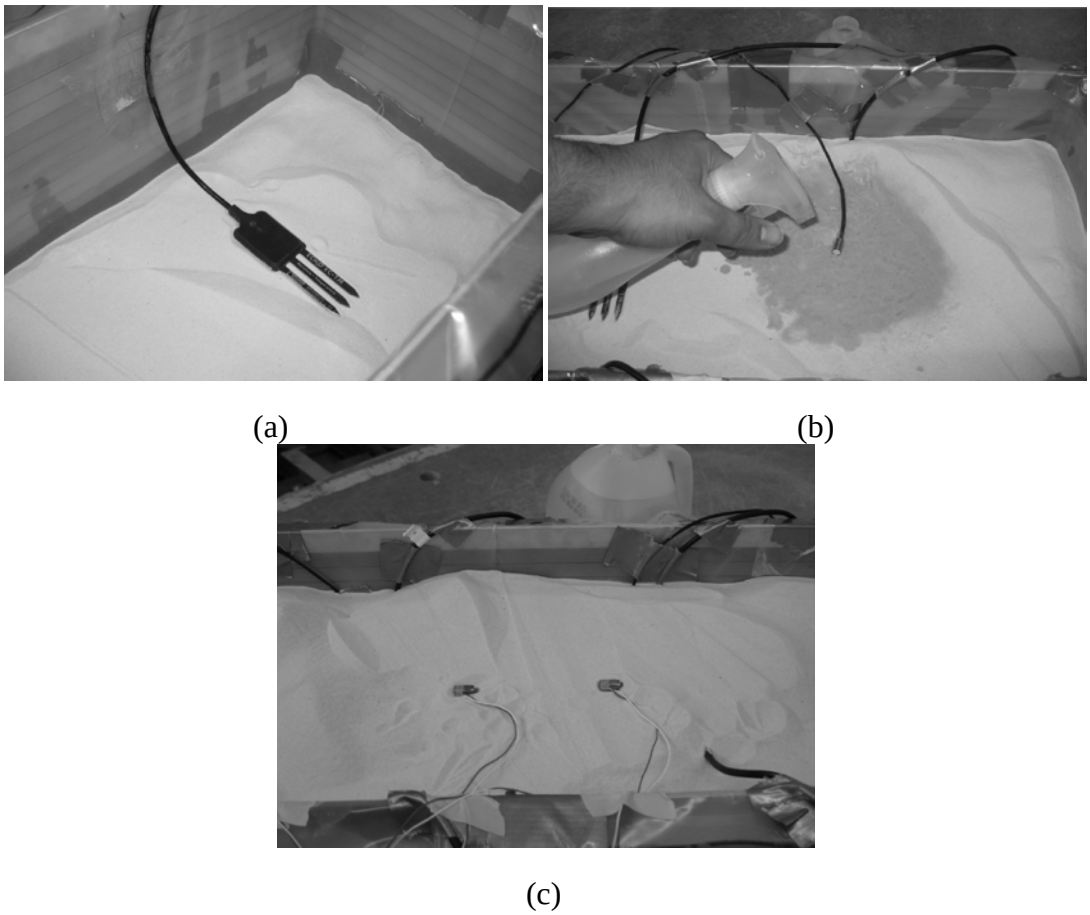

(a) (b)

(c)

Figure 4-17. (a) Dielectric Sensor; (b) PPT; (c) Accelerometers placement picture

The specimen was prepared within the container while it was atop a weighing balance. This permits assessment of the weight of each lift of soil during specimen preparation. The sand surface was leveled to obtain the desired specimen depth as shown in Figure 5-18. After preparing the sand layer and placing the instruments, the support frame for the spray nozzles and LVDTs was bolted to the container. Then, the LVDTs were mounted on the support frame and the container was placed on the centrifuge platform using the crane. A picture of the fully assembled container with the specimen inside is shown in Figure 5-19.

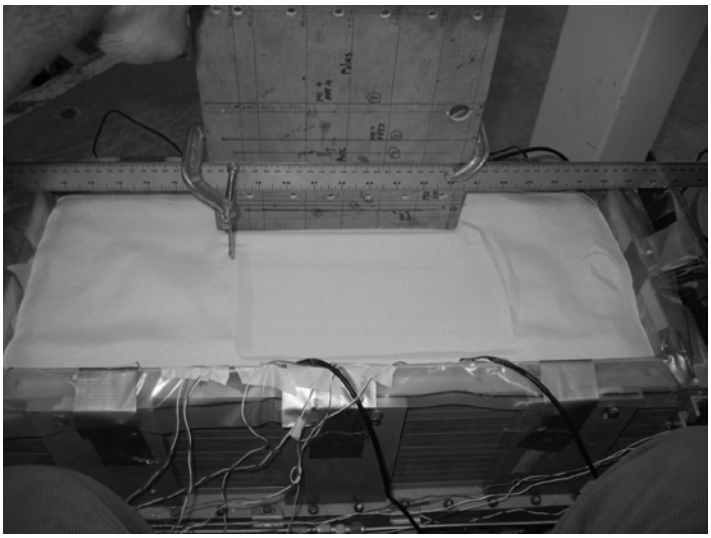

Figure 5-18. Leveling the sand surface

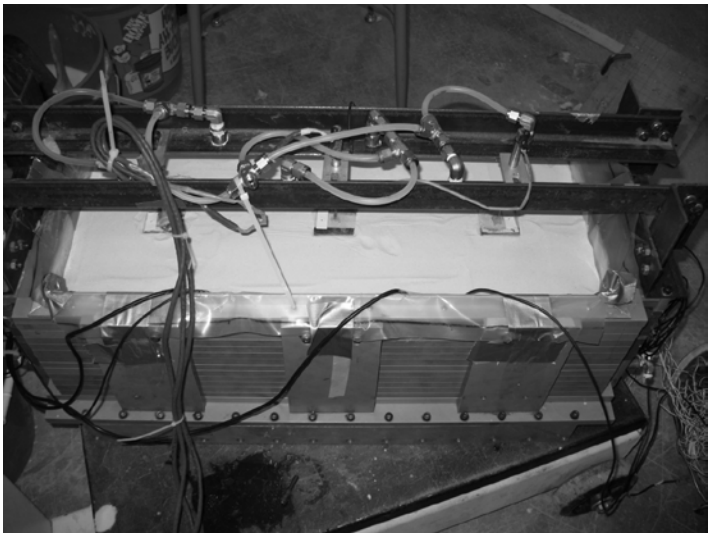

Figure 5-19. Laminar container after specimen preparation

After placement of the container on the centrifuge platform, the sand layer was saturated by connecting a de-aired water reservoir outside of the centrifuge to the drainage port at the bottom of the sand specimen (i.e., while the outflow proportional control valve is open). Dielectric sensors embedded at different depths in the sand layer were used to infer changes in volumetric water content during the saturation process.

After saturation was complete (i.e., when water reached the sand surface and dielectric sensors measured a uniform volumetric water content equal to the porosity), the outflow proportional control valve was closed and the de-aired water reservoir was disconnected from the container. Then, the centrifuge was spun up to a target gravitational acceleration of 30 or 40, defined at the mid-height of the container. Then, the outflow proportional control valve was fully opened and the inflow proportional control valve was opened by fractional amounts to reach different target infiltration rates (1v to 5v). In addition to a saturated soil layer with no infiltration, partially-saturated sand layers with infiltration rates of 10^{-10} to 10^{-3} liters/min were evaluated in this study in order to reach degrees of saturation of 0.16 to 0.76. In this manner, water was sprayed on surface of the soil layers until the measured outflow from the freely draining bottom boundary was equal to the applied inflow (steady-state conditions). Steady-state conditions were also assessed using the dielectric sensors at different depths in the soil layer; steady-state conditions were defined when the measured volumetric water content profile was uniform with depth. After reaching steady-state conditions with a uniform suction profile in the sand layer, the sand layer was subjected cyclic loading. Cyclic loading was used instead of earthquake loading in this study to simplify comparison of the seismic compression of sand layers with different degrees of saturation.

5.8 Suction Control in the Soil Profile using Steady-State Infiltration

Steady state infiltration through the sand layer was used to control the suction profile in the specimen. The volumetric water content is recorded continuously during the test using the dielectric sensors. An example of the variation in volumetric water content recorded by the dielectric sensors as a function of time during saturation and infiltration stage at a rate of 1.26×10^{-5} liters/min is shown in Figure 5-20. A close-up of the sensor readings during the infiltration process is shown in Figure 5-21. The curves in these figures indicate that a relatively uniform profile of volumetric water content was achieved after reaching steady-state conditions.

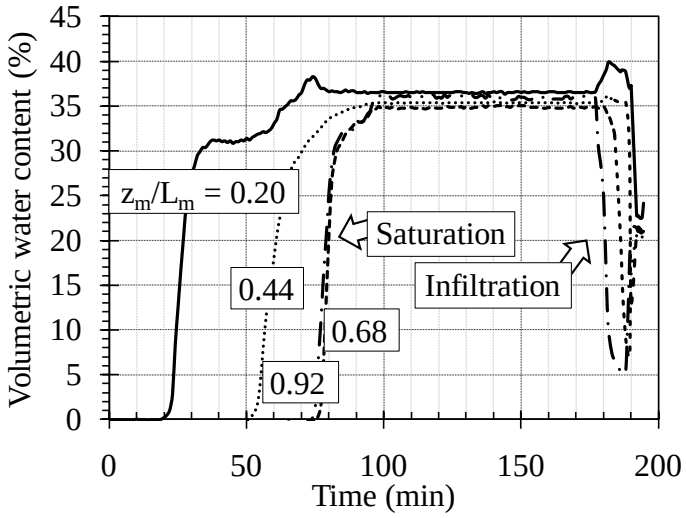

Figure 5-20. Water content variation in depth versus time

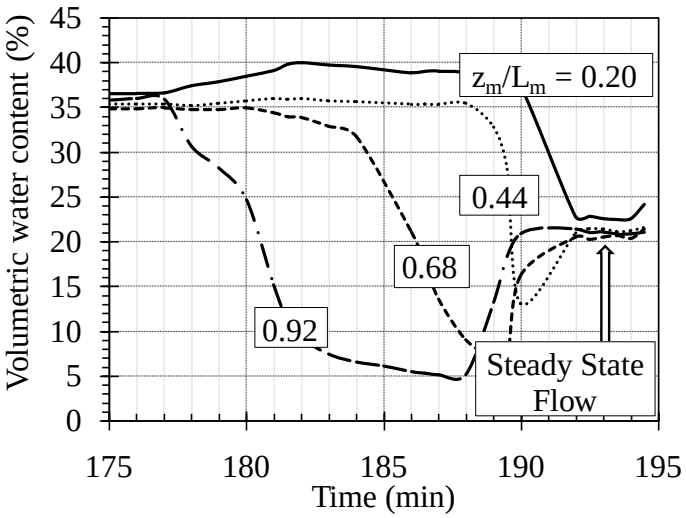

Figure 5-21. Water content variation in depth versus time in infiltration step

An evaluation of the theoretical suction profiles expressed in Equation 5-1 (using the parameters listed in Table 5-1) for different g-levels in Figure 5-22 indicates that the suction becomes more uniform with height in the sand layer as the g-level increases. Further, the transition zone from the portion of the soil layer undergoing infiltration under a unit gradient to the water table at the outflow boundary is also observed to decrease in length for higher g-levels. These results indicate that the g-level of 40g was suitable for ensuring uniform conditions in the soil layer. The effect of different infiltration rates on the theoretical suction profiles during

centrifugation at 40 is shown in Figure 5-23. Evaluation of the SWRC for Ottawa sand indicates that the specimen will have the same degree of saturation for suction values greater than 10 kPa, so this figure was used to identify the infiltration rates needed to reach suction values below 10 kPa.

Table 5-1. Parameters used for the solution to Richards' equation for water flow through partially-saturated sand during centrifugation in the laminar container

Parameter	**Value**
Soil layer height, L_m	15.875 cm
Radius at the outflow face, r_0	5.208 m
Water density, ρ_w	1000 kg/m^3
G-level at mid-height, $N_{r,mid}$	40.0
Gardner's HCF parameter, α	2.5 kPa^{-1}

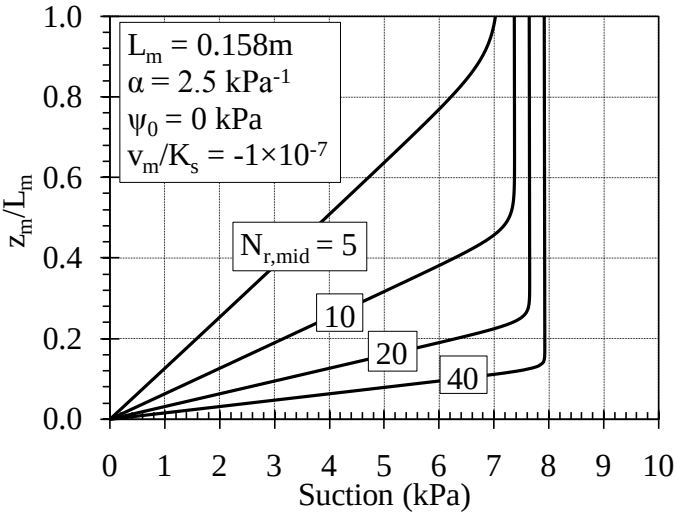

Figure 5-22. Suction profiles with depth for different g-levels from analytical solution to Richards' equation for steady-state infiltration of water through partially-saturated sand in the centrifuge

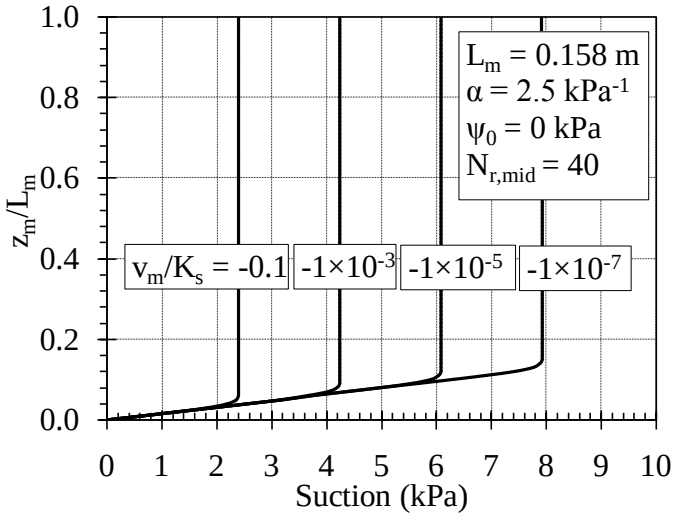

Figure 5-23. Suction profiles with depth for different discharge velocities from analytical solution to Richards' equation for steady-state infiltration of water through partially-saturated sand in the centrifuge

The theoretical suction profiles for the Ottawa sand layer during steady-state infiltration in the centrifuge, predicted using Equation 5-1, were converted to the theoretical degree of saturation profiles using the SWRC. The experimental degree of saturation profiles were defined by dividing the volumetric water content profiles measured at steady-state infiltration by the porosity of the soil measured at the beginning of the test. The experimental suction profiles were calculated from SWRC equation. The theoretical suction profiles were compared with the experimental suction profiles as shown in Figure 5-24. The theoretical and experimental degree of saturation profiles are also compared in Figure 5-25. The experimental results match well with the theoretical prediction, which confirms the concept of using steady-state infiltration to control suction in the soil layer.

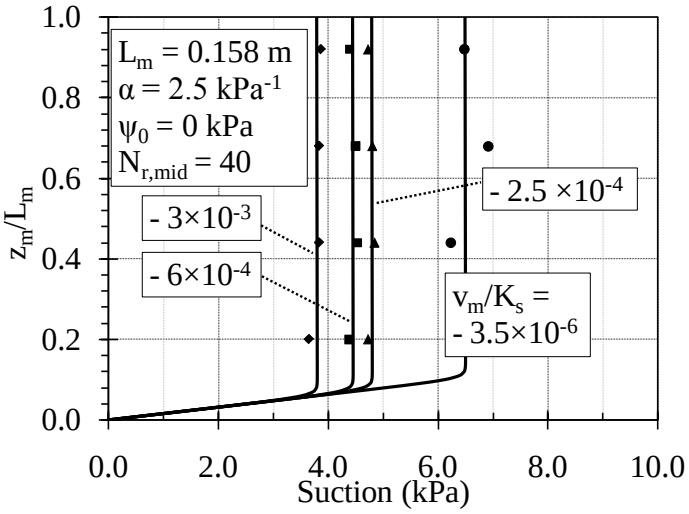

Figure 5-24. Comparison of experimental and predicted profiles of the suction during steady state infiltration

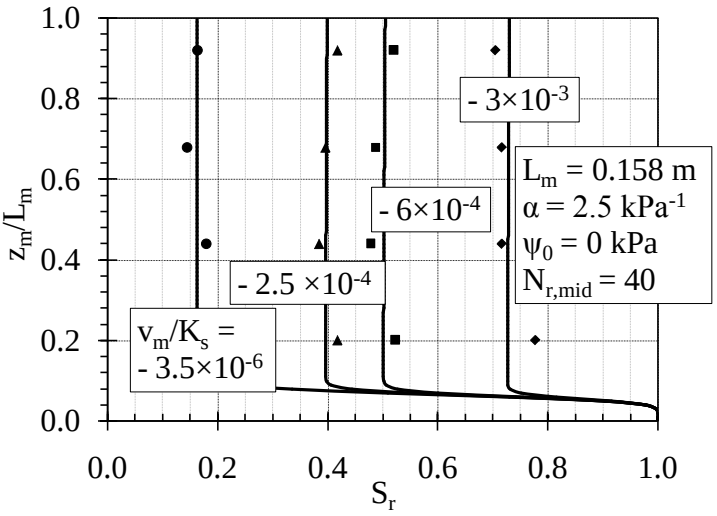

Figure 5-25. Comparison of experimental and predicted profiles of the degree of saturation during steady state infiltration

Although the suction is constant with height during steady state infiltration, the effective stress calculated from equation 2-26 will not be constant with depth. Specifically, the total stress in a soil layer will increase with depth in proportion to the bulk unit weight, while the suction stress will depend on the degree of saturation in the soil. Accordingly, changes in the rate of infiltration will lead to a shift in the effective stress profile with depth. Using the theoretical suction profiles in Figure 5-24 the effective stress profiles for different degrees of saturation

were calculated using Equation 2-26, as shown in Figure 5-26. Effective stress value at each depth is a key parameter in semi-empirical design approaches (e.g. estimating the small strain shear modulus) (Seed and Idriss 1970).

Cyclic load was applied to the container instead of earthquake load in this study to simplify comparison of the seismic compression of sand layers with different degrees of saturation. The details and specifications of the applied cyclic loads will be explained later.

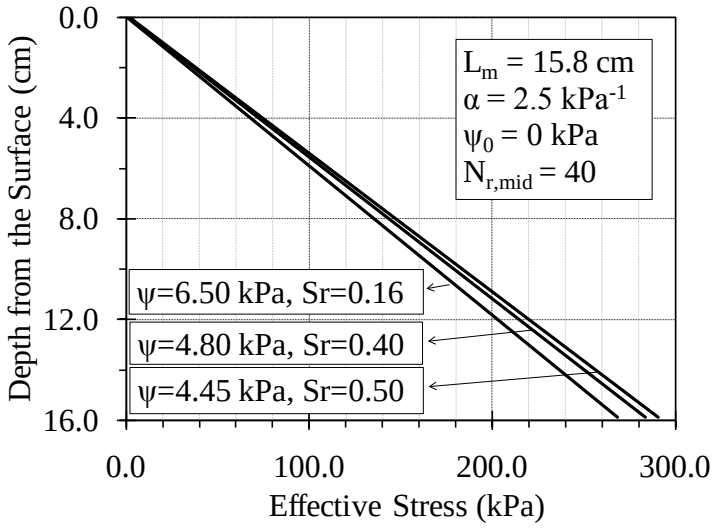

Figure 5-26. Predicted effective stress profiles in the soil layers having different degrees of saturation

CHAPTER VI

SMALL-STRAIN SHEAR MODULUS MEASUREMENT USING BENDER ELEMENT TEST

6.1 Objective

The small-strain shear modulus, G_{max}, is an important dynamic material parameter that is needed to predict the response of soil layers to dynamic loading. Because a new approach was used in this study to control the suction and degree of saturation in the soil layer (steady-state infiltration), it is important to evaluate the distribution in G_{max} throughout the soil layer using independent measurements. Bender elements were included in the soil layer for nondestructive measurement of G_{max} due to changes in suction and degree of saturation during changes in the infiltration rate into the soil layer. Shear wave velocity can be measured using a pair of bender elements by measuring the time difference between sending and receiving shear waves from one bender element to another. The shear wave velocity, Vs, is related to G_{max}, as in Equation 2-1 ($G_{max}=\rho V_s^2$). The G_{max} measurements from the bender elements were compared with those from the resonant column tests presented in Chapter 3, as well as from empirical equations.

6.2 Construction of Bender Elements

Three pairs of bender elements were manufactured for this study to measure the shear wave velocity through the soil depth. A single layer of T226-A4-303X type piezo-ceramic from PiezoSystems, Inc. having a length of 31.75 mm, a width of 12.7 mm, and a thickness of 0.67 mm was used to form each of the bender element pieces. The picture of a piezo-ceramic disk

is shown in Figure 6-1(a). The piezo-ceramic disk was cleaned and soldering solution was applied to one end of the ceramic in both sides. Then, a miniature coaxial cable from Belden Electronics was connected and soldered to each side of the piezo-ceramics as shown in Figure 6-1(b).

(a) (b)

Figure 6-1. (a) T226-A4-303X type piezo-ceramic; (b) Soldering the coaxial cable

After connection of coaxial cables to each side of the piezo-ceramics, several coats of nonconductive liquid Polyurethane (M-COAT A from Vishay Electronics) were applied to prevent corrosion in partially saturated soils. A layer of silver print was then applied to mitigate electrical noise from being transmitted to the piezo-ceramics. After connecting grounding cables to the silver print, several additional coats of polyurethane were applied to the piezo-ceramic. The completed bender elements [shown in Figure 6-2(a)] were potted with epoxy within cylindrical steel pipes (having lengths of 38.1 mm and inside diameters of 15.24 mm) so that the free vibrating length of the exposed piezo-ceramic was 17.78 mm. A picture of the completed bender element unit is shown in Figure 6-2(b).

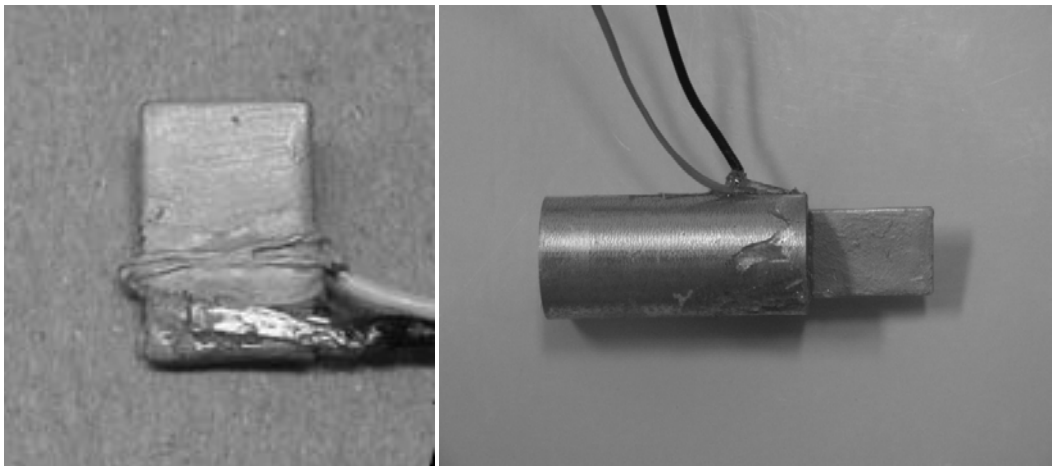

(a) (b)

Figure 6-2. (a) Coated bender element with connected wires; (b) Completed bender element unit

6.3 Bender Element Testing Setup

The laminar container used previously for seismic compression tests was adopted for bender element testing. For this purpose, the container was further modified by including two pedestals used to support bender elements, as shown in schematic in Figure 6-3. Each pair of bender elements were installed on the vertical support pedestals so that they would be at depths of 3.51, 7.31, and 11.11 cm from the soil surface. The bender elements were oriented in a vertical direction so that they would generate SH waves. This is important in centrifuge testing so that the self-weight of the soil does not provide a downward reaction on the side of the flat side of the bender elements. A 100-mm square flange at the bottom of the pedestals was affixed to the base of the centrifuge container using rubber cement. After aligning the two support pedestals, the horizontal distances (tip-to-tip) between the bender elements were 7.25, 7.55, and 7.75 mm for the top, middle and bottom pairs of bender elements respectively. A picture of the bender elements and the support pedestals during placement of the sand layer is shown in Figures 6-4(a) and 6-4(b).

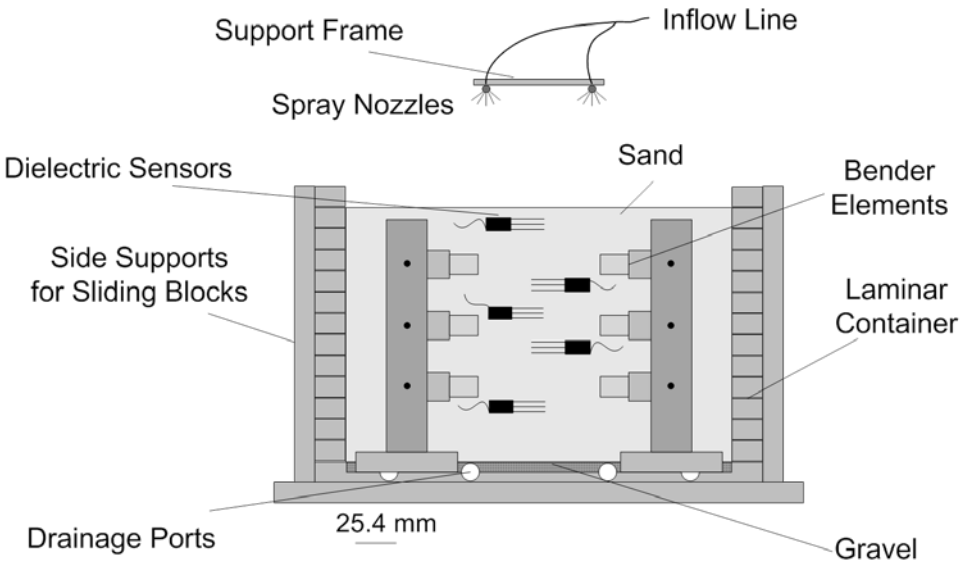

Figure 6-3: Elevation-view schematic of bender element arrangement in the sand container

(a) (b)

Figure 6-4: Picture of bender element arrangement in the sand container: (a) Bender element pedestals; (b) Pluviation of sand around the pedestals

A data acquisition system capable of generating and measuring signals to the bender elements was developed so that the bender elements could be used during flight in the centrifuge. A schematic of the data acquisition system is shown in Figure 6-5. A National Instruments PXI chassis with a NI-8176 DAQ controller was used in this study. An 8-channel PXI-6251 module was used for output signal generation and input data measurement. The maximum amplitude of

the generated signal from the PXI-6251 module is ±10V, which is not sufficient to generate a signal which can be measured by the receiving bender element above the noise of the centrifuge. Accordingly, an EPA-104 linear amplifier manufactured by Piezo Systems Inc. was used to increase the amplitude of the generated wave to ±200V. Since the amplifier has only one input and output channel a PXI-2527 switch was used to guide the generated wave to the desired transmitting bender element. This system is similar to that of Kim and Kim (2010), although a multiplexer was not required in this study due to the fewer number of channels.

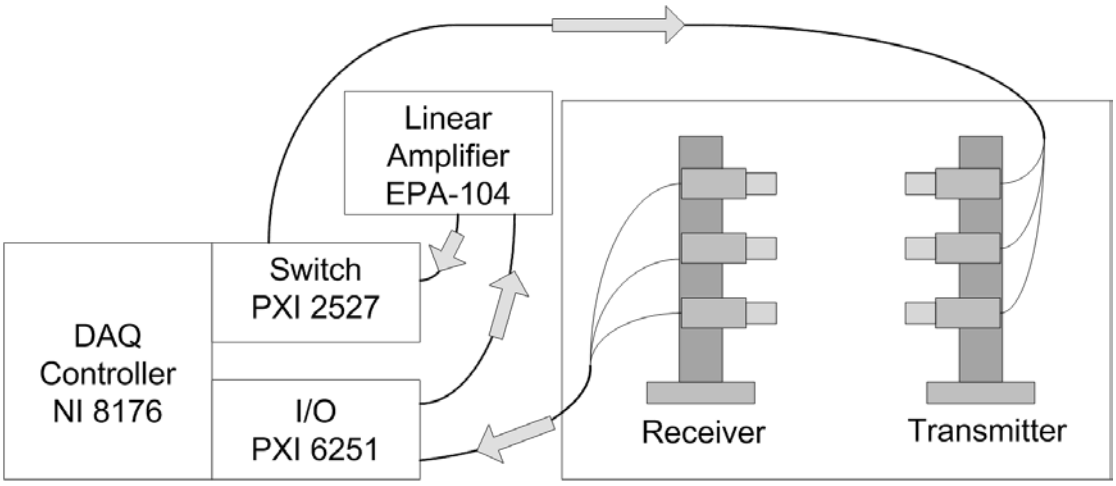

Figure 6-5: Schematic of the on-board centrifuge data acquisition system configuration for the bender elements

Steady-state infiltration was used to control the degree of saturation and matric suction in the partially-saturated soil layer in the centrifuge container. The same infiltration set up as described in previous chapters was used to reach a uniform suction profile in a layer of the sand. A schematic of the infiltration and drainage systems is shown in Figure 6-6. The changes in volumetric water content in the soil layer were measured using five EC-TM® dielectric sensors from Decagon Devices of Pullman, WA, as shown in Figure 6-3. These sensors were placed in a horizontal orientation, as far as possible from the bender elements, at depths of 1.27, 5.08, 7.30, 8.89, and 12.7 cm from the surface of the soil layer.

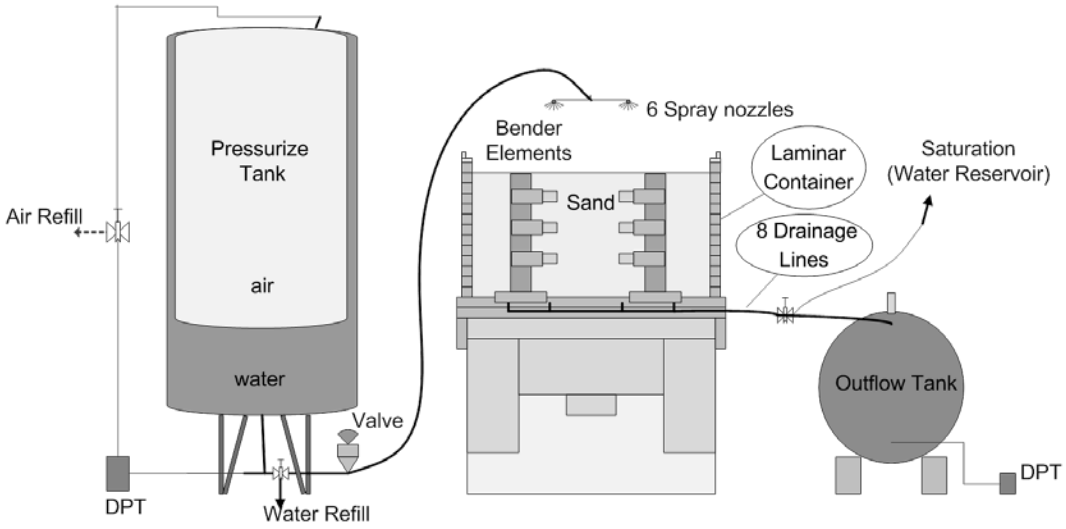

Figure 6-6. Schematic of the infiltration system setup showing the location of the bender elements

6.4 Bender Element Testing Procedure

The sand specimen was prepared in a fully assembled container using the same method as explained in specimen preparation chapter to a relative density of 45%. The final thickness of the sand layer was 15.87 cm. The dielectric sensors were placed in the soil during pluviation. Bender element tests were performed on dry, saturated and partially saturated specimens consecutively. The saturation process was explained in chapter 5-3. After saturation of the soil layer, the centrifuge was spun up until reaching a target gravitational acceleration (defined at the mid-height of the container). Then, the steady state infiltration method was used to reach the target degree of saturation. Degrees of saturation ranging from 0.11 to 0.71 were obtained in the partially saturated soil layers for infiltration rates ranging from 10^{-10} to 10^{-3} liters/min. Profiles of degree of saturation and suction with height in the sand layer at steady state conditions under different infiltration rates are shown in Figures 6-7(a) and (b) respectively.

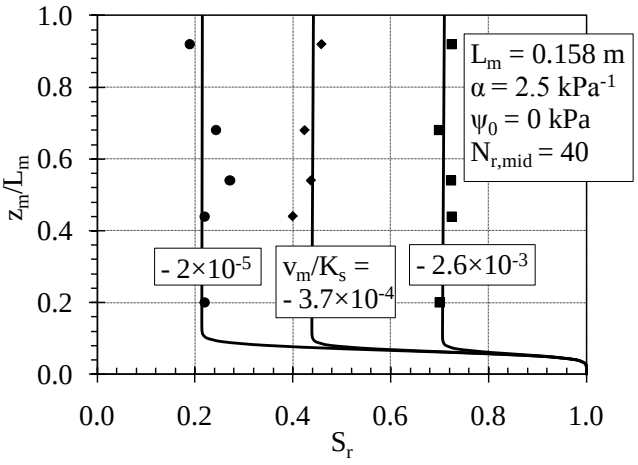

(a)

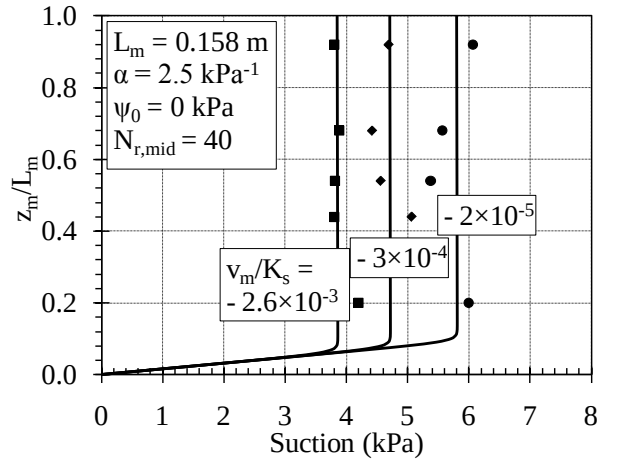

(b)

Figure 6-7. (a) Comparison of experimental and predicted profiles of the (a) degree of saturation; (b) suction during steady state infiltration

After reaching steady-state conditions with a uniform suction profile in the sand layer, bender element tests were performed. A 10V amplitude sinusoidal pulse wave (amplified to 200V) with a frequency of 10 and 20 kHz was generated to measure the shear wave velocity of the sand between the two bender elements. The transmitted signal and a typical received signal are shown in Figures 6-8(a) and (b), respectively. The shear wave travel time was calculated by subtracting the first arrival time of the shear wave recorded by receiver benders from the time at which the transmitted signal was sent. Each test was repeated several times (5 to 20 times)

and the calculated travel times were averaged. The repeat measurements were consistently within 1.5% of each other.

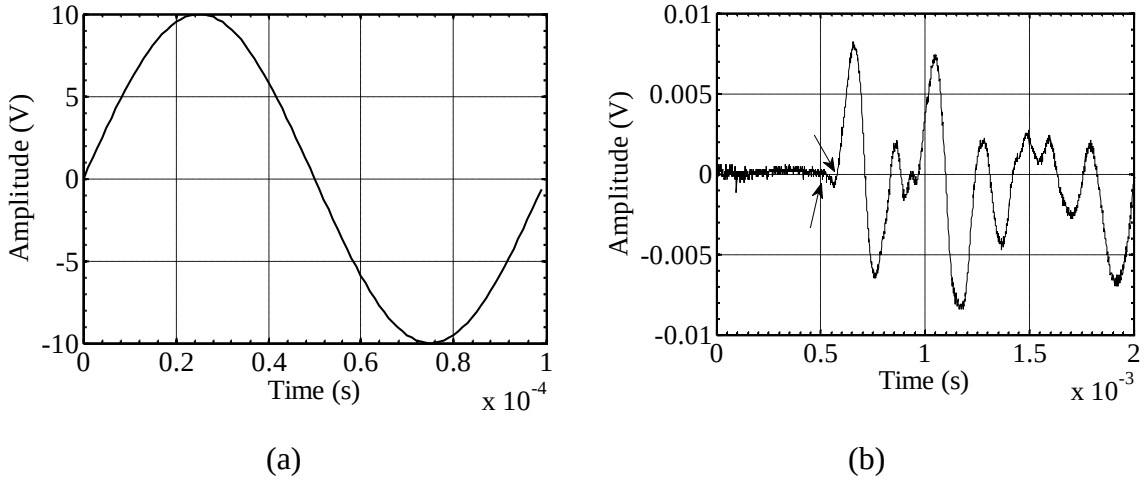

(a) (b)

Figure 6-8. Typical results from bender element testing: (a) Generated shear wave; (b) Received shear wave signal

The definition of the arrival time is a major challenge in bender element data analysis. Four methods have been proposed in the literature to infer the travel time (Viggiani and Atkinson 1995; Arulnathan et al. 1998), including the: (1) first deflection point (FDP) of a received pulse, (2) time difference between two characteristic points, (3) travel time from cross-correlation method (CCM), and (4) travel time inferred from the cross-power spectrum of transmitter and receiver signals. In each of these approaches the travel distance is commonly assumed as the tip to tip distance between the bender elements. Lee and Santamarina (2005) used the cross-correlation method to propose that the zero amplitude before the first major peak can be used as the first arrival time. They observed a small local minimum or maximum deflection in the received signal before the first major peak, and attributed this deflection to near field effects in the container. Leong et al. (2005) observed that the travel time defined using the first deflection point provides the best match with independent shear wave velocity measurements from ultrasonic pulse tests. The definition of each of the points used in the definition of the travel time using the FDP and CCM methods are shown in a schematic signal in Figure 6-9. In general, the CCM method was found to be less ambiguous to define the arrival time due to the

prominence of the first major peak. However, the results indicate that the FDP results provide more consistent results with other measurements, as discussed later.

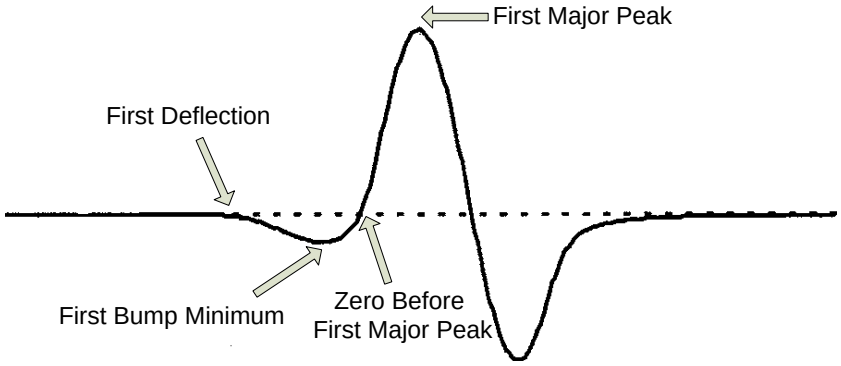

Figure 6-9: Schematic describing different approaches to define the arrival time for a shear stress wave in soils

6.5 Saturation Effect on Small-Strain Dynamic Shear Modulus

Pulse wave tests were performed for each pair of bender elements independently after reaching steady state conditions. The value of G_{max} for a given test divided by the value of G_{max} for dry sand as a function of degree of saturations for the bender elements at depths of 3.51 and 11.11 cm at 40g are shown in Figures 6-10(a) and (b) for the cross-correlation and first deflection point travel time definitions, respectively.

The received signal at a depth of 7.31 cm was detected, but it was not sufficiently greater than the noise level in the centrifuge. This was attributed to a short-circuit in the bender element electrical connections after it was submerged in water, so the results from a depth of 7.31 cm are not reported in this study. The G_{max} values calculated based on the first deflection point approach are higher than the values based on the cross-correlation method due to shorter time travel in this method (note the higher value of $G_{max\text{-}dry}$ for the first deflection point data). Regardless of the travel time calculation method, a peak value of $G_{max}/G_{max\text{-}dry}$ is observed at a degree of saturation about 0.4. This observation is consistent with measurements in the literature for sands (Qian et al. 1991; Khosravi et al. 2010), and confirms that G_{max} increases due to the impact of matric suction on the effective stress in the sand. Consistent with these studies, the bender element deeper in the soil profile shows a slightly greater variation in shear modulus with the degree

of saturation due to the impact of the greater net normal stress ($\sigma_n = \sigma - u_a$).

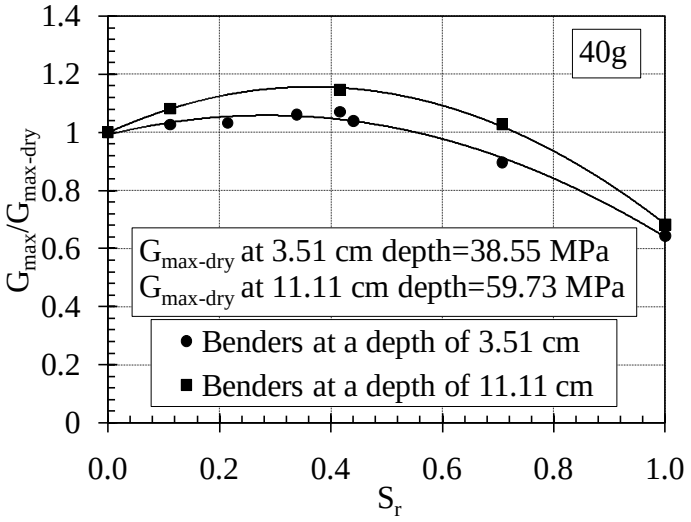

(a)

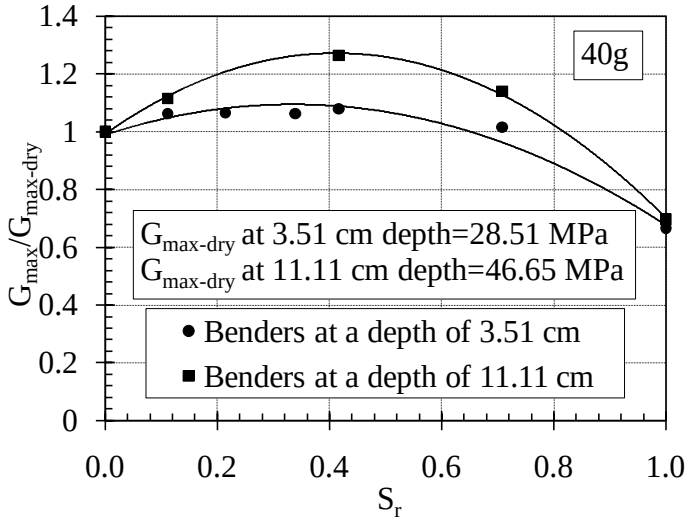

(b)

Figure 6-10: Relationship between $G_{max}/G_{max-dry}$ and degree of saturation for bender elements at 40g based on: (a) The first deflection point; (b) The zero before the first major peak using the cross-correlation method

6.6 Bender Element vs. Resonant Column

Khosravi et al. (2010) used a fixed-free Stokoe-type resonant column apparatus with suction control using the hanging column technique (McCartney et al. 2008) to measure the value of G_{max} for the same sand used in this study, albeit at a relative density of 50%. A

comparison between the variation in G_{max} with degree of saturation for the bender element (BE) (in the centrifuge) and resonant column (RC) tests is shown in Figure 6-11.

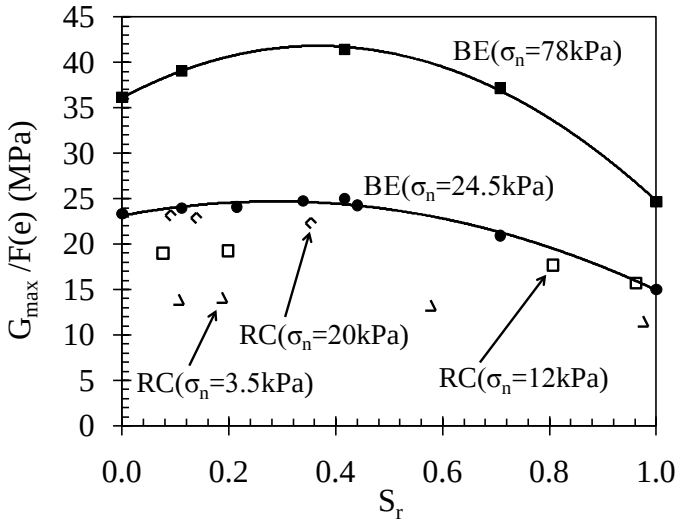

Figure 6-11: Variation in the value of G_{max} normalized with respect to the void ratio function with degree of saturation for sands evaluated under different net normal stress values in bender element (BE) and resonant column (RC) tests (σ_n is the net normal stress)

Because of the different densities, the G_{max} from both tests were normalized using the void ratio function defined by Hardin (1978) [$F(e)=1/(0.3+0.7e^2)$]. The total stress values reported for the bender element test results account for the effect of the different degrees of saturation on the total soil density. The G_{max} values from the bender element tests in this figure were calculated based on the first deflection point method. The normalized RC and BE G_{max} data have a consistent trend with the degree of saturation. The magnitudes of G_{max} for the RC and BE data having similar net normal stresses are especially consistent. Consistent whith the observations of Leong et al. (2005), the results in Figure 6-11 indicate that the first deflection point method may be a more appropriate definition for the shear wave travel time.

6.7 Impact of Effective Stress on G_{max} of Dry and Saturated Sands

The mean effective stress for the sand was calculated by multiplying the effective stress by $(1+2K_0)/3$, where K_0 is the coefficient of earth pressure at rest estimated using the friction

angle $\Phi = 35°$ (K_0=1-sinΦ) for the sand having a relative density of 45% from Shertmann's chart of Φ vs. Dr (1978). The variation in G_{max} for different effective stress is shown in Figure 6-12 using both travel time calculation methods along with different forms of Equation 2 from the literature (Hardin and Richart 1963; Seed and Idriss 1970; Hardin and Drnevich 1972). Consistent with the comparison with observations from the resonant column tests, the G_{max} values calculated using a travel time based on the first deflection point match better with the predictive empirical equations.

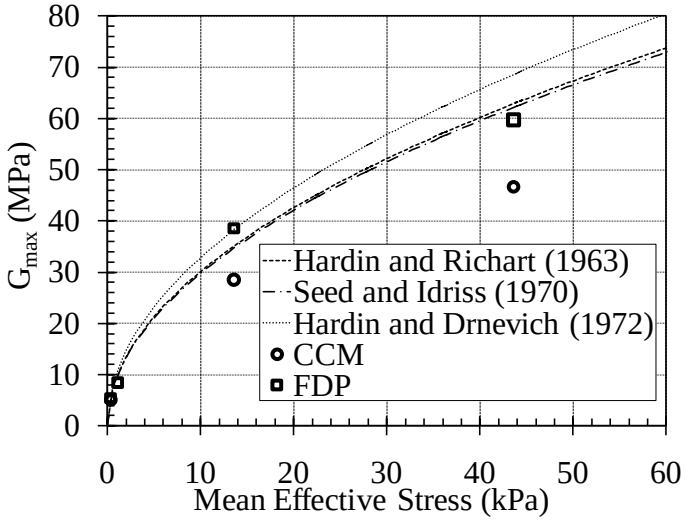

Figure 6-12: Effective stress dependent small-strain shear modulus for dry sand with data interpreted using both the cross-correlation method (CCM) and the first deflection point (FDP) method.

The variation in G_{max} with mean effective stress for saturated sand is shown in Figure 6-13. Consistent with the plots of $G_{max}/_{Gmax\text{-}dry}$ in Figure 6-10, the G_{max} values for saturated sands are lower than those for dry sands at the same effective stress, especially under higher effective stresses. A best fit equation for G_{max} of the saturated sand indicates a value of n = 0.4 may be more appropriate for the saturated sand, indicating that the values of n and A may be sensitive to the degree of saturation.

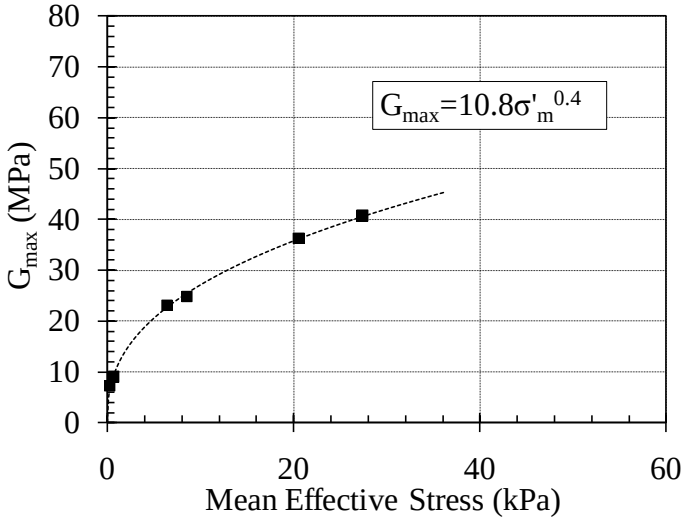

Figure 6-13: Effective stress dependent small-strain shear modulus for saturated sand data defined with the FDP method

6.8 Impact of Effective Stress on G_{max} of Partially-Saturated Sand

There are many equations available in the literature to estimate the effective stress of partially saturated soils. Recently, Lu et al. (2010) used the concept of suction stress to define the effective stress of partially-saturated soils, where suction stress is a function of matric suction and degree of saturation. They incorporated the relationships between matric suction and the degree of saturation (i.e., the soil-water retention curve or SWRC) such as that of van Genuchten (1980) and developed a functional form for the effective stress of partially-saturated soils, as in Equation 2-26. This definition of effective stress was used in this study because it incorporates the conventional van Genuchten (1980) model parameters and does not require additional shear strength tests to define the suction stress, as required by Lu and Likos (2006). The mean effective stress for the partially saturated sands was calculated using the same method as dry sand using the same friction angle. The G_{max} data is plotted as a function of the mean effective stress defined with Equation 2-26 along with a best fit power function in Figure 6-14.

The trend in G_{max} versus the mean effective stress plot for all saturation conditions is shown in Figure 6-15. This figure also incorporates data points that were obtained at a g-level of

50, to show that the trend in G_{max} is only dependent on the mean effective stress. These results indicate that a single equation may be used to predict the value of G_{max} of this particular sand regardless of the degree of saturation, as long as the effective stress of the partially saturated sand is defined using an approach such as Equation 2-26. The data points followed the curve whose equation is shown in this figure, and generally fell within a tolerance of ±10%.

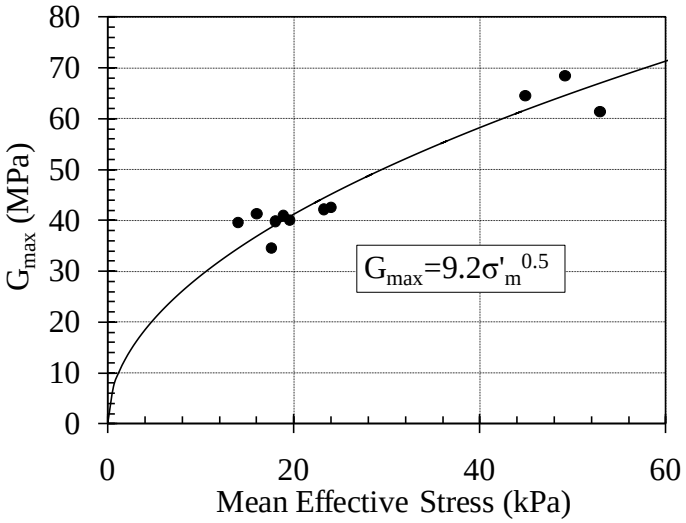

Figure 6-14. Effective stress dependent small-strain shear modulus for partially saturated sand defined with the FDP method

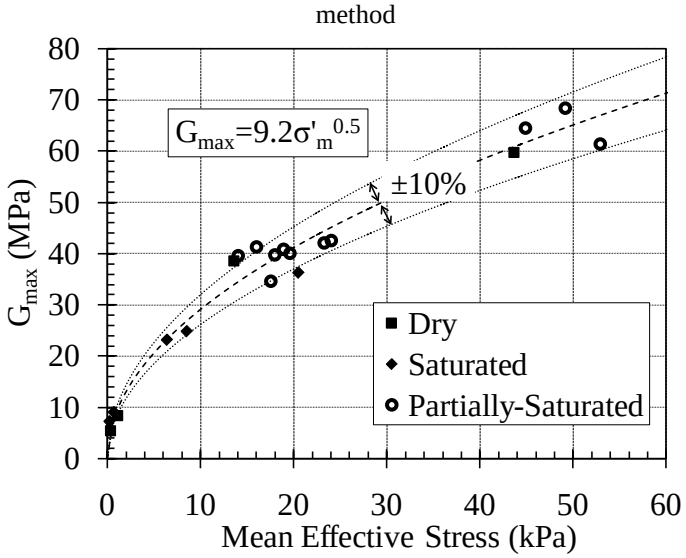

Figure 6-15. Comparison between small strain shear modulus of Ottawa sand under dry, saturated, and partially-saturated conditions as a function of mean effective stress

CHAPTER VII

SEISMIC COMPRESSION OF PARTIALLY-SATURATED SAND UNDER CYCLIC LOADING

7.1 Cyclic Test Characteristics and Scope

Cyclic load was selected to study the seismic compression of partially-saturated sand, because of its simplicity and easy interpretation. The cyclic load was applied using an in-flight shake table when the centrifuge was spinning and when the target saturation level was achieved. About 50 cyclic tests on dry, saturated and partially-saturated specimens were performed where 27 tests were done successfully, and the other 21 tests were for calibration purposes or not successful due to experimental errors. The purpose of the calibration tests were to check the laminar container's performance which will be explained later, experience the infiltration process, and improve the shake table performance. The test schedule, conditions, and number of repetition are summarized in Table 7-1. The test conditions mentioned in this table including target degree of saturation range, g-level, target cyclic amplitude, cyclic frequency, number of cycles, and pore fluid. The cyclic loading conditions listed in the table are at the model scale and where frequency and amplitude is N-times higher than the prototype scale in N-g models.

Table 6-1. Cyclic test schedule and scope

Target S_r	g-level	Shake Table Target Amp (g)	Frequency (Hz)	Number of Cycles	Pore Fluid	Number of Tests
Dry (S_r = 0.00)	40, 30	40, 30	40, 30	15	Water	3
Partially-saturated (0.00< S_r <0.20)	40	40	40	15	Water	1
Partially-saturated (0.20<S_r<0.40)	40, 30	40, 30	40, 30	15	Water	3
Partially-saturated (0.40<S_r<0.60)	40, 30	40, 30	40, 30	15	Water	10
Partially-saturated (0.60<S_r<0.80)	40, 30	40, 30	40, 30	15	Water	4
Saturated (S_r=1.00)	40, 30	40, 30	40, 30	15	Water	5
Saturated (S_r=1.00)	40	40	40	15	Metolose	1
Total						**27**

The tests listed in Table 6-1 were performed at two different g-levels including 30 and 40g. Shake table amplitude was controlled by the amount of voltage applied where at 40 g-level an amplitude of 1.2 V causes the shake table to shake with acceleration amplitude of about 40 g while 0.9 V leads to 30 g. Although the target amplitudes were 30 or 40 g, but the measured horizontal acceleration on the shake table was not always at the same exact values. That difference was due to the hydraulic pump performance. The desired number of cycles applied to the container through the shake table was 15 cycles which was a standard number of cycles in the literature for an earthquake with the magnitude of 7.5. However, there were two additional small amplitude cycles, one at the beginning and one at the end of the loading, applied to the container due to the fact that the shake table starts and stops the cyclic loads not with the full amplitude power and it reaches the desired amplitude and stops cycling in a gradual manner. It should be also noted that there is a small decaying trend in the cyclic amplitude due to loss of hydraulic power.

There were a horizontal and a vertical accelerometer mounted on the shake table to measure the actual acceleration time history of the shake table. In addition, there is one horizontal LVDT available that measures the horizontal movement of the shake table. The shake

table acceleration time history for cyclic load at 40g with amplitude of 1.2 V is shown in Figure 7-1. The maximum measured acceleration is about 40g. Accordingly, the shake table acceleration time history of the cyclic load at 40g with 0.9 V amplitude and at 30g with 0.9 V amplitude are shown in Figures 7-2 and 7-3; respectively. The maximum measured accelerations for the cyclic load with amplitude of 0.9 V on the shake table is about 30g at 40g centrifugal acceleration and 25g at 30g.

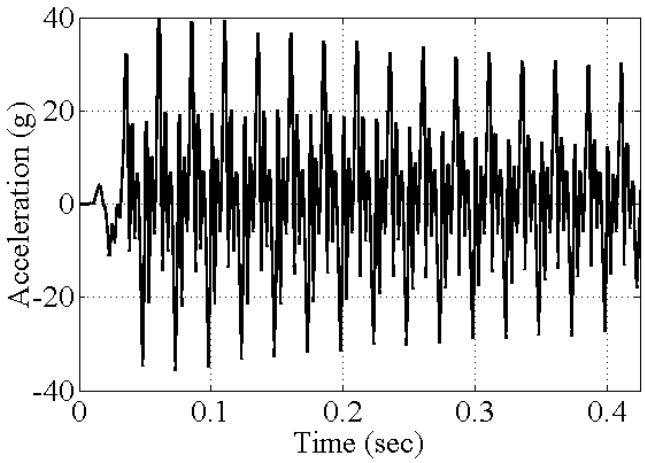

Figure 7-1. Shake table horizontal acceleration time history at 40g under 1.2 V amp cyclic loading

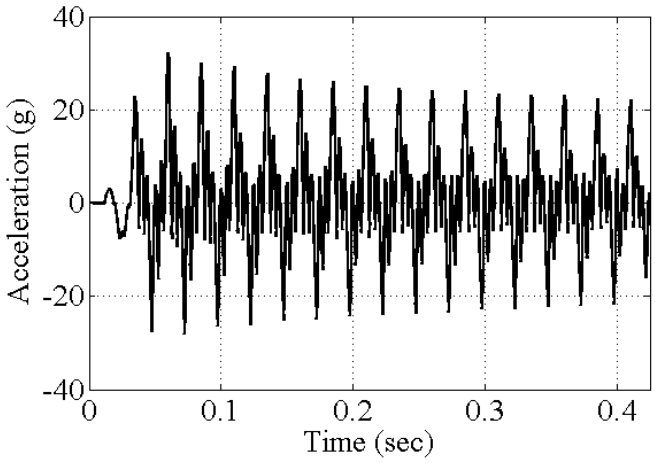

Figure 7-2. Shake table horizontal acceleration time history at 40g under 0.9 V amp cyclic loading

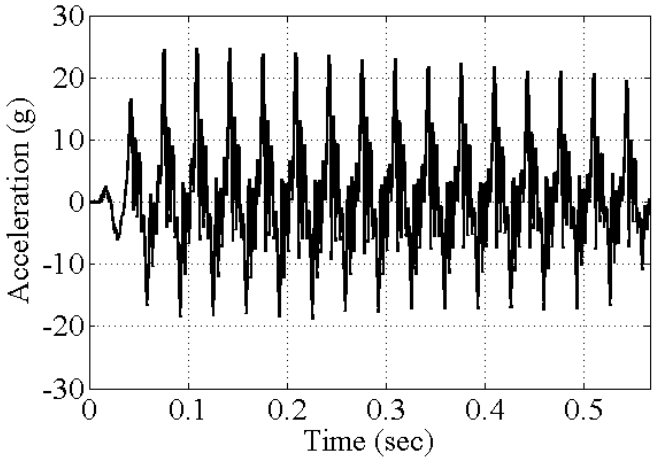

Figure 7-3. Shake table horizontal acceleration time history at 30g under 0.9 V amp cyclic loading

A typical measured displacement time history of the shake table movement using the LVDT during cyclic loading at 40g with amplitude of 1.2 V is shown in Figure 7-4. The same plot for the tests with amplitude of 0.9 V at 40g and 30g are shown in Figures 7-5 and 7-6; respectively. It should be noted that the measured amplitudes for different tests could be a little different due to the hydraulic system performance and also due to the weight of the specimen which is different in different degrees of saturation.

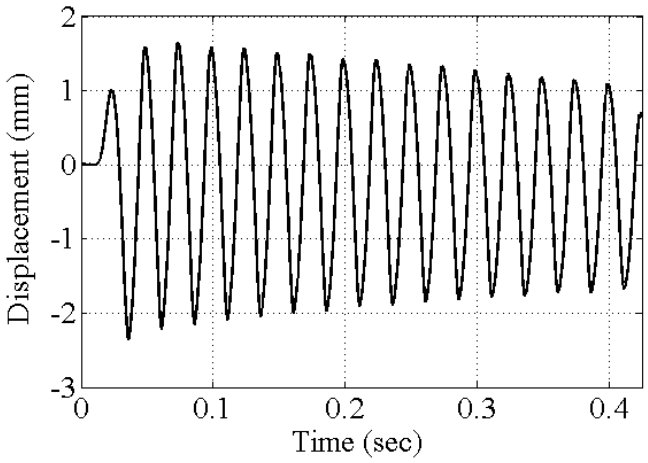

Figure 7-4. Shake table horizontal displacement time history at 40g under 1.2 V amp cyclic loading

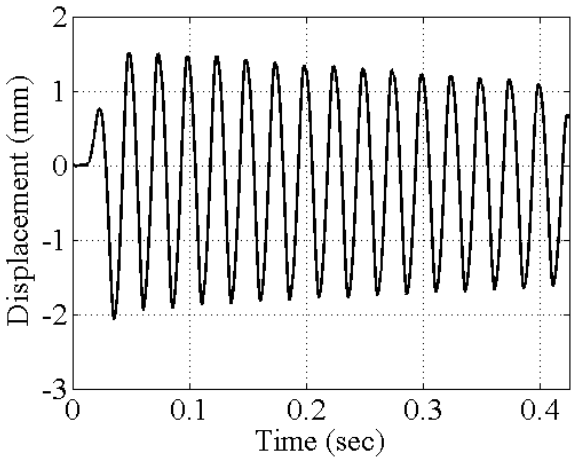

Figure 7-5. Shake table horizontal displacement time history at 40g under 0.9 V amp cyclic loading

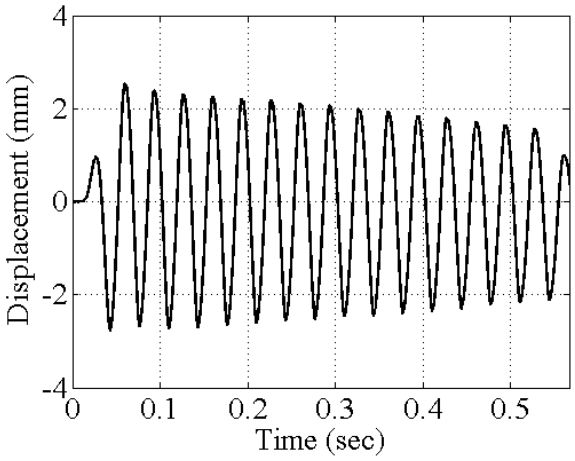

Figure 7-6. Shake table horizontal displacement time history at 30g under 0.9 V amp cyclic loading

7.2 Laminar Container Performance

Uniformity of motion at any horizontal cross section is a major criterion in evaluating the performance of the laminar container. The measured acceleration values at different lateral locations throughout the box were used to check the uniformity of motion in the container. In this criterion, the intensity of the measured acceleration time histories at different locations at a specific horizontal cross section is compared. Specifically, the root mean square of acceleration (a_{RMS}) value is used to represent the intensity of induced acceleration between pairs of accelerometers located at the same depth such as sand surface and at a depth of 7.30 cm. The value of a_{RMS} was calculated as follows.

$$a_{RMS} = \left[\frac{1}{T}\int a^2 dt\right]^{1/2} \quad (7\text{-}1)$$

where a is the measured acceleration time history, t is the time and T is the measurement time period. The values of a_{RMS} for each pair of accelerometers at the same depth for a cyclic test are plotted in Figure 7-7. The intensity of the measured acceleration is quite uniform, which indicates that the laminar container satisfies 1D shear beam behavior. The surface induced accelerations have higher intensities than the induced accelerations at a depth of 7.30 cm that is due to the wave amplification concept.

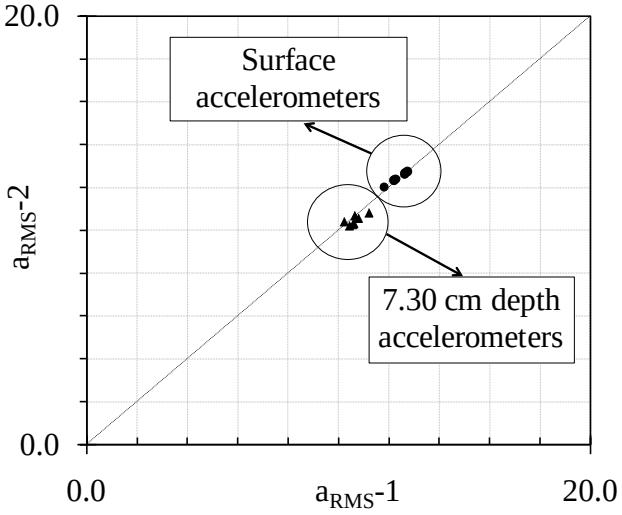

Figure 7-7. a_{RMS} value comparison for pairs of accelerometers due to the same cyclic test

7.3 Induced Acceleration Due to Cyclic Loads

As explained in Section 5-5 and shown in Figure 5-11, PCB accelerometers were used to measure the induced acceleration time history due to cyclic loads during loading at different points inside the specimen. The accelerometers were placed at three different depth including the sand surface, 7.30 cm depth and at the bottom of the specimen. The maximum induced acceleration at the surface or the peak surface acceleration (a_{PSA}) is a key parameter in estimating the seismic behavior of a sand layer, as explained in Chapter 2. According to the test schedule there were three major types of loading including the tests with amplitude of 1.2 V at 40 g, 0.9 V at 40 g, and 0.9 V at 30 g. The peak accelerations measured on the shake table are shown against

the degree of saturation in Figure 7-8. On the other hand, the cyclic amplitude has a small change in different cycles, so the a_{RMS} value was calculated to show the intensity of the acceleration time history. The a_{RMS} values of the induced acceleration time histories on the shake table for different tests are shown in Figure 7-9. The data in Figures 7-8 and 7-9 are scattered primarily due to the weight of soil layers having different degrees of saturation. This scatter can also be attributed to the hydraulic system power at the time of a particular test, because the shake table hydraulic power differs due to the difference in amount of accumulated hydraulic oil and how long the shake table was working.

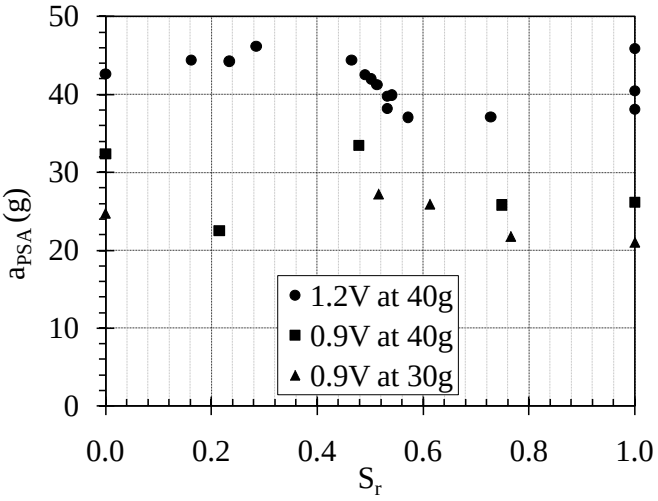

Figure 7-8. Peak acceleration measured on the shake table

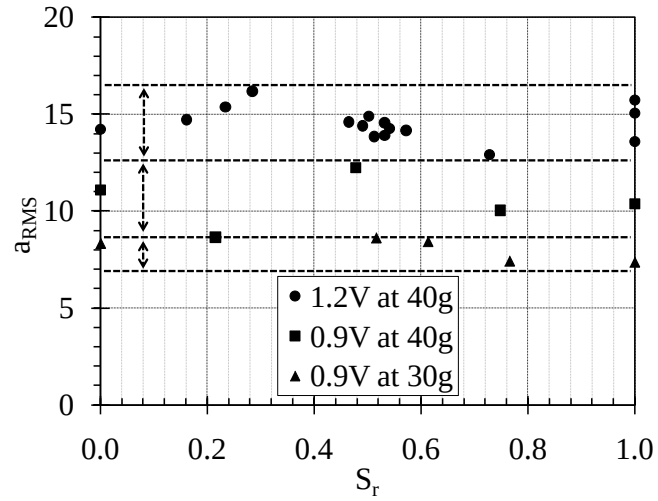

Figure 7-9. a_{RMS} value of the acceleration time history measured on the shake table

Although the measured acceleration on the shake table is important parameter, the induced acceleration inside the specimen is the key factor in empirical design approaches. The induced accelerations were measured at three different depths as the accelerometers were buried at those depths. The typical measured acceleration time histories at the sand surface under cyclic load with amplitude of 1.2V at 40g gravitational acceleration is shown if Figure 7-10. The cyclic load amplitude is about 25g and the cyclic load amplitude is quite uniform. The acceleration time history of the induced motion at the soil surface for the cyclic load with amplitude of 0.9V at 40g and 30g are shown in Figure 7-11 and 7-12; respectively.

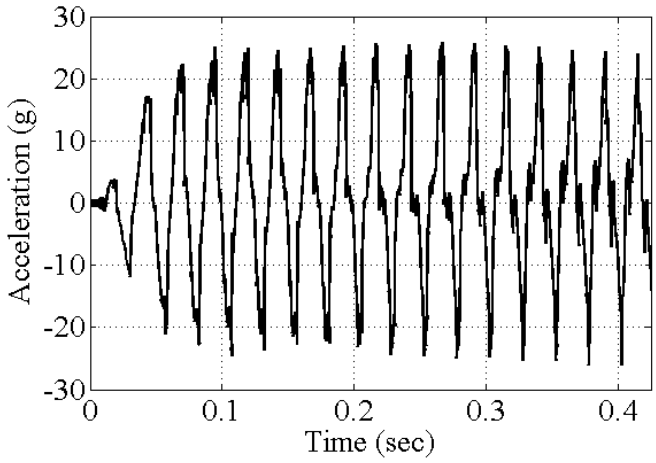

Figure 7-10.Typical induced acceleration time history at the surface under 1.2V amplitude cyclic load at 40g

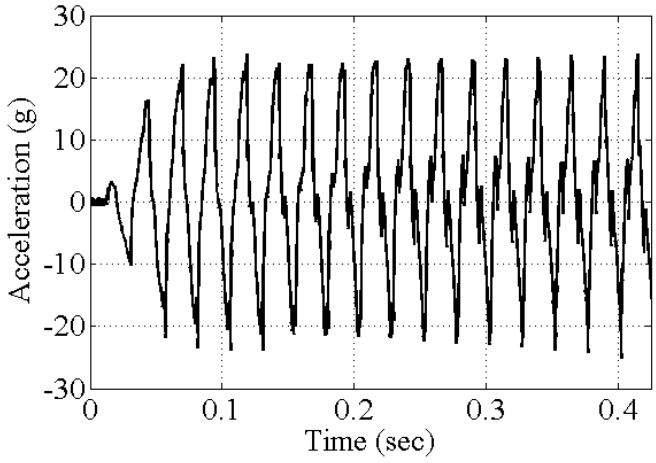

Figure 7-11.Typical induced acceleration time history at the surface under 0.9V amplitude cyclic load at 40g

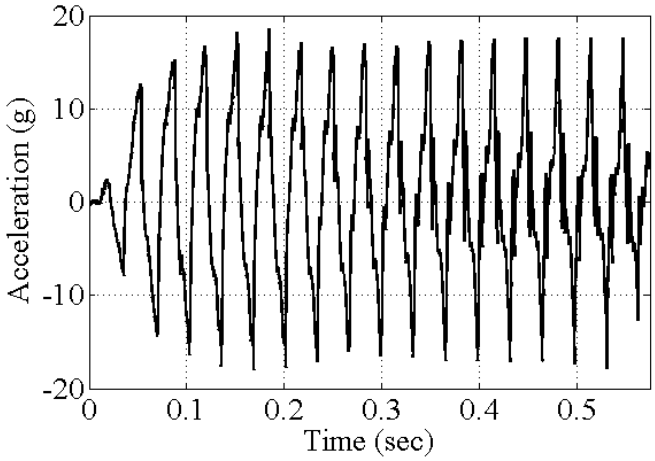

Figure 7-12. Typical induced acceleration time history at the surface under 0.9V amplitude cyclic load at 30g

The peak accelerations at different depths for the tests under cyclic load with amplitude of 1.2V at 40g with different degrees of saturation are shown in Figures 7-13. Although the data is scattered there is an overall decreasing trend in the peak acceleration by increasing the degree of saturation. The same plot is shown for the cyclic load with amplitude of 0.9V at 40 and 30g in Figures 7-14 and 7-15.

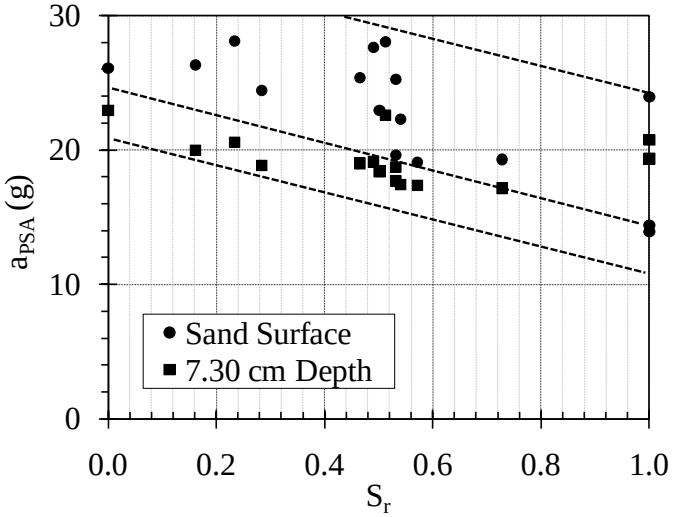

Figure 7-13. Peak induced acceleration under 1.2V amplitude cyclic load at 40g

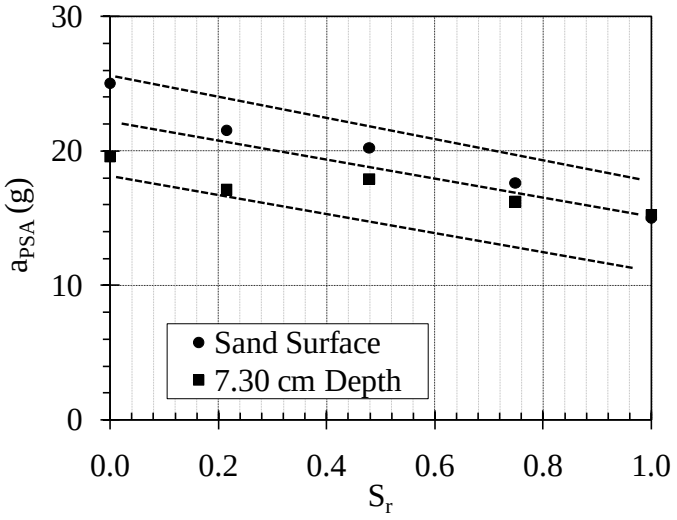

Figure 7-14. Peak induced acceleration under 0.9V amplitude cyclic load at 40g

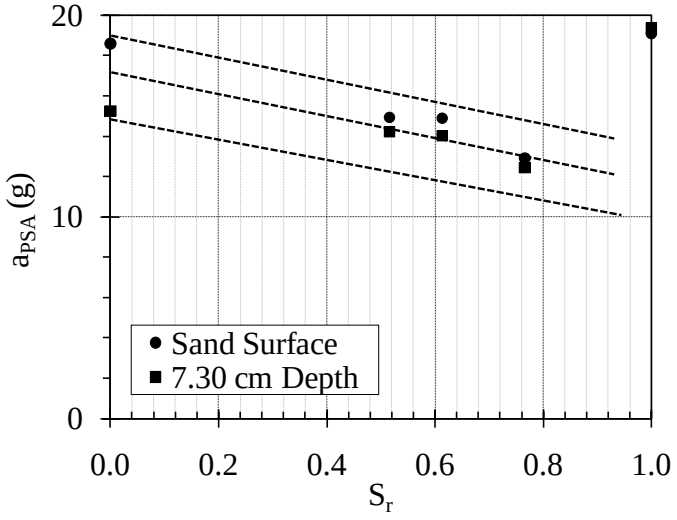

Figure 7-15. Peak induced acceleration under 0.9V amplitude cyclic load at 30g

The a_{RMS} value is a good representative of the intensity of motion. Consequently, the a_{RMS} value is calculated for the induced acceleration time histories for tests with different degrees of saturation. The a_{RMS} values of the cyclic tests with 1.2V amplitude at 40g are shown in Figure 7-16. The same decreasing trend is observed by increasing the degree of saturation. However, the data is less scattered comparing the peak acceleration results. The same plot is shown for cyclic tests with amplitude of 0.9V at 40g and 30g in Figures 7-17 and 7-18. The decreasing trend in peak acceleration and a_{RMS} values could be due to the damping of the waves

inside the specimens with higher degrees of saturation. This decreasing trend is more significant in higher g-level tests and also in higher amplitude loading condition. Also, the downward trend is less obvious in the acceleration records from the accelerometers in depth. It should be noted that still data is scattered due to scattered nature of the applied cyclic load on the shake table. The only irregular data points in these plots are the points where S_r=1.0 (fully saturated specimens). In saturated specimens the peak acceleration does not follow any trend but the a_{RMS} values still have the decreasing trend but with a significant drop in a_{RMS} values comparing to the partially-saturated specimens. This can be due to the fact that the specimen is liquefied in the tests on saturated specimens and accelerometers lose their contact with the sand particles. According to the observations above, the variation of the induced accelerations should be considered in settlement analysis later in this chapter.

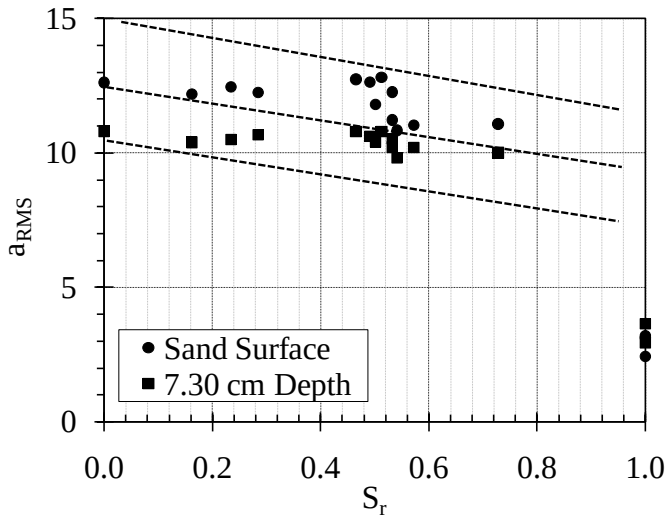

Figure 7-16. a_{RMS} value of induced acceleration time history under 1.2V amplitude cyclic load at 40g

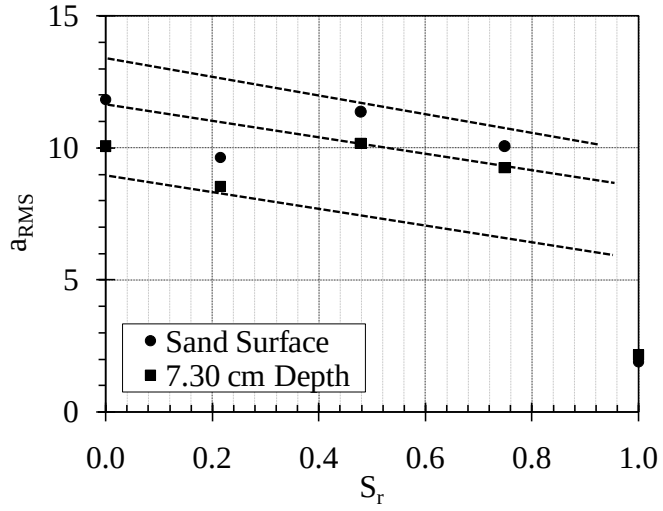

Figure 7-17. a_{RMS} value of induced acceleration time history under 0.9V amplitude cyclic load at 40g

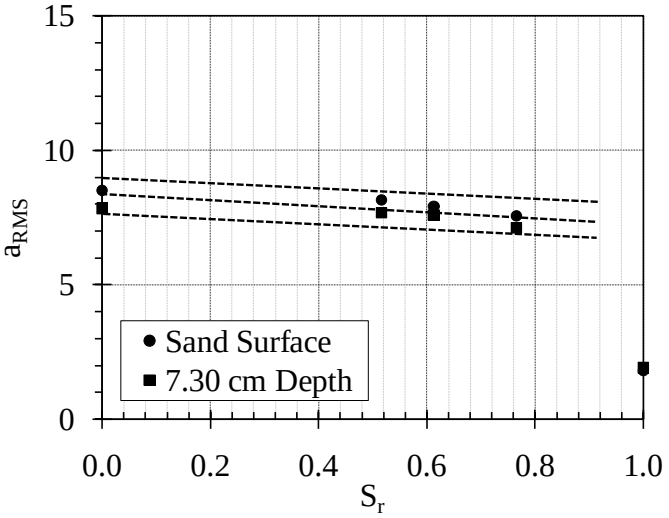

Figure 7-18. a_{RMS} value of induced acceleration time history under 0.9V amplitude cyclic load at 30g

7.4 Seismic Compression

The experimental setup incorporated three LVDTs to measure the seismic settlement during and after the loading (one at the center and two at the sides, Figure 5-11). The typical LVDT measurements under the cyclic load with amplitude of 1.2V at 40g for different range of degrees of saturation are shown in Figure 7-19 where Figure 7-19(a) is for $S_r = 0.0$, Figure 7-19 (b) is for $0.0 < S_r < 0.2$, Figure 7-19(c) is for $0.2 < S_r < 0.4$, Figure 7-19(d) is for $0.4 < S_r < 0.6$, Figure 7-19(e) is for $0.6 < S_r < 0.8$, and Figure 7-19(f) is for $S_r = 1.0$.

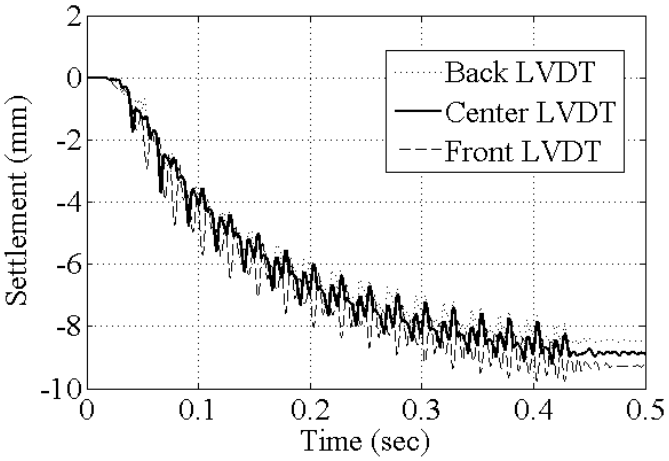
Back LVDT
Center LVDT
Front LVDT
Settlement (mm)
Time (sec)
2
0
-2
-4
-6
-8
-10
0
0.1
0.2
0.3
0.4
0.5

(a)

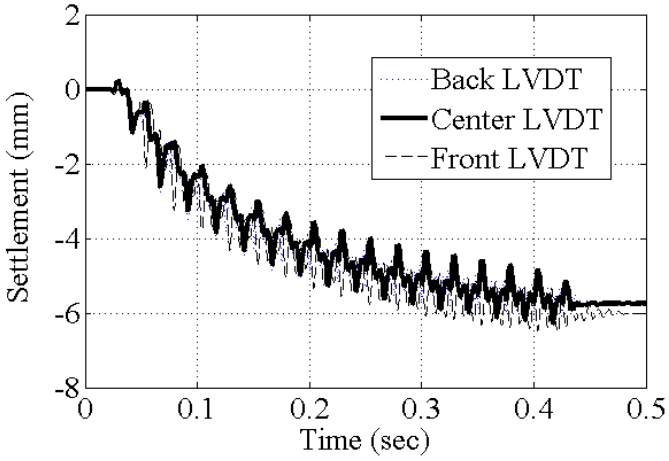
Back LVDT
Center LVDT
Front LVDT
Settlement (mm)
Time (sec)
2
0
-2
-4
-6
-8
0
0.1
0.2
0.3
0.4
0.5

(b)

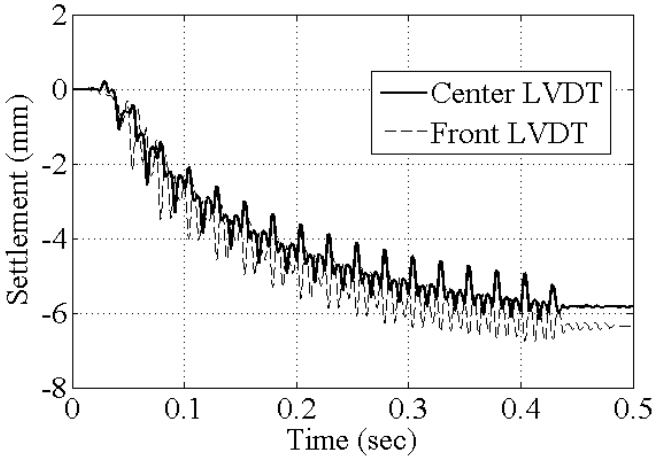
Center LVDT
Front LVDT
Settlement (mm)
Time (sec)
2
0
-2
-4
-6
-8
0
0.1
0.2
0.3
0.4
0.5

(c)

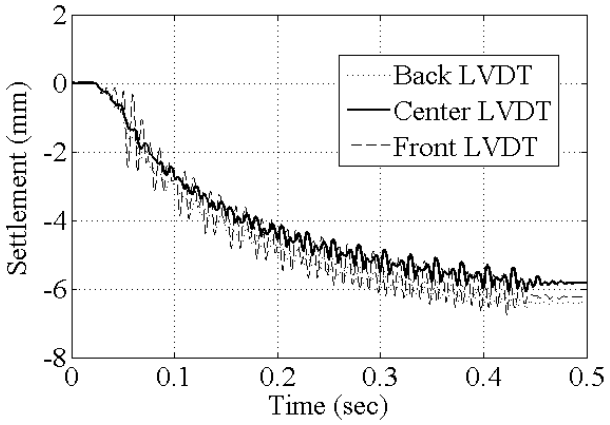

(d)

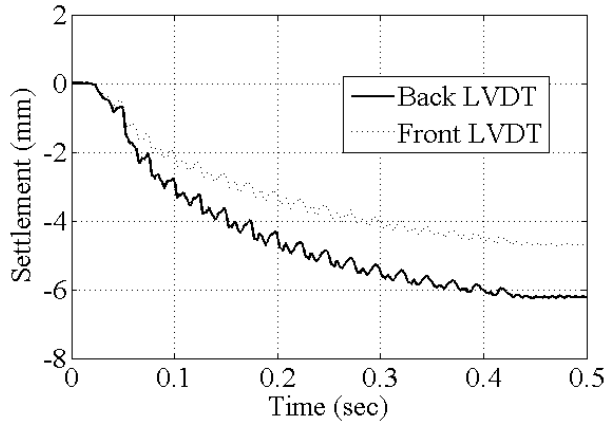

(e)

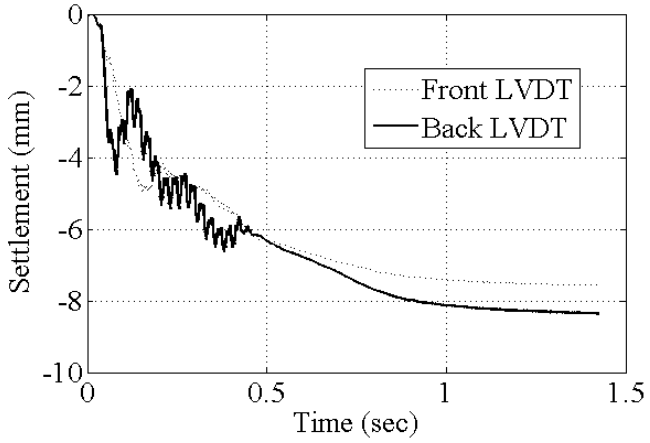

(f)

Figure 7-19. Settlement time history due to 1.2V amplitude cyclic load at 40g when: (a) $S_r = 0.0$; (b) $0.0 < S_r < 0.2$; (c) $0.2 < S_r < 0.4$; (d) $0.4 < S_r < 0.6$; (e) $0.6 < S_r < 0.8$; (f) $0.8 < S_r < 1.0$.

Considering the 17 cycles of loading (15 cycles as the main cycles and 2 low amplitude cycles to reach and stop the hydraulic power gradually) at 40Hz the loading duration was 0.425 second. According to the plots in Figure 6-19, except the case of saturated specimen, most of the settlements happen during the cyclic load which is due to compression of void space. On the other hand in saturated specimen the settlement happens during and after loading as a result of consolidation due to excess pore pressure dissipation. Although the volume change in an undrained test should be zero, there is a settlement during shaking in saturated specimen. This settlement is happening in this test because dissipation can happen during the loading where the infiltration process is still continuing and the test is not fully undrained even it is fast.

The measured settlements from the side LVDTs sometimes are higher which is related to the plastic membrane re-arrangement after the first shake. In all of the future analyses the settlement from the center LVDT is used except in a few cases where the center LVDT did not work properly or was broken. The total settlement variation for different degrees of saturation is shown in Figure 7-20 where all the settlement data due to 1.2V amplitude cyclic load at 40g are summarized. The total settlement data due to 0.9V amplitude cyclic load at 40g and 30g are shown in Figures 7-21 and 7-22, respectively.

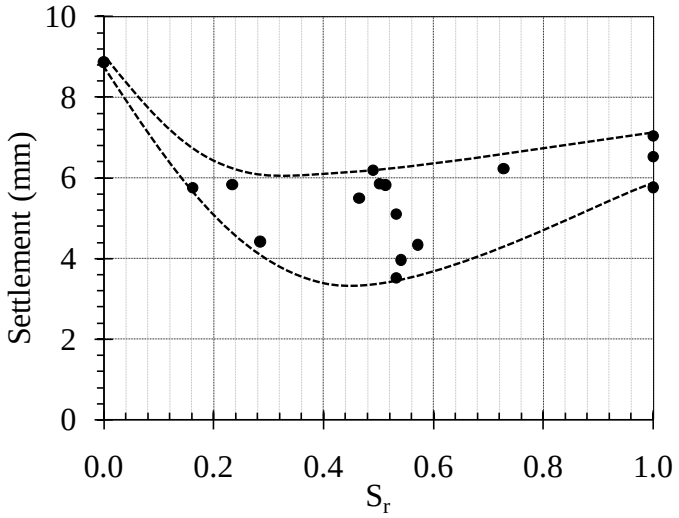

Figure 7-20. Total settlement vs. degree of saturation due to 1.2V amplitude cyclic load at 40g

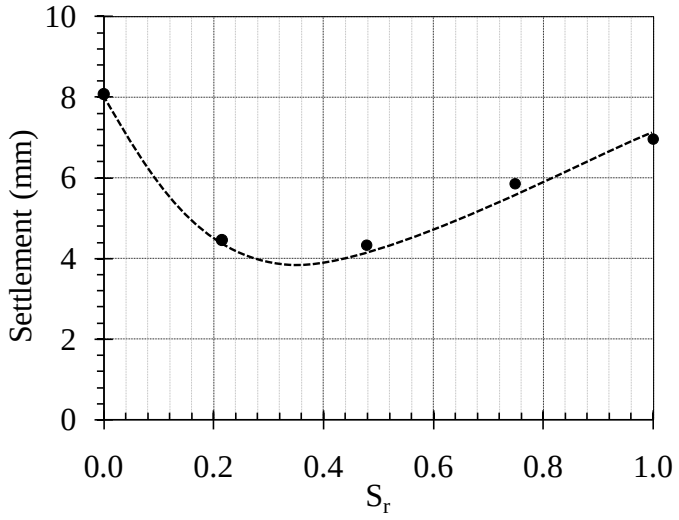

Figure 7-21. Total settlement vs. degree of saturation due to 0.9V amplitude cyclic load at 40g

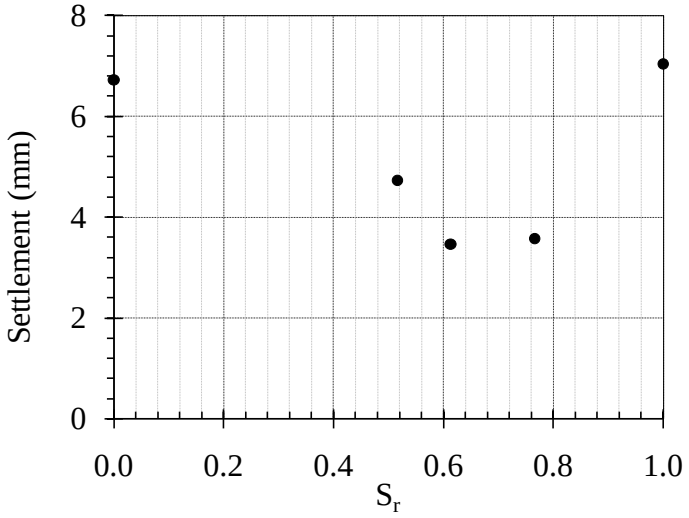

Figure 7-22. Total settlement vs. degree of saturation due to 0.9V amplitude cyclic load at 30g

According to the data shown in Figure 7-20 and 7-21, there is a nonlinear trend in the total seismically induced settlement in the sand layer by changing the degree of saturation. In all these data there is a minimum settlement at a degree of saturation of about 0.4. The scattered data in Figure 7-20 at the middle range degree of saturation is because the tests were performed at different times with different shake table hydraulic system powers and the induced accelerations were not exactly the same as shown for example in Figure 7-13. Consequently, to obtain a more meaningful set of data the settlement results should be normalized. To be able to

compare the settlements in different tests, the amount of energy applied to the specimen should be the same. The induced acceleration is decreasing in higher degree of saturation as shown in Figure 7-13. Although the raw settlement data needs to be processed, by changing the saturation condition from dry to saturated specimen the settlement first decreases until it reaches a minimum value and then increases. The minimum settlements seem to be occurred around a degree of saturation in the range of 0.3 to 0.5.

Since the induced acceleration is the key parameter varying throughout the test program, it is appropriate to normalize the settlements based on the induced acceleration. Different values can be chosen to represent the induced acceleration time history including the peak surface acceleration, peak acceleration in depth, a_{RMS} value of the surface acceleration time history, and a_{RMS} value of the acceleration time history at depth. In this study the first and third values were selected as the bases for normalization. For this purpose, all the settlement values were multiplied by a non-dimensional normalization factor based on a_{PSA} and a_{RMS}. These factors are the ratio of the peak surface accelerations or the a_{RMS} values of the acceleration time histories for each test over the same value in the dry test. The normalized settlement obtained using the following equations:

$$a_{PSA}\ Normalized\ Settlement = Settlement * \frac{a_{PSA-dry}}{a_{PSA}} \tag{7-2}$$

$$a_{RMS}\ Normalized\ Settlement = Settlement * \frac{a_{RMS-dry}}{a_{RMS}} \tag{7-3}$$

The measured settlements for the specimens tested under the 1.2V amplitude cyclic load at 40g, normalized based on the a_{PSA} (peak surface acceleration), are shown in Figure 7-23. It should be noted that the a_{PSA} in cyclic test is very close to average cyclic acceleration and ideally should be equal. The normalization was performed so that all the settlements were due to the same a_{PSA} as dry test, in this case 26.1g.

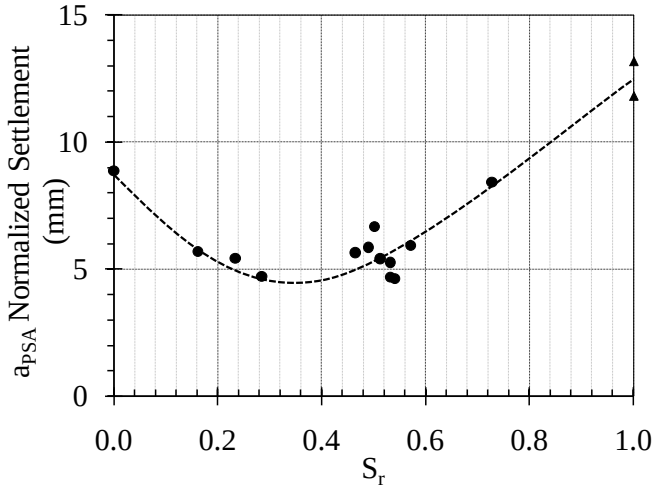

Figure 7-23. a_{PSA} normalized total settlement vs. degree of saturation due to 1.2V amplitude cyclic load at 40g

The nonlinear trend in settlement is a much clearer in figure 7-23 comparing Figure 7-20, where there is a minimum settlement at a degree of saturation of about 0.4. In order to confirm the normalization concept another set of tests were performed with completely the same condition except the cyclic amplitude. Consequently, the measured settlement data due a 0.9V amplitude cyclic load at 40g shown in Figure 7-21 were also normalized with the same method as described above and plotted together with the last set of results as shown in Figure 7-24. The same trend observed in Figure 7-23 can be seen in Figure 7-24 where the approximation line kept constant to show the similarity of the results.

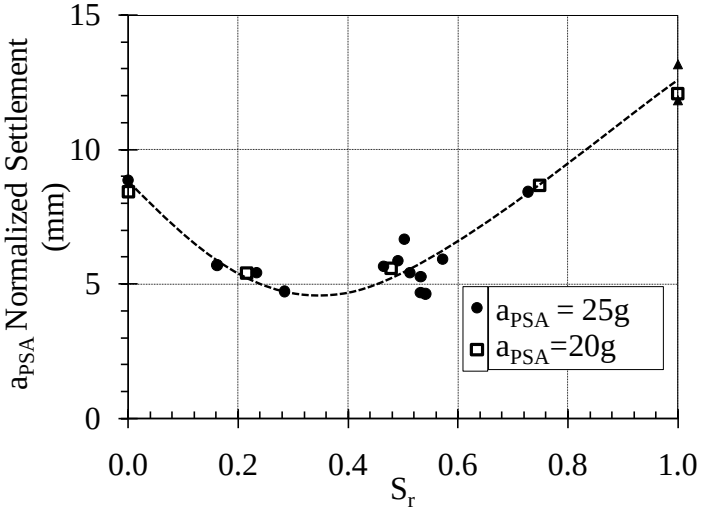

Figure 7-24. a_{PSA} normalized total settlement vs. degree of saturation due to cyclic load at 40g

As discussed earlier in this chapter, a_{RMS} value is also a good representative of the intensity of the acceleration time history. Consequently, settlements measured due to cyclic loading shown in Figures 7-20 and 7-21 were normalized using the value of a_{RMS} from the induced acceleration time history at the sand surface and are shown in Figure 7-25. The value of a_{RMS} represents the intensity of motion in a more meaningful way than a_{PSA} because the full time history is considered in the value of a_{RMS} while only the peak is incorporated into the value of a_{PSA}.

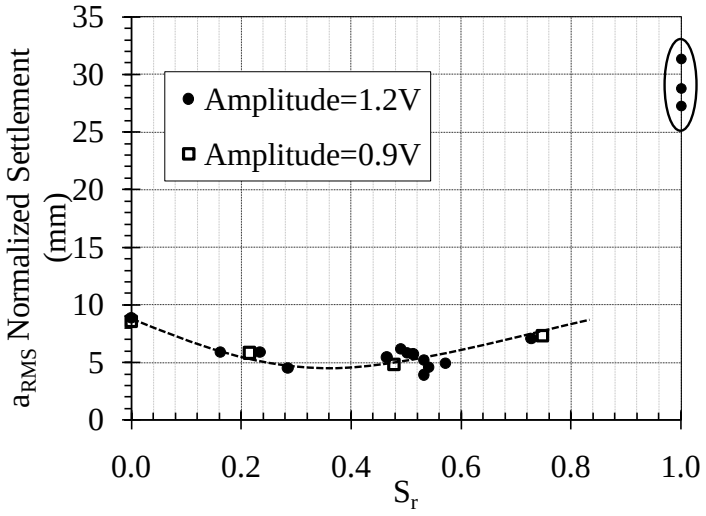

Figure 7-25. a_{RMS} normalized total settlement vs. degree of saturation due to cyclic load at 40g

As in Figure 7-25, normalization based on a_{RMS} provides a clear trend similar to normalization based on a_{PSA}. The only problem with a_{RMS} modification is in saturated condition, where sand was liquefied after the first cycle and the accelerometers lost contact with sand particles and were floating in water. Consequently, the measured accelerations have very small amplitudes after the first peak as shown in Figure 7-26. Since there is low amplitude of acceleration time history in the results obtained from the tests on the saturated specimens the a_{RMS} value will be low too. This low a_{RMS} results in a very high normalized settlement value. The results of normalized settlement based on a_{RMS} are shown together with the a_{PSA}-base normalized data for saturated specimens in Figure 7-27. It is obvious that the normalization

based on a_{RMS} is not suitable for the tests on the saturated specimens. The a_{RMS}-base normalized settlement results obtained from the test performed at 30g under 0.9V amplitude cyclic load is shown in Figure 7-28 showing the same trend as the tests at 40g. Accordingly, the same behavior in the tests on saturated specimens is notified.

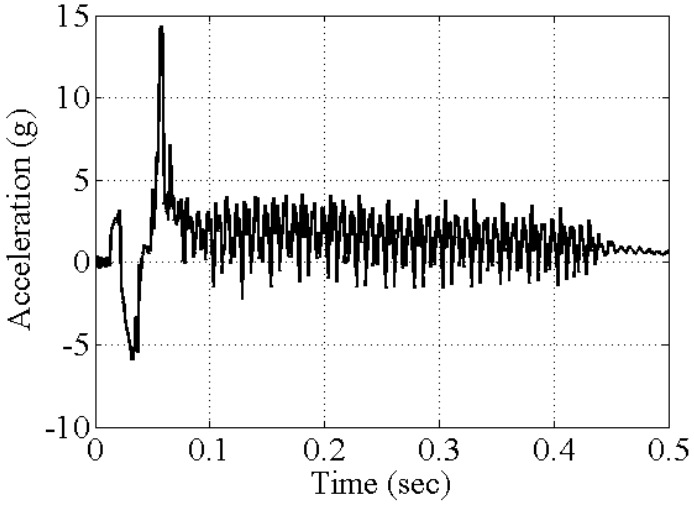

Figure 7-26. Typical induced acceleration time history at the surface of a saturated specimen under 1.2V amplitude cyclic load at 40g

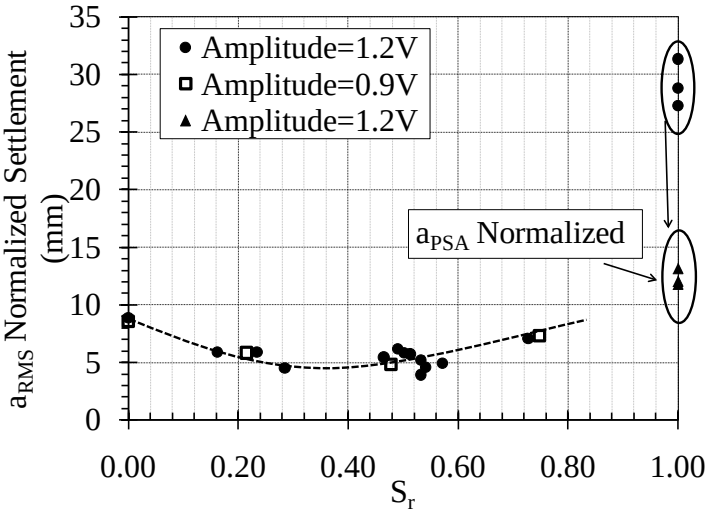

Figure 7-27. a_{RMS} Normalized total settlement vs. degree of saturation due to cyclic load at 40g

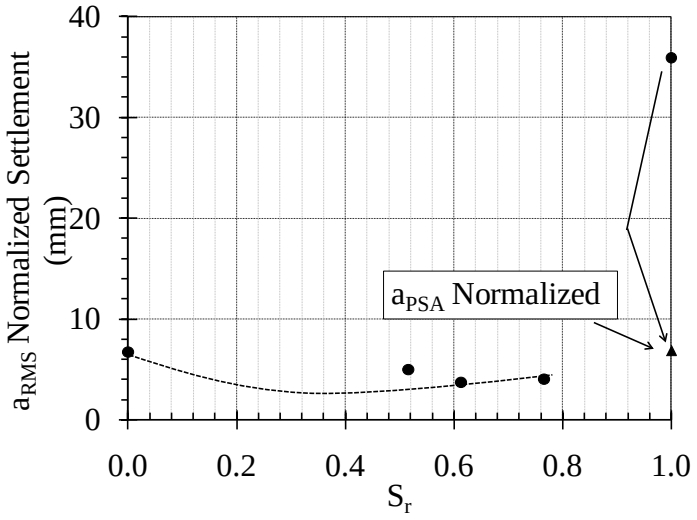

Figure 7-28. a_{RMS} Normalized total settlement vs. degree of saturation cyclic load at 30g

7.5 Pore Water Pressure Generation

As explained in previous chapters, one source of seismically induced settlement in a layer of sand is due to the consolidation resulting from dissipation of excess pore water pressure. When an earthquake happens or the geotechnical structure subjected to dynamic loads there will be a raise in pore water pressure. In a fully undrained manner, there will be no drainage during the test. If the specimen is saturated there is no volume change until the shaking stops. Then, the excess pore water pressure starts to drain and sand particles will slip on each other causing volume change and further settlement in the sand layer. Consequently, previous researchers tried to correlate the amount of pore pressure generated due to loading and the volume change due to dissipation of pore water pressure. In actual field cases and in these physical modeling tests the system is not fully undrained so there will be settlements during and after loading.

The pore pressure time history was recorded by placing the pore pressure transducers inside the soil layer as shown in Figure 7-11. The pore pressure variation due to loading and after cyclic loading measured at depths of 5.08 and 12.7cm in the saturated specimen under 1.2V amplitude cyclic load at 40g, 0.9V amplitude cyclic load at 40g and 0.9V amplitude cyclic load at 30g; are shown in Figures 7-29, 7-30 and 7-31; respectively. The pore pressure increases

during the loading and then it dissipates afterwards. The r_u value ($r_u=\Delta u/\sigma'_0$) is a common parameter to evaluate the pore pressure variation and is shown on each plot. ru value is lower in the deeper PPT than the shallower PPT, but almost in all cases sand was liquefied. By comparing Figure 7-29 and 7-30, it can be found that the higher amplitude cyclic loading generates more excess pore water pressure (u_{excess}) which leads to higher ru value.

The change in location of PPTs (and other sensors) during shaking in most tests was minor, except in the case of the saturated specimen, which liquefied. In the case of liquefied saturated sand, the excess pore pressure exceeds the initial effective stress [Figure 7-29 to 7-31] which could only have occurred if the PPT changed in position during liquefaction. Similar behavior was reported by Fiegel and Kutter (1994).

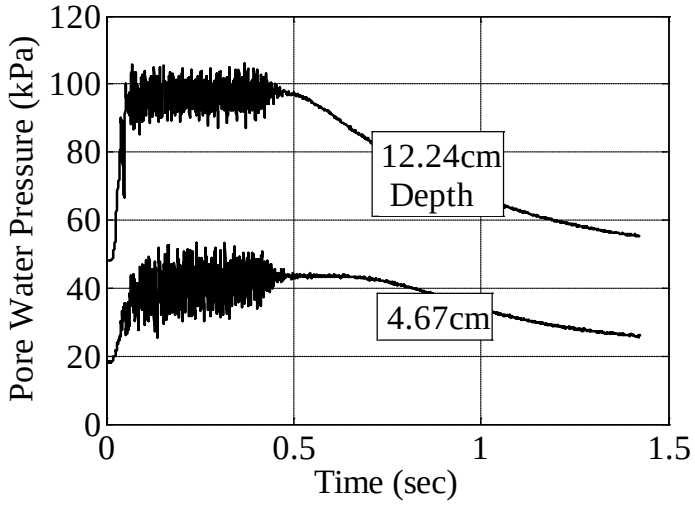

Figure 7-29. Pore Water Pressure time history in a saturated specimen due to 1.2V cyclic load at 40g

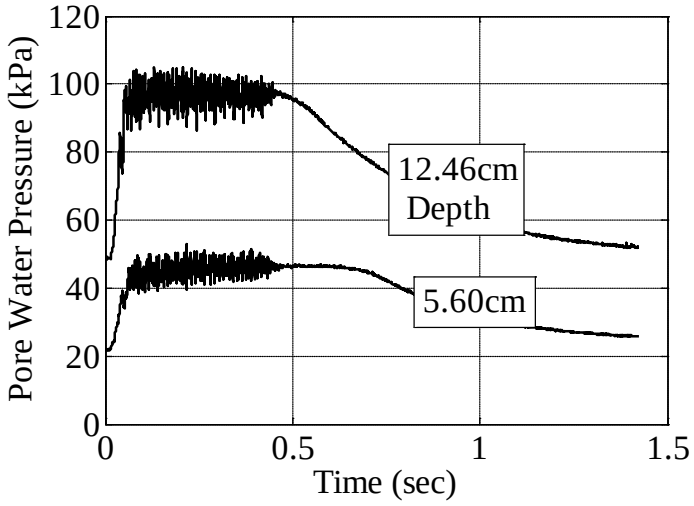

Figure 7-30. Pore Water Pressure time history in a saturated specimen due to 0.9V cyclic load at 40g

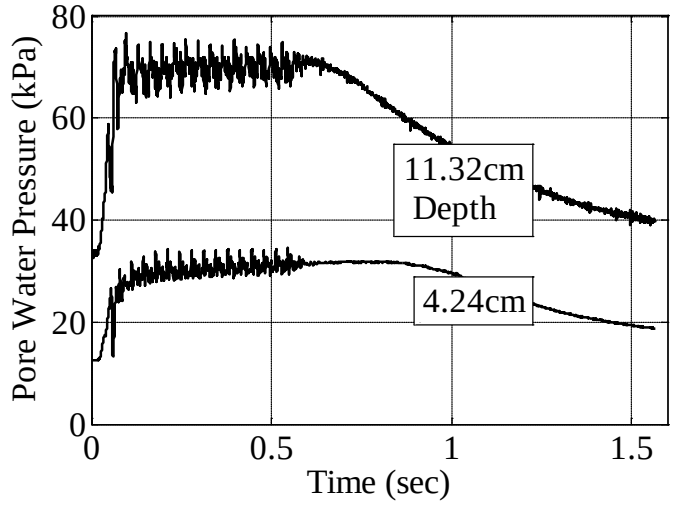

Figure 7-31. Pore Water Pressure time history in a saturated specimen due to 0.9V cyclic load at 30g

The degree of saturation may have a significant impact on deformation response of a soil layer during cyclic loading. If the degree of saturation is very close to 1.0, then there will be some pore pressure generation but much lower than the saturated condition. Accordingly, the volume change due to pore pressure dissipation in partially saturated specimen would be lower than the saturated specimen. On the other hand, for lower values of degree of saturation, the initial pore pressure is negative. In this case, cyclic loading will result in compression of air voids, which will result in an increase in degree of saturation.

The Druck PDCR 81 sensors were found to provide a reliable measurement of the relatively low magnitudes of matric suction encountered in this study (<15 kPa). The only concern is that the porous stone at the tip of the PPTs should remain saturated while the sand layer is partially saturation. Although the air-entry suction of the PPTs is relatively high, the PPTs only functioned as expected in a few tests. Typical changes in pore water pressure at depths of 8.89 and 12.7 cm in a sand layer having an initial degree of saturation of 0.49 and 0.50 are shown in Figures 7-32 and 7-33, respectively. In this test, the pore water pressure increases and approaches zero. Since the infiltration process is continuous during a cyclic loading event, the specimen rapidly returns to a uniform suction profile after cyclic loading. The suction decreased after cyclic loading because seismic compression occurred, which resulted in a decrease in void ratio. A lower change in suction was observed at the elevation of the lower PPT, likely because of the lower confining pressure and corresponding lower seismic compression.

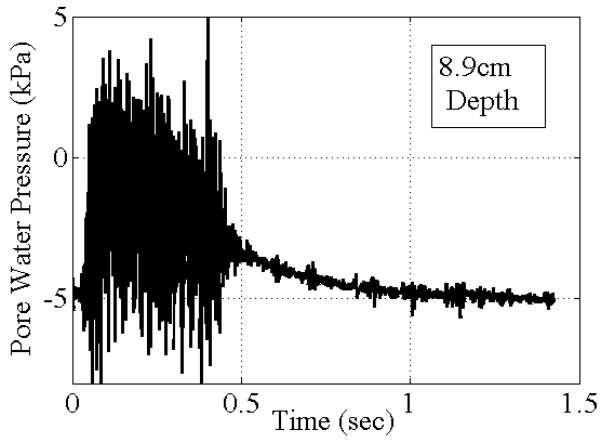

Figure 7-32. PWP time history in a partially-saturated specimen due to 1.2V amplitude cyclic load at 40g at a depth of 8.9 cm

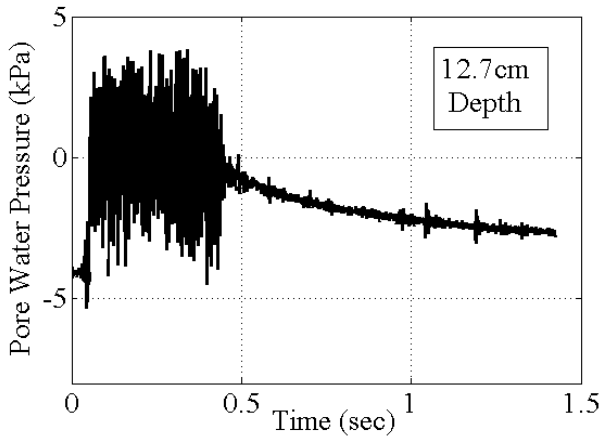

Figure 7-33. PWP time history in a partially-saturated specimen due to 1.2V cyclic load at 40g at a depth of 12.7 cm

7.6 Cyclic Test with Metolose as an Alternate Pore Fluid

As discussed in Chapter 2.7, there are different scaling relations for time when evaluating the effects of seepage and generation/dissipation of pore water pressures due to dynamic loading. Since both of these mechanisms occur during cyclic loading of partially-saturated sand models, time scaling is an important issue when extrapolating measurements to prototype conditions. Although tests were also performed in this investigation using a more viscous pore fluid (metolose), the majority of the tests were performed with water. Water was used because of the ease of controlling the infiltration process and because it permitted straightforward use of the dielectric sensors for volumetric water content measurement. This is not ideal to evaluate the dissipation of pore water pressures generated from earthquake shaking due to the time scaling conflict in centrifuge modeling between diffusive fluid flow and dynamic loading. Arulanandan et al. (1983) and Dief and Figueroa (2003) indicate that the viscosity of the pore fluid primarily mainly the dissipation of pore pressure after shaking. They observed that the magnitude of excess pore pressure was not affected by the viscosity of pore fluid, but that water pressure drops faster than that for a more viscous pore fluid. Accordingly, if a more viscous pore fluid had been used in this study, its major effect would be on the rate of the settlement due to dissipation of pore water pressure instead of the total settlement after shaking. An exception to this situation is the case where partial drainage occurs during shaking, which can lead to some settlement

during the shaking event (Dashti et al. 2010). The magnitude of partial drainage depends on the hydraulic conductivity of the soil layer. The use of a more viscous pore fluid will decrease the hydraulic conductivity and slow down drainage during shaking and result in lower settlements during shaking related to pore water pressure dissipation. However, the pore water pressure measurements in this study indicate that only partial drainage during shaking occurred in soils which are saturated or close to saturation.

A Metolose solution with a concentration of 1.8% by weight (i.e., weight of the Metolose powder to weight of the water) was prepared and used to saturate the specimen. According to Dewoolkar et al. (1999), a Metolose solution with 1.8% concentration has a viscosity which is 40 times more than that of water but with the same density and shear strength. Consequently, this solution is appropriate as a pore fluid in centrifuge physical modeling tests at 40g.

After saturating the specimen (due to low permeability the saturation process took a long time) and spinning up the centrifuge a cyclic load with amplitude of 1.2 V was applied to the specimen at 40g. The measured settlement for the saturated specimen with Metolose and the results obtained from the tests with water as the pore fluid are shown together in Figure 7-34. The seismic settlement of the layer of the sand which had been saturated with Metolose is lower than the value of the layer of the sand saturated with water under the same cyclic loading conditions. The lower settlement confirms the partial drainage concept during shaking which is slower when Metolose was used as pore fluid. The slower drainage leads to smaller settlement during shaking. The rest of drainage happened after the shaking stopped and causes further settlement. However, using more viscous pore fluid affects only the rate of settlement after shaking and not the amount of settlement. A new nonlinear trend line is added to the plot in Figure 7-34 that shows the possible settlement of the sand layer if the scaling conflict didn’t exist. Although the settlement values are changed, the nonlinear trend with minimum settlement at the degree of saturation of about 0.4 remains the same.

On the other hand, when a Metolose-saturated soil layer is subjected to cyclic load

there is a longer time required for dissipation of the excess pore water pressure generated by the cyclic loading (because the permeability of sand to Metolose is lower than the permeability of sand to water). Time histories of the excess pore water pressures generated at two depths in a sand layer are shown in Figure 7-35. Unfortunately, because of the limitations on the duration of high-speed data recording possible with the data acquisition system, dissipation of excess pore water pressures was not measured by the time the recording of data stopped.

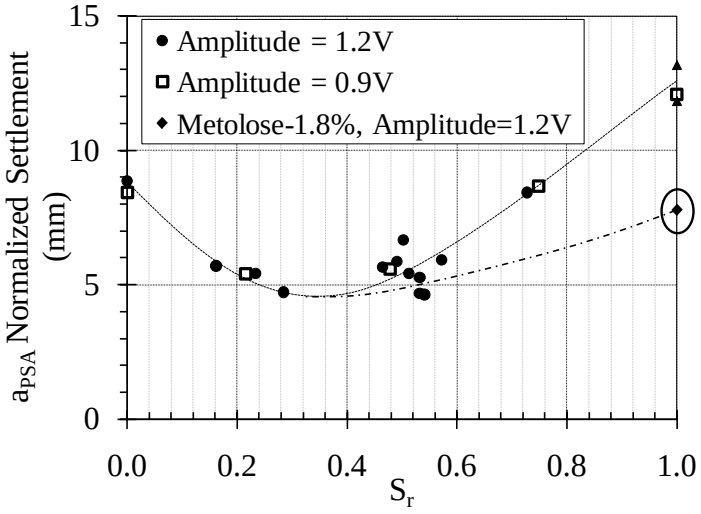

Figure 7-34. a_{PSA} normalized settlement of the sand layer with water and Metolose as the pore fluid

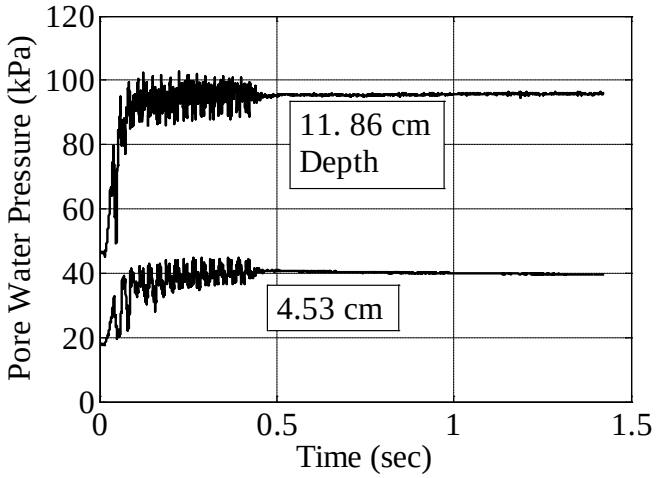

Figure 7-35. Pore pressure time history due to 1.2V cyclic load at 40g for a Metolose-saturated specimen

7.6 Model Validation

Comparison of the seismic settlement results from the prediction methodology and

centrifuge physical modeling indicates that there is a similarity in the general trend of the settlement of the partially saturated sand layer. The differences can be attributed to the uncertainty in material parameters and empirical equation which needs further investigation. However, the similarity in general trend confirms the significance of difference in seismically induced settlement of partially-saturated sand comparing with the case of dry or saturated sand.

The predicted range and measured settlements are shown in Figures 7-14 (a) and (b). The experimental results presented in Figure 7-14(b) are obtained by multiplying the model settlements shown in Figure 4-34 to the centrifuge scaling factor for length (n=40). The comparison indicates that the measured experimental settlements in are in the range of predicted settlements depending on selection of input parameters. However, the imaginary line for the settlement of the specimens with Metolose as pore fluid is in more agreement with the predicted results.

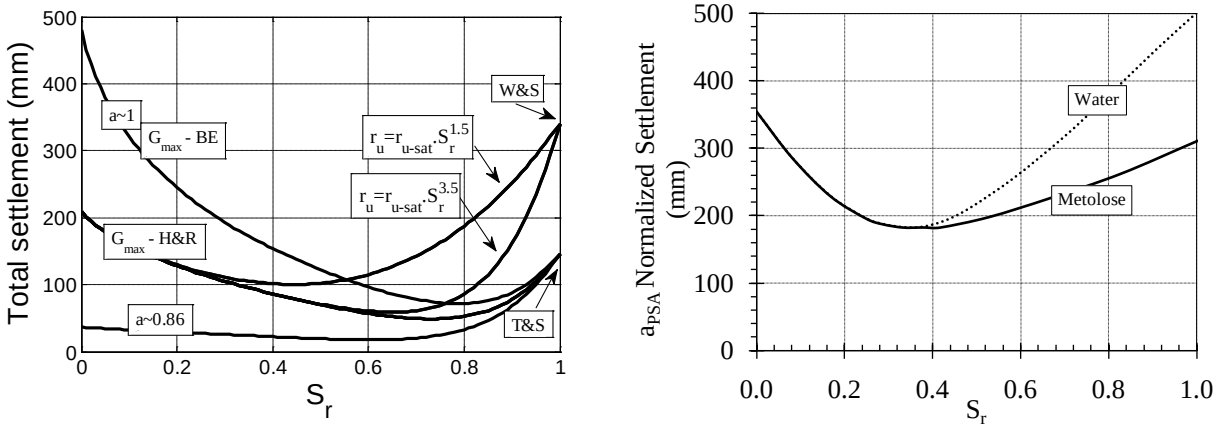

Figure 7-36. (a) The range of predicted settlements, (b) Scaled settlements of the sand layer due to cyclic loading

CHAPTER VIII

SUMMARY, CONCLUSIONS, AND RECOMMENDATIONS

8.1 Summary

The goals of this study was to characterize the mechanisms of seismically induced settlement of partially-saturated sand, and to evaluate the suitability of an empirical design methodology to predict the amount of settlement in free-field soil layers during earthquake or cyclic loading. The objectives of this study stated above were achieved as follows:

- The soil water retention curve (SWRC) of the F-75 Ottawa sand was obtained by performing a hanging column test.
- A resonant column test apparatus was modified by incorporating the hanging column technique for partially-saturated sand testing. The effect of matric suction on small-strain shear modulus was evaluated using the modified resonant column test results.
- An empirical methodology framework was developed to predict the earthquake induced settlements of partially-saturated sands. This methodology incorporates the effective stress concept in partially-saturated sand while it is consistent with conventional methods. The settlement obtained in this methodology is due to two different sources including: (1) settlement due to compression of void space; (2) settlement due to consolidation associated with the dissipation of excess pore water pressure.
- Steady-state infiltration technique was adopted to reach uniform suction and degree of saturation profile through the soil depth. A laminar container was modified to allow for the flow of water through the layer of sand. Steady state infiltration was found to lead to a constant degree of saturation in the soil profile. This technique facilitates performing

any pulse-wave testing, cyclic testing, or earthquake evaluation for a layer of the sand inside the laminar container atop shake table with partially-saturated condition in geotechnical centrifuge.

- A bender element testing approach was implemented to assess G_{max} of the soil in centrifuge physical modeling. Using three pairs of bender elements mounted on two pedestals facilitated the evaluation of the G_{max} of partially-saturated sand at different depth of a layer of sand during infiltration. The effective stress dependent shear modulus function was obtained for partially-saturated sand by considering the single parameter effective stress concept. The estimated effective stress dependent shear modulus equation was compared with empirical methods for dry sands and with resonant column test results.
- A new testing approach was developed to test the seismic compression of partially-saturated sand. Cyclic loading was applied to sand layers having different degrees of saturation at 40g and 30g and the surface settlement was measured using three LVDTs. Acceleration time histories were measured using accelerometers which were buried inside the sand layer and also mounted on the shake table. The measured settlements were normalized based on surface induced acceleration and compared for different degrees of saturation. The cyclic tests with lower amplitude were performed to confirm the normalization idea. A few cyclic tests were performed at 30g and similar trend was observed in the settlement data. Pore water pressure time histories were measured during and after cyclic loading and the PWP generation and dissipation due to loading were tracked. However, The PPTs didn't perform well for partially-saturated specimens. Cyclic tests on Metolose-saturated specimens were also performed to investigate the effect of viscosity difference of pore fluid in the seismic behavior of the layer of sand.
- The advantages and disadvantages of the developed methodology were discussed and its results were compared by experimental data. The possible ways to improve the prediction methodology were pointed out.

8.2 Conclusions

The following specific conclusions were drawn from the results in this study:

- Although F-75 Ottawa sand is uniformly graded sand, it has enough fine particles to hold suction values up to 10 kPa.
- A nonlinear trend was observed in the predicted settlement using the developed empirical methodology, where the settlement due to compression of void space decreases by increasing the degree of saturation whiles the settlement due to consolidation increases.
- Steady state infiltration was found to be a useful approach to reach a uniform degree of saturation profile through the sand depth. Experimental water contents measured in the sand profile confirmed the theoretical prediction of steady state flow in unsaturated sand during centrifugation.
- The bender element testing technique was found appropriate for in-flight measurement of G_{max} and during infiltration. Specifically, the values of G_{max} measured using bender elements matched well with those from resonant column tests. In both sets of tests, a maximum G_{max} value was observed at a degree of saturation of about 0.4.
- This observation confirms the presence of minimum settlement at a middle range degree of saturation under cyclic loading.
- Arrival time measurement was found to be a key issue in evaluation of the shear wave velocity of the partially saturated sand layers. Comparing the empirical equations for G_{max} and the calculated values based on the two arrival time estimation methods, FDM and CCM methods, indicates that FDM method leads to a better estimation of G_{max} while CCM-based method underestimate the G_{max} value.
- A single parameter approach was used to estimate the effective stress of partially-saturated sand. The mean effective stress dependent G_{max} curve was plotted for dry, saturated and partially-saturated specimens and it was observed that a single equation may be used to predict the value of G_{max} of this particular sand for different degrees of saturation. The

data points followed the best fitted curve and generally fell within a tolerance of ±10%.

- A nonlinear trend was observed in the settlement of partially-saturated sand layer due to cyclic loading where the layer of sand with a uniform degree of saturation of about 0.4 had the minimum settlement due to the same cyclic load.
- The lower settlement in partially-saturated sands in comparison to those observed in dry or saturated sands is in accordance with higher shear modulus trend.
- Pore water pressure was observed to increase during shaking in the saturated sand layers due to cyclic loads and caused liquefaction in the specimen. On the other hand, suction in partially-saturated sand was observed to decrease. However, there was not enough quality data to evaluate the PWP response for different degrees of saturation.
- Metolose-saturated sand layers were observed to settle less than water-saturated specimen, while the excess pore pressure was dissipated slower than in water saturated specimen. This difference in pore pressure response mainly affected the settlements of the specimens with degree of saturations more than 0.4.
- The predicted and measured settlements followed the same general nonlinear trend with a minimum settlement at a middle range degree of saturation. However, the settlement values and the degree of saturation with the minimum settlement are different. This difference could be due to uncertainty in material parameters, lack of fully developed relations for volumetric strain of partially-saturated specimens, and time scaling effect in centrifuge modeling where the Metolose-saturated test had a lower settlement than water saturated test.

8.3 Recommendations

A recommendation for future research would be to improve the relations used to estimate the material parameters and the empirical equations used in the empirical methodology. Performing element scale cyclic test including torsional shear test, cyclic triaxial test, and cyclic simple shear with the capability of suction control would be a major contribution to this

methodology. Use of these tests permits soil-specific definition of the shear modulus reduction function for unsaturated conditions, pore pressure response of the partially-saturated sand under cyclic loading, and seismic compression of partially-saturated sand element during and after loading. All of these values are important input parameters for the empirical methodology for seismic settlement.

The database developed in this study may be extended in the future by performing tests on partially saturated sand layers using earthquake acceleration time histories. In that case, the measured settlement can be compared with the available field data from an actual earthquake. The reversals and duration of earthquake shaking may lead to different trends than those noted in this study. One improvement in instrumentation in the physical modeling would be to improve PPT's capability for suction measurement in fast dynamic loading. In addition the seismic response of the sand with Metolose as the substitute pore fluid could be further investigated. However, an increase in pore fluid viscosity will lead to a lower permeability of the soil layer, which may inhibit the use of steady-state infiltration to control the suction profile. Accordingly, the effect of viscosity of pore fluid on settlement of a layer of sand is a subject which can be studied further as long as a uniform suction profile is achievable through the sand depth.

The seismic compression of soil layers under a footing load rather than in a free-field case is an interesting subject for future research. Steady state infiltration can still be used to provide a partially-saturated sand profile under a footing load at the sand surface. The bender element testing technique during infiltration could be a powerful tool to assess the changes in the G_{max} profile in the sand layer with and without presence of the footing load.

REFERENCES

Alramahi, B., Alshibli, K.A., Fratta, D., and Trautwein, S. 2007. “A Suction-Control Apparatus for the Measurement of P and S-wave Velocity in Soils.” Geotechnical Testing Journal, 31(1), 1-12.

Altun S. and Goktepe A.B., 2006, “Cyclic stress strain behavior of partially saturated soils”, Proc. Unsaturated soils 2006, Carefree, Arizona, 497-507.

Andrus, R.D. and Stokoe II, K.H. 2000. “Liquefaction Resistance of Soils from Shear Wave Velocity.” Journal of Geotechnical and Geoenvironmental Engineering. ASCE. 126(11), 1015-1025.

Argawal, T. K. and Ishibashi, I. 1991. “Multi-Directional Wave Velocity by Piezoelectric Crystals,” Proceedings, Recent Advances in Instrumentation, Data Acquisition and Testing in Soil Dynamics, Orlando, FL, Bhatia and Blaney, Eds., ASCE. 102–117.

Arulanandan, K., Anandarajah, A., and Abghari, A. 1983. “Centrifugal Modeling of Soil Liquefaction Susceptibility.” Journal of Geotechnical Engineering, 109(3), 281-300.

Arulnathan, R., Boulanger, R.W., and Riemer, R.F. 1998. “Analysis of Bender Element Tests”, Geotechnical Testing Journal, 21(2), 120-131.

Bates, C.R. 1989. “Dynamic Soil Property Measurements during Triaxial Testing.” Geotechnique, 39(4), 721–726.

Bishop A.W., 1959, “The principle of effective stress”, Tek. Ukeblad, 106(39), 859-863.

Blewett, J., Blewett, I.J., and Woodward, P.K. 2000. “Phase and Amplitude Responses Associated with the Measurements of Shear Wave Velocity in Sand by Bender Elements.” Canadian Geotechnical Journal. 37, 1348–1357.

Brandenberg, S.J., Choi, S., Kutter, B.L., Wilson, D.W., and Santamarina, J.C. 2006. “A Bender Element System for Measuring Shear Wave Velocities in Centrifuge Models.” Proc. Int.

Conf. Physical Modelling in Geotechnics, Hong Kong. Nov.

Brignoli, E. G. M., Gotti, M., and Stokoe II, K. H. 1996. “Measurement of Shear Waves in Laboratory Specimens by Means of Piezoelectric Transducers.” Geotechnical Testing Journal, 19(4), 384–397.

Cabarkapa, Z., Cuccovillo, T. and Gunn, M. 1999. “Some aspects of the pre-failure behaviour of unsaturated soil.” Proc. of the Second International Conference on Pre-failure Deformation Characteristics of Geomaterials, Torino, Italy, Sept. 27–29.

Cetin, K.O., Bilge, H.T., Wu, J., Kammerer, A.M., and Seed, R.B. “Probabilistic Model for the Assessment of Cyclically Induced Reconsolidation (Volumetric) Settlements.” Journal of Geotechnical and Geoenvironmental Engineering, 135(3), 387-398.

Chaney R.C., 1978, “Saturation effects on the cyclic strength of sands”, Proc., ASCE Special Conference on Earthquake Engineering and Soil Dynamics, New York, 342-359.

Chipley M.T., 1996, “Centrifuge modeling of flow processes”, Ph.D. thesis, Department of Civil, Environmental, and Architectural Engineering, University of Colorado, Boulder.

D’Appolonia E., 1968, “Dynamic loadings”, State-of-the-Art Report, Presented at the Aug.68 ASCE Specialty Conference held at Cambridge, MA.

Dashti, S., Bray, J.D., Pestana, J.M., Riemer, M. and Wilson, D. 2010. “Mechanisms of Seismically Induced Settlement of Buildings with Shallow Foundations on Liquefiable Soil.” Journal of Geotechnical and Geoenvironmental Engineering, 136(1), 151-164.

Darendeli M.B. and Stokoe K.H. 2001. Development of a new family of normalized modulus reduction and material damping curves, University of Texas, Geotechnical Engineering Report GD01-1.

Dell’Avanzi, E., Zornberg, J.G., and Cabral, A.R. 2004. “Suction Profiles and Scale Factors for Unsaturated Flow under Increased Gravitational Field.” Soils and Foundations, 44(3), 79-90.

Dewoolkar M.M., Ko H.Y., Stadler A.T. and Astaneh S.M.F., 1999, “A substitute pore fluid for seismic Centrifuge Modeling”, Geotechnical Testing Journal, Vol. 22, No. 3, 196-210.

Dief, H.M. and Figueroa, J.L. 2003. “Shake Table Calibration and Specimen Preparation for Liquefaction Studies in the Centrifuge.” ASTM Geotechnical Testing Journal, 26(4), 402-409.

Duku, P.M., Stewart J.P., Whang, D.H., and Yee, E. 2008. “Volumetric Strains of Clean Sands Subject to Cyclic Loads.” Journal of Geotechnical and Geoenvironmental Engineering, 134(8), 1073-1085.

Dyvik, R. and Madshus, C. 1985. “Lab Measurements of Gmax using Bender Elements”, Norwegian Geotechnical Institute Publication, No. 161, Oslo.

Fiegel, G.L. and Kutter, B.L. 1994. “Liquefaction Mechanisms for Layered Soils.” Journal of Geotechnical Engineering, 120(4), 737-755.

Finn W.D.L. and Byrne P.M., 1976, “Estimating settlements in dry sand during earthquakes”, Canadian Geotechnical Journal, 13, 355-363.

Gardner W., 1956, “Calculation of capillary conductivity from pressure plate outflow data”, SSSA, 20, 317-320.

Greenin, P.D. and Nash, D.F.T. 2004. “Frequency Domain Determination of G0 using Bender Elements.” Geotechnical Testing Journal, 27(3), 288-294.

Hardcastle J.H. and Sharma S., 1998, “Shear modulus and damping of unsaturated loess”, Proc. of Third Conference of Geotechnical Earthquake Engineering and Soil Dynamics, Seattle, WA, 178-188.

Hardin, B.O., Richart, F.E. 1963. “Elastic Wave Velocities in Granular Soils.” J. Soil Mech. Found. Div. Proc. ASCE 89, No.SM1, 33–65.

Hardin, B.O. and Black, W.L. 1969. “Vibration modulus of normally consolidated clay; closure.” Journal of the Soil Mechanics and Foundations Division. ASCE. Vol. 95, No. SM6, 1531–1537.

Hardin, B.O., Drnevich, V.P. 1972. “Shear Modulus and Damping in Soils: Design Equations and Curves.”, J. Soil Mech. Found. Div. Proc. ASCE 98, No. SM7, 667–692.

Hardin, B.O. 1978. “The nature of stress-strain behavior of soils.”, Proceedings, Earthquake Engineering and Soil Dynamics, ASCE Pasadena, California, 1(3-89).

Heidari, M. and James, R.G. 1982. “Centrifugal Modeling of Earthquake Induced Liquefaction in a Column of Sand.”, Proceedings of the Conference on Soil Dynamics and Earthquake Engineering, Vol. 1, Southampton, England, 271-281.

Hoyos, L.R., Takkabutr, P., Puppala, A.J., and Hossain, M.D.S. 2008. “Dynamic Response of Unsaturated Soils Using Resonant Column and Bender Element Testing Techniques.” Geotechnical Earthquake Engineering and Soil Dynamics IV, 1-8.

Hushmand, B., Scott, R.F., and Crouse, C.B. 1988. “Centrifuge Liquefaction Test in a Laminar Box.” Geotechnique, 38(2), 253-262.

Inci, G., Yesiller, N., and Kagawa, T. 2003. “Experimental investigation of dynamic response of compacted clayey soils.” Geotechnical Testing Journal. Vol. 26, No. 2, 125-141.

Ishibashi I. and Zhang X., 1993, “Unified dynamic shear moduli and damping ratios of sand and clay”, Soils and Foundations, Vol. 33, No. 1, 182-191.

Ismail, M.A. and Hourani, Y. 2003. An innovative facility to measure shear-wave velocity in centrifuge and 1-G models.” Proc. of Third International Symposium on Deformation Characteristics of Geomaterials. H. Di Benedetto, T. Doanh, H. Geoffroy & C. Sauzéat (eds.). Lyon, France. 22-24 Sept. 2003.

Iwasaki, T., Tatsuoka, F. and Takagi, Y. 1978. “Shear moduli of sands under cyclic torsional shear loading.” Soils Found. 18(1), 39–56.

Jitrapinate N., Sriboonlue V., Srisuk K. and Muangson N., 2006, “A method for capillary rise modeling”, Proc. Unsaturated soils 2006, Carefree, Arizona, 2535-2545.

Kawaguchi, T., Mitachi, T., and Shibuya, S. 2001. “Evaluation of Shear Wave Travel Time in Laboratory Bender Element Test,” Proceedings, Fifteenth International Conference on Soil Mechanics and Geotechnical Engineering, Istanbul, Balkema, 155–158.

Ketchum S.A., 1989, “Development of an earthquake motion simulator for centrifuge testing and the dynamic response of a model sand embankment”, PhD Dissertation, University of Colorado at Boulder, Boulder, CO.

Khalili, N. and Zargarbashi, S. (2010), “Influence of hydraulic hysteresis on effective stress in unsaturated soils”, Geotechnique, 60(9), 729-734.

Khosravi, A., Ghayoomi, M., and McCartney, J.S. (2010). “Impact of effective stress on the dynamic shear modulus of unsaturated sand.” GeoFlorida 2010, West Palm Beach, Florida, USA. Feb. 20-24. CD-ROM.

Kim, D. S., Seo, W. S. & Kim, M. J. 2003. “Deformation characteristics of soils with variations of capillary pressure and water content.” Soils and Foundations. Vol. 43, No. 4, 71–79.

Kim, N.-R., Kim, D.-S. 2010. “A Shear Wave Velocity Tomography System for Geotechnical Centrifuge Testing.” 33(6), 10 pg.

Ko H.Y., 1988a, “Summary of the state-of-art in centrifuge model testing”, Centrifuges in Soil Mechanics, Edited by Craig and Schofield, 11-18.

Ko H.Y., 1988b, “The Colorado centrifuge facility”, Centrifuge 88, Corte, Ed., Balkema, Rotterdam, 73-75.

Kokusho T., 2000, “Correlation of pore-pressure B-value with P-wave velocity and Poisson’s ratio for imperfectly saturated sand or gravel”, Soils and Foundations, 40(4), 95-102.

Kramer S.L., 1996, “Geotechnical Earthquake Engineering”, Prentice Hall, New Jersey.

Lambe, P.C., Whitman, R.V. 1982. “Scaling for Earthquake loading Tests on Centrifuge.” Proceedings of the Conference on Soil Dynamics and Earthquake Engineering, Vol. 1, Southampton, England, 91-106.

Law H.K., 1991, “An experimental study of soil-water-foundation interaction during an earthquake, PhD thesis, Department of Civil, Environmental and Architectural Engineering, The University of Colorado at Boulder, Boulder, CO.

Lee K.L. and Albaisa A., 1974, “Earthquake induced settlement in saturated sands”, ASCE, Journal of Geotechnical Engineering Div., 100(GT4), 387-405.

Lee J.-S. and Santamarina J.C. 2005. “Bender Elements: Performance and Signal Interpretation.” J. Geotechnical and Geoenvironmental Eng., 131(9), 1063-1070.

Leong, E.C., Yeo, S.H., and Rahardjo, H. 2005. “Measuring Shear Wave velocity using Bender Elements.” Geotechnical Testing Journal, 28(5), 488-498.

Lu N. and Likos W.J., 2004, “Rate of capillary rise in soil”, Journal of Geotechnical and Geo-environmental Engineering, Vol. 130, No. 6, 646-650.

Lu N. and Likos W.J., 2006, “Suction stress characteristic curve for unsaturated soil”, Journal of Geotechnical and Geo-environmental Engineering, Vol. 132, No. 2, 131-142.

Lu, N., Godt, J.W., and Wu, D.T. 2010. “A Closed Form Equation for Effective Stress in Unsaturated Soil.” Water Resources Research, 46, W05515, 14pp.

Mancuso, C., Vassallo, R., and d’Onofrio, A. (2002). “Small Strain Behavior of a Silty Sand in Controlled-Suction Resonant Column-Torsional Shear Tests.” Canadian Geotechnical Journal. CGJ. Vol. 39, No. 1, 22-31.

Marinho, E.A.M., Chandler, R.J., and Crilly, M.S. 1995. “Stiffness Measurements on an Unsaturated High Plasticity Clay using Bender Elements.” Proc. of the First International Conference on Unsaturated Soils, UNSAT ’95, Paris, France, 6– 8 September 1995. A.A. Balkema, Rotterdam, the Netherlands. Vol. 2. 535–539.

Martin G.R., Finn W.D.L. and Seed H.B., 1975, “Fundamentals of liquefaction under cyclic loading”, Journal of Geotechnical Engineering Devision, ASCE, Vol. 101, No. GT5, Proc. Paper 11284, May, 423-438.

Mendoza, C.E., Colmenares, J.E., and Merchan, V.E. (2005). “Stiffness of an Unsaturated Compacted Clayey Soil at Very Small Strains.” Conf. on Advanced Experimental Unsaturated Soil Mechanics. Trento, Italy. 27-29 June. 199-204.

McCartney J.S., Villar L.F.S. and Zornberg J.G., 2008, “Nonwoven Geotextile as Hydraulic Barriers for Capillary flow”, The first Pan American Geosynthetics Conference & Exhibition, Cancun, Mexico.

McCartney, J.S. and Zornberg, J.G. 2010. “Centrifuge Permeameter for Unsaturated Soils. II: Measurement of the Hydraulic Characteristics of an Unsaturated Clay.” Journal of Geotechnical and Geoenvironmental Engineering, 136(8), 1064-1076.

Menq, F.-Y., 2003. “Dynamic Properties of Sandy and Gravelly Soils”, PhD Thesis, The University of Texas at Austin.

Metolose Brochure, Shin-Etsu Chemical Co., Ltd., 1997, Cellulose Dept., Othemachi 2-chome, Chiyoda-ku, Tokyo, Japan.

Michaels P., 2006, “Comparison of viscous damping in unsaturated soils, compression and shear”, Proc. Unsaturated soils 2006, Carefree, Arizona, 565-576.

Mulilis J.P., Horz R.C. and Townsend F.C., 1976, “The effects of cyclic triaxial testing techniques on the liquefaction behavior of Monterey No. 0 sand”, Misc., Paper S-76-6, Soils and Pavements Laboratory, U.S. Army Engineer Waterways Experiment Station.

Nagase H. and Ishihara K., 1988, “Liquefaction-induced compaction and settlement of sand during earthquakes”, Soils and Foundations, Vol. 28, No.1, 65-67.

Ng, C.W.W., Xu, J. and Yung, S.Y. 2009. “Effects of imbibition-drainage and stress ratio on anisotropic stiffness of an unsaturated soil at very small strains.” Canadian Geotechnical Journal, Vol. 46, No. 9, 1062-1076.

Ng. C.W.W. and Yung S.Y. 2008. “Determination of the Anisotropic Shear Stiffness of an Unsaturated Decomposed Soil.” Geotechnique. 58(1), 23-35.

Okamura M. and Teraoka T., 2006, “Seismic performance of desaturated soil as a liquefaction countermeasure”, 6th ICMPG, Hong Kong, 469-474.

Pennington, D.S., Nash, D.F.T., and Lings, M.L. 2001. “Horizontally Mounted Bender Elements for Measuring Anistropic Shear Moduli in Triaxial Clay Specimens.” ASTM Geotechnical Testing Journal. 24(2), 133–144.

Pradel D., 1998, “Procedure to evaluate earthquake-induced settlements in dry sandy soils”, Journal of Geotechnical and Geo-environmental Engineering, Vol. 124, No. 4, 364-368.

Pyke R., Seed H.B. and Chan C.K., 1975, “Settlement of sands under multidirectional shaking”, ASCE, Journal of Geotechnical Engineering Div., 101(GT4), 379-397.

Qian X., Gray D. and Woods R., 1993, “Modulus of unsaturated sands”, Journal of

Geotechnical Engineering, Vol. 119, No. 2, 295-314.

Rammah, K.I., Ismail, M.A., and Fahey, M. 2006. “Development of a Centrifuge Seismic Tomography System at UWA.” 6th International Conference on Physical Modeling in Geotechnics. Ng, Zhang and Wang (eds.). pg. 229-234.

Rezzoug A., Konig D. and Triantafyllidis T., 2004, “Scaling laws for centrifuge modeling of capillary rise in sandy soils”, Journal of Geotechnical and Geo-environmental Engineering, Vol. 130, No. 6, 615-620.

Rocker K.J., 1968, “The liquefaction behavior of sands subjected to cyclic loading”, Soils Publication No. 221, MIT.

Sawangsuriya, A., Edil, T.B., and Bosscher, P.J., and Wang, X. 2009. “Modulus-suction-water relationship for compacted soils in postcompaction state.” Journal of Geotechnical and Geoenvironmental Engineering ASCE. Vol. 135, No. 10, 1390-1403.

Schubert, H. (1975). “Tensile strength of agglomerates.” Powder Technologies. 11, 107–119.

Seed, H.B. and Lee, K.L. 1965. “Studies of liquefaction of sands under cyclic loading conditions.”, Report TE-65-65, Department of Civil Engineering, University of California, Berkeley.

Seed, H.B. and Idriss I.M. 1970. “Soil Moduli and Damping Factors for Dynamic Response Analyses.” Rep. No. EERC70-10. Earthquake Eng. Res. Ctr., Univ. of California, Berkeley, Calif.

Seed, H.B. and Idriss, I.M. 1971. “Simplified procedure for evaluating soil liquefaction potential.” J. Soil Mechanics Found. Div., ASCE, 97(9), 1249-1274.

Seed H.B. and Silver M.L., 1972, “Settlement of dry sands during earthquakes”, Journal of Geotechnical Engineering Div., ASCE, Vol. 98, No.4, 381-397.

Seed H.B., Tokimatsu K. and Harder L., 1984, “The influence of SPT procedures in evaluating soil liquefaction resistance”, Report No. UCB/EERC-84-15, Earthquake Engrg. Res. Ctr., Univ. of California, Berkeley, Calif.

Seed, R.B., Cetin, K.O., Moss, R.E.S., Kammerer, A.M., Wu, J., Pestana, J.M., and Riemer, M.F. 2001. Recent advances in soil liquefaction engineering and seismic site response evaluation, Proc. 4th Int. Conf. on Recent Advances in Geotech. Eqk. Engrg. Soil Dyn., Paper No. SPL-2.

Shirley, D.J. and Hampton, L.D. (1978). “Shear Wave Measurements in Laboratory Sediments.” Journal of the Acoustical Society of America, 63(2), 607-613.

Silver M.L. and Seed H.B., 1971, “Volume changes in sands during cyclic loading”, Journal of Soil Mechanics and Foundation Div., ASCE, Vol.97, No. SM9, 1171-1182.

Stewart, J.P. and Whang, D.H. 2003. “Simplified Procedure to Estimate Ground Settlement from Seismic Compression in Compacted Soils.” Proceedings of 2003 Pacific Conference on Earthquake Engineering, New Zealand Society for Earthquake engineering, Paper No. 046.

Stokoe, K. H., A. Kutulus, and F-Y. Menq [2004]. SASW measurements at the NEES Garner Valley test site, California, University of Texas at Austin, College of Engineering Data Report.

Terzaghi K., 1943, “Theoretical soil Mechanics”, John Wiley & Sons Inc., New York, NY.

Tokimatsu K. and Seed H.B., 1987, “Evaluation of settlements in sands due to earthquake shaking”, Journal of Geotechnical Engineering Div., ASCE, Vol. 113, No.8, 861-878.

Tokimatsu and Yoshimi (1983), "Empirical correlation of soil liquefaction based on SPT N-value and fines content." Soils and Foundations, Vol. 23, No. 4, pp. 56-74.

Tsukamoto Y., Ishihara K., Nakazawa H., Kamada K. and Huang Y., 2002, “Resistance of partly saturated sand to liquefaction with reference to longitudinal and shear wave velocities”, Soils and Foundations, Vol. 42, No. 6, 93-104.

van Genuchten, M. 1980. A Closed Form Equation for Predicting the Hydraulic Conductivity of Unsaturated Soils.” Soil Sci. Soc. Am. J., 58, 647-652.

Vassallo R., Mancuso, C. and Vinale, F. 2007. “Effects of net stress and suction history on the small strain stiffness of a compacted clayey silt.” Canadian Geotechnical Journal, Vol. 44, No. 4, 447-462.

Viggiani, G. and Atkinson, J. H. 1995. “Interpretation of Bender Element Tests.” Geotechnique. 45(1), 149–154.

Vincens E., Labbe P. and Cambou B., 2003, “Simplified estimation of seismically induced settlements”, Int. Journal for Numerical and Analytical Methods in Geomechanics, 27, 669-683.

Yegian M.K., E. Eseller-Bayat, Alshawabkeh A. and Ali S., 2007, “Induced-partial saturation for liquefaction mitigation : Experimental Investigation”, Journal of Geotechnical and Geo-environmental Engineering, Vol. 133, No. 4, 372-380.

Yoshimi Y., Tanaka K. and Tokimatsu K, 1989, “Liquefaction resistance of a partially saturated sand”, Soils and Foundation, Vol. 29, No. 3, 157-162.

Youd T.L., 1970, “Densification and shear of sand during vibration”, Journal of the Soil

Mechanics and Foundations Div., ASCE, Vol. 96, No. SM3, Proc. Paper 7272, May, 863-880.

Weissman, K. 1989. “Centrifugal Modeling of Dynamic Soil-Structure Interaction.”, Ph.D. Dissertation, Princeton University, Princeton, NJ.

Whitman R.V., Lambe P.C. and Kutter B.L., 1981, “Initial results from a stacked ring apparatus for simulation of a soil profile”, Proc. of Intl. Conf. on Recent Advance in Geotech. Earthquake Engrg. and Soil Dynamics, UMR-Rolla, MO, 1105-1110.

Whitman, R.V. and Lambe, P.C. 1986. “Effect of Boundary Conditions Upon Centrifuge Experiments Using Ground Motion Simulation.” Geotechnical Testing Journal, 9(2), 61-71.

Whitman, R.V. and Lambe, P.C. 1988. “Earthquake Like Shaking of a Structure Founded on Saturated Sand.” Centrifuge 88, Paris, 529-538.

Wu, J., and Seed, R. B. 2004. “Estimating of liquefaction-induced ground settlement (case studies).” Proc., 5th Int. Conf. on Case Histories in Geotechnical Engineering, Paper 3.09, New York.

Zornberg, J.G. and McCartney, J.S. 2010. “Centrifuge Permeameter for Unsaturated Soils. I: Theoretical Basis and Experimental Developments.” Journal of Geotechnical and Geo-environmental Engineering, 136(8), 1051-1063.

APPENDIX A

```
            %%%USS (Unsaturated Seismic Settlement)%%%
%% This is a settlement predictor code written by Majid Ghayoomi
% at the University of Colorado at Boulder
% All rights are reserved for the author
% Started on 12/04/09
% last updated 02/10/11
% Units are according to SI system (kg, m, sec)
close all
clc
clear all
% --------------------------------------------------------------------------
%% --------------------------------------------------------------------------
%    ----- Soil Profile and Centrifuge Dimensional Characteristics -----
% Height of the model soil specimen
H_model = 6.25*2.54/100;
% Distance of the center of the specimen from the centrifuge platform
D_center_p = 11*2.54/100 + H_model/2;
% Centrifuge arm length
ArmCent = 18*12*2.54/100;
% Spinning g-level at the platform
g_spin = 42.8;
% Centrifugal g-level at the center of the specimen
g_cen = g_spin*(ArmCent-D_center_p)/ArmCent;
% Prototype Height
H = H_model*g_cen;
% number of numerical subdivision
n_div = 50;
% --------------------------------------------------------------------------
%% --------------------------------------------------------------------------
%                  --- Sand Physical Characteristics ----
SandType = ' F-75 Ottawa Sand ';
Gs = 2.65; % Specific Gravity
Phi=35; % degree % from Schmertmann, 1978 from Bardet's book
%                 for Dr=45-50% uniform fine sand
nou=0.25;   % Poisson's ratio
K_0=1-sin(pi*Phi/180);  % coefficient of earth pressure at rest
ro_d_max = 1781 ;
ro_d_min = 1469 ;
e_max = 0.8039;
```

```
e_min = 0.4879;
% Preparation Density
Dr_init = 0.45;
ro_init_d = ro_d_min + Dr_init*(ro_d_max-ro_d_min);
e_init = e_max - Dr_init*(e_max-e_min);
n_init=e_init/(1+e_init);
Cu = 1.71; % Uniformity Coeeficient
% fluid density
ro_water = 1000; %kg/cm3
K_w=2200000000; %Pa
% Assumed there is a Uniform Degree of Saturation through the depth
% -------------------------------------------------------------------------
%% -------------------------------------------------------------------------
%       --- Earthquake or sesimc load in prototype scale---
loadtype = 'cyclic';
% maximum acceleration (g)
a_max = 0.65; %a_max/g
g = 9.81 ;% m/(s^2)
% number of cycles
n_cycle = 15;
% frequency (Hz)
freq = 1 ;
% Earthquake magnitude vs cyclic load characteristics
M_quake = 7;
if loadtype == 'cyclic'
    a_ave = a_max;
    M_quake = n_cycle^(1/2.17)+4;
elseif loadtype == 'earthquake'
    a_ave = 0.65* a_max;
    n_cycle = (M_quake-4)^2.17;
end
% -------------------------------------------------------------------------
%% -------------------------------------------------------------------------
%              ---Settlement Calculation----
% -------------------------------------------------------------------------
n_sr=101;   % number of degrees of saturation from 0.0 to 1.0
dsr=0.01;   % degree of saturation increment
% Seismically Induced Settlement of Unsaturated Soil is associated with two
% sources; calculated separately and added up
DH_com=zeros(1,n_sr);    % settlement due to compression of void space
DH_con=zeros(1,n_sr);    % settlement due to consolidation

%% Settlement due to Compression of Void Space

for nsr=1:n_sr

    for div=1:n_div
    % n_div : sublayers

    Sr(nsr,div)=dsr*(nsr-1);

    % wet density
    ro_init(nsr,div)=ro_init_d*(1+Sr(nsr,div)*e_init/Gs);
```

```
    % depth of the center of each sub-layer
    Depth_C(nsr,div)= (2*div-1)*H/(2*n_div);

    % total stress at the center of each layer
    Sigma_C(nsr,div)= ro_init(nsr,div)*g*Depth_C(nsr,div);

    % find suction value from swrc parameters based on van Genuchten model
    teta_r=0.00;
    teta_s=0.397;
    alpha_v=0.24; %1/kPa
    N_v=7;
    if Sr(nsr,div)>=(teta_r)/(teta_s)
        suction(nsr,div)=1000*(1/alpha_v)*(((Sr(nsr,div)-teta_r/teta_s)/(1-
teta_r/teta_s))^(N_v/(1-N_v))-1)^(1/N_v);
    else
        suction(nsr,div)=0;
    end

    % suction stress calculation (Lu et al. 2010)
    Sigma_suction_C(nsr,div)=
suction(nsr,div)/((1+(alpha_v*suction(nsr,div)/1000)^N_v)^((N_v-1)/N_v));

    % effective stress calculation (Lu et al. 2010)
    if Sr(nsr,div)==0.00

        % effective stress
        Sigmap_C(nsr,div)=Sigma_C(nsr,div);

    elseif Sr(nsr,div)==1.00

        % pore water pressure
        u_init_C(nsr,div)=ro_water*g*Depth_C(nsr,div);

        % effective stress
        Sigmap_C(nsr,div)=Sigma_C(nsr,div)-u_init_C(nsr,div);

    else

        % effective stress
        Sigmap_C(nsr,div)=Sigma_C(nsr,div)+ Sigma_suction_C(nsr,div);

    end

    % maximum shear modulus

    % Hardin and Richart (1963) for dry round-grained Ottawa Sand
     G_max_C(nsr,div)= 7000000*(((2.17-
e_init)^2)/(1+e_init))*(((1+2*K_0)/3)*Sigmap_C(nsr,div)/1000)^0.5;

    % maximum shear modulus , Ghayoomi an McCartney (2011) for F-75 Ottawa
    % Sand
    % G_max_C(nsr,div)=
```

```
9200000*(((1+2*K_0)/3)*Sigmap_C(nsr,div)/1000)^0.5;

    % stress reduction factor (Pradel, 1998)
    z_0 = 30.5; % m
    r_d_C(nsr,div) = 1/(1+(Depth_C(nsr,div)/z_0)^2);

    % average induced shear stress (Tokimatsu and Seed, 1987)
    Tau_ave_C(nsr,div)=(a_ave)*(Sigma_C(nsr,div))*r_d_C(nsr,div);

    % atmospheric pressure
    P_0 = 101.3 ; % kPa % Stewart

    % mean total stress
    P_C(nsr,div)= ((1+2*K_0)/3)*Sigma_C(nsr,div);

    % based on Darendeli and Stokoe (2001) and Stewart and Whang (2003) and
    % for PI=0
    % Initial estimate for the induced shear strain and shear modulus
    a_gamma(nsr,div)=0.199*(Sigmap_C(nsr,div)/(P_0*1000))^0.231;
    b_gamma(nsr,div)=10850*(Sigmap_C(nsr,div)/(P_0*1000))^-0.410;


gammaE_C(nsr,div)=((1+a_gamma(nsr,div)*exp(b_gamma(nsr,div)*Tau_ave_C(nsr,div
)/G_max_C(nsr,div)))/(1+a_gamma(nsr,div)))*(Tau_ave_C(nsr,div)/G_max_C(nsr,di
v));
    GE_C(nsr,div)=Tau_ave_C(nsr,div)/gammaE_C(nsr,div);

    % Menq 2003
    gamma_r_C(nsr,div)= 0.01*0.12*(Cu^-
0.6)*(Sigmap_C(nsr,div)/P_0/1000)^(0.5*(Cu^-0.15));
    % a_curve(nsr,div)= 0.86+0.1*log(Sigmap_C(nsr,div)/P_0/1000);

    % Hardin and Drnevich (1972)
     a_curve(nsr,div)=0.999;

    % Iteration process to find the compatible shear modulus and the
    % induced shear strain


G_C(nsr,div)=G_max_C(nsr,div)*(1/(1+(gammaE_C(nsr,div)/gamma_r_C(nsr,div))^a_
curve(nsr,div)));
    gamma_C(nsr,div)= Tau_ave_C(nsr,div)/G_C(nsr,div);
    gammap_C(nsr,div)=gammaE_C(nsr,div);
    while (abs(gamma_C(nsr,div)-gammap_C(nsr,div)))/gammap_C(nsr,div)>0.0001
        gammap_C(nsr,div)=gamma_C(nsr,div);

G_C(nsr,div)=G_max_C(nsr,div)*(1/(1+(gammap_C(nsr,div)/gamma_r_C(nsr,div))^a_
curve(nsr,div)));
        gamma_C(nsr,div)=Tau_ave_C(nsr,div)/G_C(nsr,div);
    end


    % modified SPT-N value (Tokimatsu and Seed 1987)
```

```
    N1_C(nsr,div)= floor((Dr_init/0.15)^2);

    % Volumetric strain under 15 cycles of shear strain (Pradel 1998,
Tokimatsu and Seed
    % 1987, and Silver and Seed 1971)
    Eps_15(nsr,div)=gamma_C(nsr,div)*(N1_C(nsr,div)/20)^(-1.2);

    % Volumetric Strain (Silver and Seed 1971, Pradel 1998)
    Eps_N(nsr,div)= Eps_15(nsr,div)*(n_cycle/15)^0.45;

    % modification of volumetric strain for degree of saturation
    Eps_mod(nsr,div)=Eps_N(nsr,div)*(1-Sr(nsr,div))^1;

    % differential layer settlement
    dDH_com(nsr,div)= Eps_mod(nsr,div)*H/n_div;

    % total collapse settlement
    DH_com(nsr)=DH_com(nsr)+dDH_com(nsr,div);

    end
end

%% Settlement due Consolidation associated with PPD
  for nsr=1:n_sr

    for div=1:n_div

    % Cyclic Stress Ratio Calculation
    CSR(nsr,div)=Tau_ave_C(nsr,div)/Sigmap_C(nsr,div);

    % NL vs CSR for Saturated Sand (Seed and Lee 1965)
    a_csr_N = -0.00732*e_init+0.00920;
    b_csr_N = 0.17007*e_init-0.19286;
    c_csr_N = -1.44463*e_init+1.55401;
    N_L(nsr,div) = exp((-b_csr_N - sqrt((b_csr_N^2-4*a_csr_N*(c_csr_N-
CSR(nsr,div)))/(2*a_csr_N))));

    % ru function (Krammer 1996)
    alpha = 0.7;
    if n_cycle<=N_L(div)
    r_u(nsr,div)= 1/2+(1/pi)*asin(2*(n_cycle./N_L(nsr,div))^(1/alpha)-1);
    else
    r_u(nsr,div)=1;
    end

    % ru for unsat based on Yoshimi 1989 ans some modification (not sure)
    r_u(nsr,div)=r_u(nsr,div)*(Sr(nsr,div))^3.5;

    % volumetric strain due to consolidation of liquefied sand for high CSR
    % and loose sand for Dr=45%

    % Tokimatsu and Seed (1987)
```

```
    % epspL(nsr,div)=0.12*(1/N1_C(nsr,div))^0.75;
    % Wu and Seed (2004)
     epspL(nsr,div)=0.2*(1/N1_C(nsr,div))^0.6;

    % Volumetric Strain ratio for certain amount of pore water pressure
    %(Lee and Albaisa 1974)
    Epsp(nsr,div)=epspL(nsr,div)*(r_u(nsr,div))^2.25;

    % differential layer settlement
    dDH_con(nsr,div)= Epsp(nsr,div)*H/n_div;

    % total consolidation settlement
    DH_con(nsr)=DH_con(nsr)+dDH_con(nsr,div);

    end
  end

DH=DH_com+DH_con;

%figure (1);
%mark=['+', 'o', '*', 'x', 's', 'd'];
%j=1;
%for k=[1, 21, 41, 61, 81, 101]
%plot(Sigmap_C(k,:)/1000,Depth_C(k,:),'LineWidth',2,'color','k', 'Marker',
mark(j))
%j=j+1;
%hold on
%end
%ylabel('Prototype depth (m)','FontSize',20)
%xlabel('Effective stress (kPa)','FontSize',20)
%set(gca,'FontSize',14)
%grid on

%figure (2);
%mark=['+', 'o', '*', 'x', 's', 'd'];
%j=1;
%for k=[1, 21, 41, 61, 81, 101]
%plot(G_max_C(k,:)/1000000,Depth_C(k,:),'LineWidth',2,'color','k', 'Marker',
mark(j))
%j=j+1;
%hold on
%end
%ylabel('Prototype depth (m)','FontSize',20)
%xlabel('G_{max} (kPa)','FontSize',20)
%set(gca,'FontSize',14)
%grid on

%figure (3);
%plot(Sr(:,1),gamma_C(:,1)*100,'marker','o','LineWidth',2,'color','k')
%hold on
%plot(Sr(:,1),gamma_r_C(:,1)*100,'marker','+','LineWidth',2,'color','k')
%xlabel('S_r','FontSize',20)
%ylabel('Shear Strain,\gamma (%)','FontSize',20)
```

```
%ylim([0,0.05]);
%legend('\gamma_{iterated}','\gamma_r','FontSize',18)
%set(gca,'FontSize',14)
%grid on

%figure (4);
%plot(Sr(:,1),Eps_mod(:,1)*100,'LineWidth',2,'color','k')
%xlabel('S_r','FontSize',18)
%ylabel('Volumetric strain due to compression (%)','FontSize',18)
%set(gca,'FontSize',14)
%grid on

%figure (5);
%plot(Sr(:,1),r_u(:,1),'LineWidth',2,'color','k')
%set(gca,'FontSize',14)
%xlabel('S_r','FontSize',20)
%ylabel('r_u','FontSize',20)
%set(gca,'FontSize',14)
%grid on

%figure (6);
%plot(Sr(:,1),Epsp(:,1)*100,'LineWidth',2,'color','k')
%xlabel('S_r','FontSize',18)
%ylabel('Volumetric strain due to consolidation (%)','FontSize',18)
%set(gca,'FontSize',14)
%grid on

figure (7);
%plot(Sr(:,1),DH_com*1000,'LineWidth',2.5,'color','b')
%hold on
%plot(Sr(:,1),DH_con*1000,'LineWidth',2.5,'color','r')
%hold on
plot(Sr(:,1),DH*1000,'LineWidth',2.5,'color','k')
xlabel('S_r','FontSize',20)
ylabel('Total settlement (mm)','FontSize',20)
set(gca,'FontSize',14)
grid on
```